

## REVIEW ARTICLE

## Superconducting quantum interference device instruments and applications

R. L. Fagaly

*Tristan Technologies, 6185 Cornerstone Court East, Suite 106, San Diego, California 92121*

(Received 7 November 2005; accepted 18 July 2006; published online 11 October 2006)

Superconducting quantum interference devices (SQUIDs) have been a key factor in the development and commercialization of ultrasensitive electric and magnetic measurement systems. In many cases, SQUID instrumentation offers the ability to make measurements where no other methodology is possible. We review the main aspects of designing, fabricating, and operating a number of SQUID measurement systems. While this article is not intended to be an exhaustive review on the principles of SQUID sensors and the underlying concepts behind the Josephson effect, a qualitative description of the operating principles of SQUID sensors and the properties of materials used to fabricate SQUID sensors is presented. The difference between low and high temperature SQUIDs and their suitability for specific applications is discussed. Although SQUID electronics have the capability to operate well above 1 MHz, most applications tend to be at lower frequencies. Specific examples of input circuits and detection coil configuration for different applications and environments, along with expected performance, are described. In particular, anticipated signal strength, magnetic field environment (applied field and external noise), and cryogenic requirements are discussed. Finally, a variety of applications with specific examples in the areas of electromagnetic, material property, nondestructive test and evaluation, and geophysical and biomedical measurements are reviewed. © 2006 American Institute of Physics.

[DOI: [10.1063/1.2354545](https://doi.org/10.1063/1.2354545)]

### I. INTRODUCTION

There are many ways to measure magnetic fields and properties. Sensing methods have been based on the use of induction coils, flux gate magnetometers, magnetoresistive and Hall effect magnetometers, magneto-optical magnetometers, and optically pumped magnetometers. Sensitivities range from microtesla to picotesla levels. Reference<sup>1</sup> gives an overview of the principles and design of magnetic sensors and magnetometers. The most sensitive magnetic flux detector is the superconducting quantum interference device (SQUID). This device, operating at cryogenic temperatures with quantum-limited sensitivity, has demonstrated field resolution at the  $10^{-17}$  T level.

#### A. Superconductivity

At temperatures approaching absolute zero, certain materials undergo a transition to what is known as the superconducting state. In 1911, Kamerlingh-Onnes<sup>2</sup> discovered that the resistance of mercury, when cooled below 4.2 K (K), dropped to an immeasurably small value [Fig. 1(a)].

This transition from normal resistance to resistanceless behavior takes place over a narrow temperature range—about 0.001 K for pure, strain-free metals and a degree or more for alloys and ceramics. Below this temperature, known as the transition temperature ( $T_c$ ), the material is characterized by a complete lack of electrical resistance. While it is not possible to demonstrate true zero dc resis-

tance, circulating current decay experiments superconducting rings of tin have been made to carry circulating dc currents for a period much greater than a year, disconnected from any power source, without any measurable decrease in current.<sup>3</sup> This demonstrates that the resistivity of superconducting tin is at least 17 orders of magnitude less than that of room temperature copper.

Subsequent investigations<sup>4</sup> indicated that a large number of materials undergo a similar superconducting transition. The source of resistivity in normal materials is the scattering of the electrons as they move through the materials. According to the Bardeen-Cooper-Schrieffer (BCS) theory,<sup>5</sup> phonon exchange between electrons causes the electrons to condense into weakly bound pairs (Cooper pairs) that can travel without scattering. The superconducting coherence length  $\xi$  is a measure of the distance over which the superconducting pair density can change and is of the order of the spatial size of a Cooper pair. Electrons in Cooper pairs can exchange partners, and they can be depaired by thermal (critical temperature  $T_c$ ), kinetic (critical current density  $J_c$ ), or magnetic (critical field  $H_c$ ) interactions. The temperature, current density, and magnetic field under which the particular material is superconducting define the superconducting phase space for the material.

In 1986, Bednorz and Müller<sup>6</sup> discovered a new class of ceramic oxides that became superconducting near 30 K—significantly warmer than any previously known superconductor. Since then, newer materials have been developed

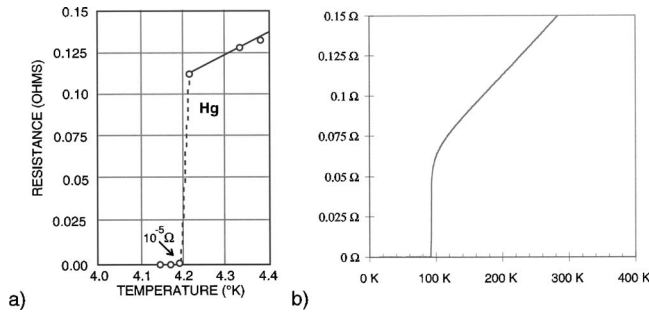


FIG. 1. Resistance of mercury (a) (after Ref. 2) and YBa<sub>2</sub>Cu<sub>3</sub>O<sub>7-δ</sub> vs (b) absolute temperature.

with the superconducting transition temperatures above 130 K, well above the boiling point of liquid nitrogen. YBa<sub>2</sub>Cu<sub>3</sub>O<sub>7-δ</sub> (often referred to as YBCO) [Fig. 1(b)] with  $T_c > 90$  K is the most commonly used superconducting ceramic oxide. To distinguish between the types of materials used in making SQUID sensors, we denote the older (primarily) metallic superconductors that typically operate at or near liquid helium temperatures (4.2 K) as low temperature superconductors (LTSs) and the newer (primarily ceramic oxide) materials that can operate at liquid nitrogen temperatures (77 K) as high temperature superconductors (HTSs).

## B. Meissner effect

A unique property of the superconducting state is observed if a superconductor is put in a magnetic field and then cooled below its transition temperature.<sup>8</sup> In the normal state, magnetic flux lines can penetrate through the material [Fig. 2(a)]. For a hypothetical, perfectly conducting (zero resistance) material, the currents induced by attempts to change the magnetic field would prevent changes in the magnetic field within the conductor. In contrast, in the superconducting state flux lines cannot exist within the superconducting region except for a shallow surface layer, called the penetration depth  $\lambda$ . As the material becomes superconducting, the magnetic flux is expelled [Fig. 2(b)] unlike a perfect conductor that would trap the flux. This flux expulsion is called the Meissner effect and is a consequence of the fundamental character of the superconducting state—it is new physics.

If the superconducting material forms a ring, the flux interior to the ring is trapped when the ring becomes superconducting [Fig. 2(b)] rather than expelled as in a continuous solid. If the magnetic field is then turned off, a current, which circulates around the ring keeping the magnetic flux ( $\Phi = \int B dA$ ) inside the ring constant, is induced [Fig. 2(c)]. Because of the electrical resistance, the current in a ring made of a normal (nonsuperconducting) metal will quickly decay. The current decay is exponential with a time constant that is related to the resistance ( $R$ ) and inductance ( $L$ ) of the ring,  $I(t) = I_0 e^{-tR/L}$ . In a superconducting ring ( $R=0$ ), there would be no decay of the current and a persistent current ( $I = -\Phi/L$ ) is established. The current continues to circulate as long as the ring is kept below  $T_c$ , as previously discussed.

Total flux exclusion is seen in type-I superconductors in the superconducting state, e.g., below the critical field  $H_{c1}$ . There is a second category of superconductors, type-II, that

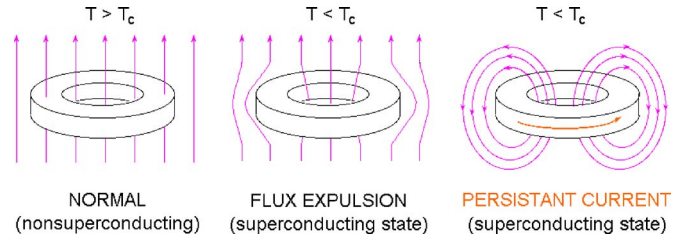


FIG. 2. (Color online) Meissner effect in a superconducting ring cooled in an externally applied magnetic field.

demonstrate complete flux exclusion below a lower critical field  $H_{c1}$ , but display partial flux exclusion between  $H_{c1}$  and an upper critical field  $H_{c2}$ . In this range, the material separates into normal and superconducting regions—the flux is confined to the normal regions.

## C. Critical current and ac resistance

As noted above, there is a limiting current density that a superconductor can support and still remain in the superconducting state. This density is theoretically related to the product of the density of electrons and their velocity. If the energy of the Cooper pairs exceeds their binding energy, they will decouple and the material will exhibit normal rather than superconducting properties. In practice, the critical current density is highly dependent on sample preparation.<sup>7</sup>  $J_c$ 's can be in the order of  $10^7$ – $10^8$  A/cm<sup>2</sup> for type-I materials (Sec. II A) and of  $10^6$ – $10^7$  A/cm<sup>2</sup> for type-II materials.

In the high frequency limit, there can be losses even if the material exhibits zero resistance at dc. This is because type-II materials (and type-I materials within the skin depth) allow flux penetration. Defects trap the flux as vortices at pinning sites; the strength of the trapping is measured in terms of the pinning energy—the energy required to dissociate a flux vortex from a pinning site. Dissipative flux motion (due to an alternating current moving the vortices about the pinning sites) absorbs energy. This dissipation gives rise to an effective resistance that increases with frequency up to the frequency whose energy corresponds to the superconducting energy gap [ $\Delta(T)$ , the energy needed to decouple the paired electrons].

## D. Flux quantization

As long as a superconducting ring remains in the superconducting state, the magnetic flux within it remains trapped. This trapped flux has some very unusual properties. First, one cannot change the level of magnetic flux in the ring in a continuous manner. One can only trap discrete levels of the magnetic flux (Fig. 3). In other words, the magnetic flux is quantized<sup>9</sup> and exists only in multiples of the flux quantum ( $\Phi_0 = 2.068 \times 10^{-15}$  Wb;  $1 \text{ Wb/m}^2 = 1 \text{ T}$ ). Equivalently, for a ring with an area of  $1 \text{ cm}^2$ , the field inside the ring can only exist in discrete steps of  $2.068 \times 10^{-11} \text{ T}$ .

## E. The Josephson effect

For a loop of superconducting wire interrupted by a normal (i.e., resistive) region, one would expect that the wave function of the Cooper pair would quickly decay across the

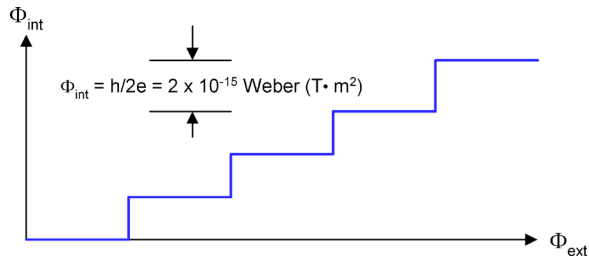


FIG. 3. (Color online) Flux quantization.

resistive barrier [Fig. 4(a)] and the corresponding superconducting current would cease. In 1962, Josephson<sup>10</sup> predicted the possibility of electrons tunneling from one superconducting region to another. They are separated by a resistive (insulating) barrier, often referred to as a “weak link” [Fig. 4(b)]. For distances less than the coherence length ( $\xi$ ) of the superconducting material (Table I) and currents less than a critical current  $I_c$  that is characteristic of the weak link, the Cooper pairs can tunnel through the resistive barrier and the superconducting current can penetrate the resistive barrier with no voltage drop [Fig. 4(c)].

There are many ways to make a weak link. The junction can be an insulating [superconducting-insulator-superconducting (SIS)] barrier such as a point contact where the barrier is  $\text{NbO}_x$  [Fig. 5(a)], a normal metal [superconducting-normal-superconducting (SNS)] or a microbridge where the current flowing through a small constriction exceeds  $J_c$  only in the region of the microbridge [Fig. 5(b)]. Present day LTS devices use tunnel junction weak links [Fig. 5(c)]. HTS devices use either intrinsic—bicrystal [Fig. 5(d)] or step edge grain boundary [Fig. 5(e)]—junctions or extrinsic—step edge SNS [Fig. 5(f)] or ramp edge [Fig. 5(g)]—structures.

Bicrystal [Fig. 5(d)] and ramp edge [Fig. 5(g)] junctions have become popular in commercial HTS devices. This is because ramp edge junctions have a larger coherence length along the  $a$ - $b$  plane, have good control of  $I_c$  by relatively thick barrier (which gives good reproducibility and stability), can be arbitrary placed on the substrate and used for complex

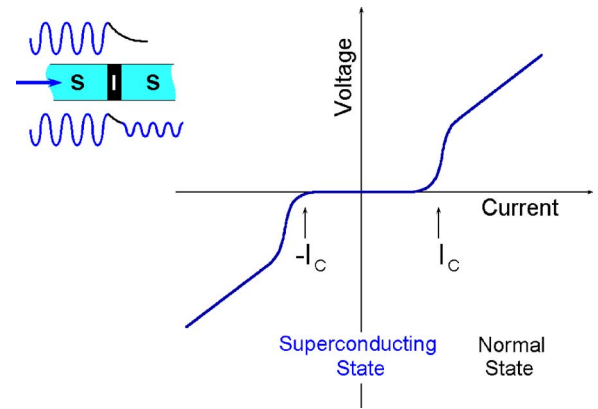


FIG. 4. (Color online) (a) Quantum mechanical wave function of a superconducting current penetrating a normal region, showing the attenuation of the wave function as it penetrates an insulating layer. (b) Quantum mechanical wave function penetrating a thin normal region separating two superconducting regions. (c) Current vs voltage curve of a shunted Josephson tunnel junction measured across the junction. In an ideal Josephson junction, the transition from resistive to superconducting behavior would be a sharp vertical transition, rather than the real-world curved transition shown.

circuits, and can operate in higher fields<sup>11</sup> because they are shielded by a top superconducting electrode. Bicrystal junctions are high Ohmic devices (good for SQUIDs and microwave detectors), have good control of  $I_c$  by misorientation angle (good reproducibility and stability), like ramp edge junctions have a larger coherence length along the  $a$ - $b$  plans, and, most importantly, are relatively simple to fabricate—only one HTS layer and one lithography stage is needed. Because of the higher quality and reproducibility combined with a relatively easy technology, these junction types have become the most studied and better developed devices.

The next most popular HTS junction types are the step edge [Fig. 5(e)] junctions (cheaper than bicrystal ones, but the quality and reproducibility is usually poorer) and step edge junctions with a normal metal shunt (better reproducibility for the shunt resistance ( $R_n$ ), but  $R_n$  and  $I_c R_n$  are usually too low for SQUID operation).

TABLE I. Properties of superconducting materials (parts of this table were taken from Refs. 7 and 15).

Material	$T_c$ (K)	$H_{c0}$ (T)	$H_{c1}$ (T)	$H_{c2}$ (T)	$\xi_0$ (nm)	$\lambda_0$ (nm)	$\Delta_0$ (meV)
LTS							
Lead	7.193	0.0803	...	...	90		1.35
Mercury	4.153	0.0412					
Niobium	9.25	...	0.198	0.268	40		1.50
NbTi	9.50	...		15	4	240	1.5
Nb <sub>3</sub> Sn	18.1	...		24.5	3	65	3.4
HTS							
			$H_{c1}$ (T)	$H_{c2}$ (T)	$\xi_{ab}$ (nm)	$\xi_c$ (nm)	$\lambda_{ab}$ (nm)
Ba <sub>0.6</sub> K <sub>0.4</sub> BiO <sub>3</sub>	30						
La <sub>1.85</sub> Sr <sub>0.5</sub> CuO <sub>4</sub>	40			4	0.7		
MgB <sub>2</sub>	39		18	6.5	2.5	140	
YBa <sub>2</sub> Cu <sub>3</sub> O <sub>7-<math>\delta</math></sub>	95		>100	4	0.7	150	
Bi <sub>2</sub> Sr <sub>2</sub> Ca <sub>2</sub> Cu <sub>3</sub> O <sub>10</sub>	110		>100	4.5	0.2	150	
Tl <sub>2</sub> Bi <sub>2</sub> Ca <sub>2</sub> Cu <sub>3</sub> O <sub>10</sub>	125						
HgBa <sub>2</sub> Ca <sub>2</sub> Cu <sub>3</sub> O <sub>8+<math>\delta</math></sub>	134						

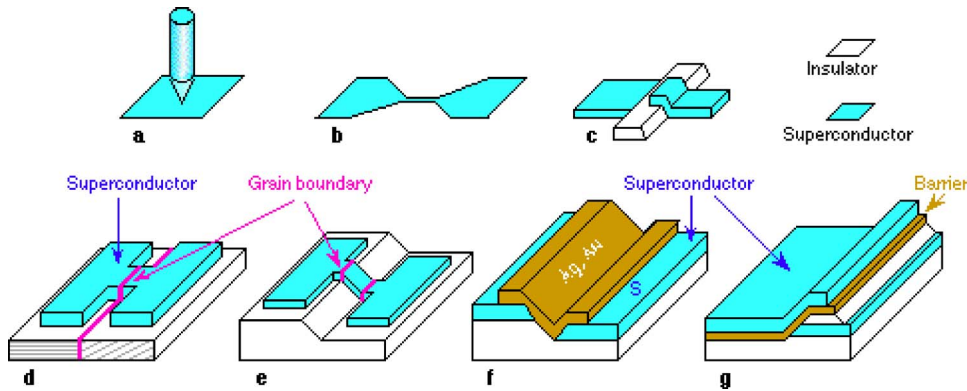


FIG. 5. (Color online) Different types of Josephson junctions: (a) point contact, (b) microbridge, also known as a Dayem bridge, (c) thin-film tunnel junction (the barrier can either be an insulating (SIS) or normal metal (SNS) material), (d) bicrystal, (e) step edge grain boundary, (f) step edge superconductor-normal-superconductor, and (g) ramp edge superconductor-normal-superconductor with a  $\text{PrBa}_2\text{Cu}_3\text{O}_{7-\delta}$  barrier. After Ref. 18.

## F. Superconducting quantum interference devices

SQUID uses Josephson effect phenomena to measure extremely small variations in magnetic flux. Typically, a SQUID is a ring of superconductor interrupted by one or more Josephson junctions (Fig. 6).

A bias current ( $I_b$ ) is applied (two  $I_b$  in the case of a dc SQUID) putting the operational point on the  $I$ - $V$  curve [Fig. 7(a)] midway between superconducting and resistive behaviors. Shunt resistors are used to prevent hysteretic behavior in the  $I$ - $V$  curve.<sup>12</sup> Inductively coupling magnetic flux into the SQUID loop creates screening currents ( $I_{\text{loop}} = \Phi_{\text{loop}}/L_{\text{loop}}$ ) that will effectively increase or decrease  $I_c$ , depending on the direction of the induced flux.

Fixing  $I_b$  at a slightly higher value than  $I_c$ , when an external magnetic flux ( $\Phi_{\text{ext}} = B_{\text{ext}}A$ ) is coupled into the Josephson loop, the voltage drop across the Josephson junction will change. As the external flux increases (or decreases), the voltage will change in a periodic manner with the period being that of the flux quantum  $\Phi_0$  [Fig. 7(b)]. Monitoring the change in voltage allows determination of the magnetic flux that has been coupled into the SQUID loop. By using external feedback (Sec. III A 1), it is possible to “lock” the SQUID at a unique point on the  $V$ - $\Phi_0$  curve; the feedback current [coupled into the SQUID loop (Fig. 6)] is then a measure of the externally applied flux. SQUIDs are normally operated at the steepest part of the  $V$ - $\Phi_0$  curve (where  $\partial V/\partial\Phi$  is a maximum).

There is also the need for the feedback electronics to be able to track large changes in applied fields. For signal changes larger than  $\Phi_0/4$ , the electronics need to be able to apply negative feedback fast enough to keep the voltage at the operating or lock point. If the electronics cannot change the feedback current (slew) fast enough, it is possible that they could end up at a different point on the  $V$ - $\Phi_0$  curve (same  $V$ , different  $\Phi_0$ ). If flux jumping occurs, it may be necessary to go to faster electronics or limit the dynamic

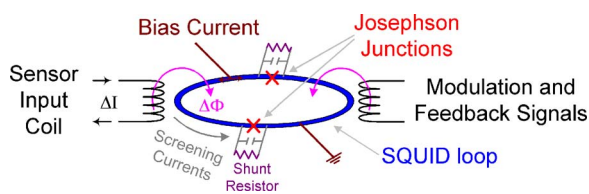


FIG. 6. (Color online) Dual junction (dc) SQUID loop. The capacitor represents the self-capacitance of the junction.

range (or bandwidth) of the input signal (source).

The theory of different types of SQUIDs is described in detail in the literature.<sup>13–16</sup> SQUIDs are operated as either rf or dc SQUIDs. The prefix rf or dc refers to whether the Josephson junction is biased with an alternating current (rf) or a dc current. Due to their lower noise (Sec. III C), nearly all commercial SQUIDs are dc SQUIDs. As seen in Fig. 6, flux is normally (inductively) coupled into the SQUID loop via an input coil which connects the SQUID to the experiment. Because the input coil is superconducting ( $R=0$ ), its impedance is purely inductive. HTS SQUIDs have the input coil either as part of the Josephson loop or as inductively coupled (via a flip chip) to the Josephson loop.

## II. SQUID SENSORS

There are fundamental differences between low and high temperature superconductors. LTS materials are metallic (although some nonmetallic and organic compounds have been found to be superconducting at liquid helium temperatures, none have been fabricated into SQUIDs), isotropic, and have coherence lengths ( $\xi$ ) that are tens to hundreds of interatomic distances. HTS materials are ceramics, brittle, anisotropic, and (with the exception of  $\text{MgB}_2$ ) essentially planar and have coherence lengths in the  $c$  direction (perpendicular to the  $a$ - $b$  plane) that are significantly smaller (Table I). Not only is there a temperature limitation to superconductivity; there is also a field limitation. The material remains in the superconducting state below a critical field  $H_c(T) = H_{c0}[1 - (T/T_c)^2]$ , where  $H_{c0}$  is the critical field at  $T=0$ . Type-II superconductors have two critical fields:  $H_{c1}$ , below which the material acts as a type-I superconductor, and  $H_{c2}$ , the upper limit in the type-II (mixed) state.

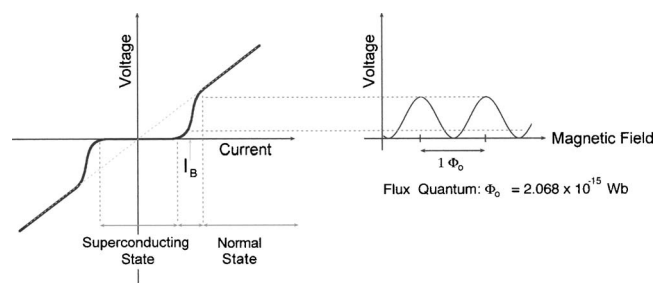


FIG. 7. (a) bias point ( $I_b$ ) for Josephson junction; (b) voltage vs externally applied flux at constant bias current.

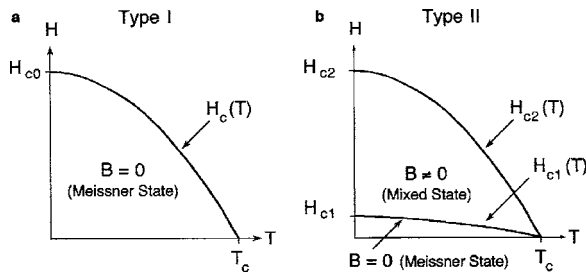


FIG. 8. The  $H$ - $T$  phase space for (a) type-I and (b) type-II superconductors.

## A. Materials

The superconducting phase space is defined by the critical temperature, the critical magnetic field (both of which are intrinsic properties of the superconducting state), and the critical current density (which is extrinsic and the value used is that from the strongest pinning situation).

We have already briefly discussed type-I and type-II superconductors. Materials (typically pure metallic elements such as Hg or Pb) that totally exclude flux in the superconducting state (up to a well-defined transition temperature  $T_c$ ) are referred to as type-I superconductors [Fig. 8(a)]. Materials that exhibit the partial Meissner effect described earlier are referred to as type-II superconductors [Fig. 8(b)]. Below a lower critical field  $H_{c1}$ , they act as type-I superconductors. Above  $H_{c1}$ , the flux can penetrate into type-II superconductors and the material is (incompletely) threaded by flux lines; the material can be considered to be in a vortex state.<sup>14</sup> The higher the applied field, the greater number of allowed flux lines until the upper critical field  $H_{c2}$  is reached, where the entire material transitions to the normal state. Type-II superconductors (e.g., NbTi and Nb<sub>3</sub>Sn) tend to be alloys or transition metals with high electrical resistivity in the normal state. All HTS materials are type-II superconductors. High field superconducting magnets are fabricated from type II materials.

LTS devices have significant advantages and one disadvantage—operating temperature—over HTS devices. Because LTS materials are isotropic and have long coherence lengths (Table I) relative to their interatomic distances, it is possible to fabricate devices with three-dimensional structures. This allows crossovers and multilayer structures that permit higher sensitivity, i.e., the ability to make multiturn than single turn devices. HTS crossovers (needed for multiturn coils) require larger dimensions than the coherence length of YBCO in the  $c$  direction. The effect is that a HTS crossover acts as a Josephson or insulating junction with the addition of significant  $1/f$  noise (Sec. III E). The associated flux creep that can occur (particularly in HTS materials) by operating in the mixed (vortex) state can lead to nonlinearity or hysteretic effects. While their pinning energies are somewhat lower than YBCO, bismuth and thallium compounds seem to have much lower densities of pinning sites.<sup>17</sup> As a result, the flux creep (and its associated resistivity) is considerably higher. Because of this, most HTS SQUIDs are fabricated from YBCO because of its sufficiently strong (and intrinsic) flux pinning at 77 K. By operating at lower temperatures (20–30 K), it is possible to freeze out the hys-

teretic effects seen in bismuth and thallium devices at 77 K, but because of the convenience of liquid nitrogen as a cryogen, all commercial HTS SQUIDs are fabricated using YBCO as the superconductor. Even when operated as just a bare SQUID loop with no input coils [as might be used in a magnetic microscope (Sec. IX C)], LTS devices are significantly quieter than HTS devices—in both white noise and  $1/f$  noise.

A significant difference between LTS and HTS materials is that LTS materials (e.g., NbTi) are ductile and—in wire form—can be made into complex three-dimensional structures such as axial gradiometers (Sec. IV E). Additionally, using NbTi (or Nb<sub>3</sub>Sn) allows detection coils to be in high field regions, while the actual LTS SQUID sensor can be placed in a low field environment. Because of the inability to make a truly superconducting flexible three-dimensional structure, axial HTS gradiometers are not possible (although thin film planar gradiometers are). Even if it was possible to make a separate HTS coils, the inability to make superconducting joints (or joints with contact resistances at the sub-pico-ohm level) prevents true dc response in discrete element HTS circuits<sup>17</sup> (i.e., the in-series resistance acts as a low frequency high pass filter).

Another advantage of LTS materials is that they are stable in air, whereas moisture degrades the HTS structure. Thus, passivation layers or overcoatings are required and add to the complexity of manufacture. Although LTS materials have superior properties, the ability to operate a device at liquid nitrogen rather than liquid helium temperatures gives HTS devices significant operational advantages and cannot be discounted.

The barrier used for fabricating the weak link is critical. Early point contact LTS devices used an NbO layer formed by oxidizing the end of a niobium needle that was then pressed against a block of niobium [Fig. 5(a)]. The first commercial dc SQUID used an amorphous SiO<sub>2</sub> barrier that allowed junctions with critical currents within a few percent to be easily fabricated. An unfortunate side effect was that the amorphous barrier had significant temperature dependent resistivity that caused frequency dependent noise (Sec. III C 5). Present day LTS SQUIDs utilize AlO<sub>x</sub> barriers with temperature independent critical currents. Reference 18 gives an excellent overview on HTS SQUIDs.

## B. Flux transformers

One problem with using just the SQUID loop as the detection coil is its small area and associated inductance ( $\sim 10^{-10}$  H). Increasing the area of the loop or connecting a larger loop in series would increase sensitivity, but the impedance mismatch [Eq. (11)] due to the increased inductance of the larger loop would negate much of the sensitivity gain. Most LTS SQUID sensors use a multilayer flux transformer to couple an externally detected flux into the SQUID loop (Fig. 9). The flux transformer can either be fabricated on a separate substrate and placed directly over the SQUID loop (commonly known as a flip chip), or it can be fabricated on the same substrate as the SQUID loop.<sup>19</sup> The input impedance of the flux transformer is much higher than that of the SQUID loop and typically ranges from 0.1 to 2  $\mu$ H. The

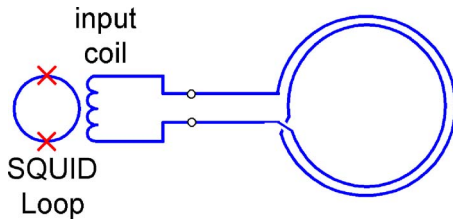


FIG. 9. (Color online) Flux transformer for coupling external flux (two turn “detection coils”). Not to scale.

larger impedance of the input coil allows detection coils to be significantly larger than the SQUID loop. Section IV discusses design of detection coils. Additionally, the use of a flux transformer allows placement of the SQUID sensor in a noise reduced environment (Sec. IV A), while the external field sensing portion could be placed in field or temperature regimes well beyond the operational limits of the SQUID sensor itself.

### C. Fractional turn SQUIDs

Another way to increase sensitivity of a bare SQUID loop is to connect not just a single detection coil, but a number of coils, not in series (as is done in traditional multiturn coils), but in parallel [Fig. 10(a)]. The critical concept is keeping the inductance of the SQUID loop itself very small, while having a large area for coupling to an external coil. This is because thermal noise puts an upper bound on the inductance of the loop itself. Referred to as a fractional turn (multiloop) SQUID,<sup>20</sup> this improves on sensitivity by reducing the input inductance by roughly  $L_{\text{poly}}/N^2 + L_{\text{spoke}}/N + L_{\text{jp}}$ , where  $L_{\text{poly}}$  is the total inductance of a polygonal pickup coil without spokes,  $L_{\text{spoke}}$  is the inductance of the spoke,  $L_{\text{jp}}$  is the small parasitic inductance of the Josephson junction connection lines, and  $N$  is the number of turns in the SQUID loop.<sup>21</sup>

By directly coupling a fractional turn input coil, this allows a small diameter input coil that can match the input impedance of the SQUID loop to be fabricated. Devices with  $N=3$  [Fig. 10(b)] to  $N=16$  have been fabricated with significantly reduced field noise. While fractional turn SQUIDs have better sensitivity, it should be noted that their spatial resolution (for nearby objects) may be significantly poorer. Depending on the geometry of the fractional turn SQUID, the spatial resolution can be as poor as half the device diameter, while conventional coils have demonstrated spatial resolutions up to 1/20th diameter (Sec. IV D). Because of this, fractional turn SQUIDs may not be the best choice for use in magnetic microscopy (Sec. IX B).

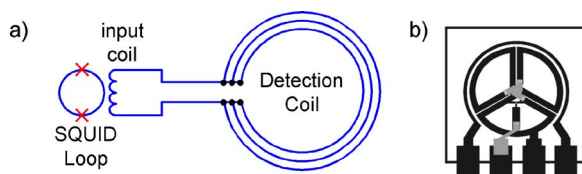


FIG. 10. (Color online) (a) Schematic of fractional turn SQUID sensor; (b) fabricated device. The pads are for coupling in the bias and feedback currents.

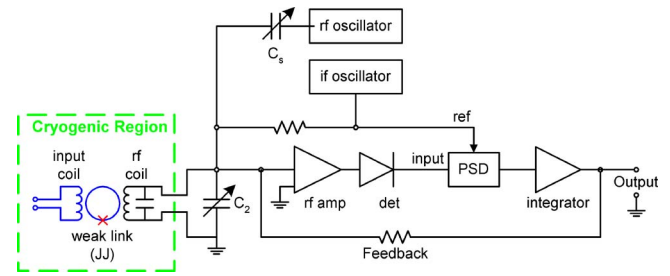


FIG. 11. (Color online) Block diagram of SQUID input and electronics for locked-loop operation of a rf SQUID. The input circuitry from the experiment (e.g., a detection coil which would be connected to the input coil) is omitted for clarity. PSD refers to phase sensitive detection, JJ means Josephson junction, and ref means reference.

## III. SQUID OPERATION AND PERFORMANCE

The major difference between rf and dc SQUIDs is that the dc SQUID may offer lower noise when compared to a rf SQUID. The cost of this increase in sensitivity can be the complexity of the electronics needed to operate a dc SQUID and the difficulty in fabricating two nearly identical Josephson junctions in a single device. From a historical viewpoint, although the LTS dc SQUID was the first type of SQUID magnetometer made, early LTS development was with rf SQUIDs. With modern thin film fabrication techniques and improvements in control electronics design, the dc SQUID offers clear advantages over the rf SQUID for many applications.

The system output voltage is the voltage drop across the feedback resistor in a negative feedback loop controlled by the SQUID electronics. The feedback signal is generated in response to changes in the output signal of the SQUID sensor. The output of the SQUID sensor is periodic in the field coupled into the SQUID loop. Negative feedback (similar to a phase-locked loop technique) is used to maintain the system operating point at a particular (and arbitrary) flux quantum. When operated in this mode, the system is in a flux-locked loop (Sec. III A 1).

### A. The rf SQUID

The rf SQUID (Ref. 22) utilizes a single Josephson junction and flux is normally (inductively) coupled into the SQUID loop via an input coil which connects the SQUID to the experiment and a “rf” coil that is part of a high- $Q$  resonant (tank) circuit to read out the current changes in the SQUID loop (Fig. 11).

This tuned circuit (in this example operated at 19 MHz) is driven by a constant current radio-frequency oscillator that is weakly coupled to the SQUID loop. As the oscillator drive amplitude is increased, the (peak) detected output of the rf amplifier increases until a critical level is reached. That is, an increase in drive amplitude produces a very small increase in output. The rf drive is set so that the SQUID operates on this plateau, where the detected output depends on the current flowing in the input coil. Any changes in the input coil current will induce a change in the current flowing in the SQUID ring. This shielding current causes the total flux linking the SQUID ring to remain constant as long as the ring remains superconducting. Another contribution to the total

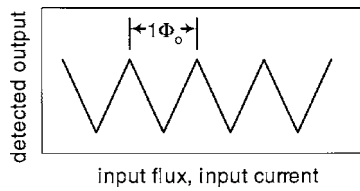


FIG. 12. Triangle pattern showing detected output (rf) voltage vs flux coupled into the SQUID.

flux in the SQUID (and to the shielding current) comes from the rf current in the (19 MHz) tuned circuit. Thus we can consider the shielding current to consist of an ac component and a dc component which biases the junction. When the amplitude of the ac component increases, the critical current of the weak link is reached and a transition occurs changing the flux state of the SQUID by a single flux quantum. This transition temporarily reduces the level of oscillation in the rf coil, which then builds up again to its maximum value, and the process repeats itself. Just after the transition, the weak link again becomes a superconductor and the shielding bias current due to the current in the input coil reestablishes itself to quantize the flux in the SQUID. When the rf oscillations have been reduced sufficiently, the Josephson junction will again be superconducting and the amplitude of the rf oscillations will begin to increase again. This behavior in the high- $Q$  tank leads to the very characteristic triangles shown in Fig. 12 (quite unlike the transfer functions seen with the dc SQUID).

If the dc current in the input coil is changed, the dc bias of the shielding current in the SQUID is changed so that the rf-induced transition occurs at a different level of oscillation in the rf coil. The detected rf output is a periodic function of the applied flux (Fig. 12). While it might be possible to measure the change in input coil current by simply counting the number of periods produced in the detected rf output, it may not be easy to tell if the external field is increasing or decreasing. In any case, the field resolution would be limited to  $1\Phi_0$ .

### 1. The flux-locked loop

A more commonly used mode of operation is a feedback scheme (Fig. 11) which locks in on either a peak or a valley in the triangle pattern output from the rf peak detector (Fig. 12). A feedback flux is applied to the SQUID through the rf coil that just cancels the change in flux from the input coil. This allows flux resolution to  $\mu\Phi_0$  levels.

An audio frequency oscillator (if oscillator in Fig. 11) provides a reference for a phase-sensitive detector and also modulates the flux linking the SQUID due to the rf coil by an amount of  $\Phi_0/2$  (peak to peak). This low frequency flux modulation, where  $f_{\text{modulation}}$  is typically several tens of kilohertz, modulates the detected rf output. The amplitude of the rf modulation is zero when the total flux in the SQUID corresponds to a peak or a valley [Fig. 7(b) or 12] and increases linearly to a maximum as the flux departs from an extremum one-fourth of the period ( $\Phi_0/4$ ). A change in flux in the SQUID results in an output from the phase-sensitive detector, which is fed back through a resistor to the rf coil. The

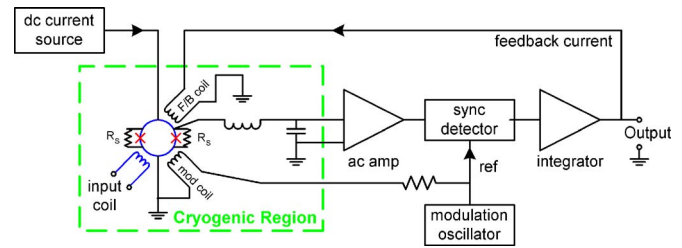


FIG. 13. (Color online) Block diagram of a typical dc SQUID. The detection coil (connected to the input coil) is omitted for clarity.

feedback current through the rf coil counters the flux change from the input coil and maintains the flux in the SQUID locked at a value corresponding to an extremum in the rf response. This manner of operation is called a flux-locked loop. The bandwidth in locked loop operation is necessarily  $< f_{\text{modulation}}/2$ .

For small scale signals, open loop operation—where the maximum amplitude of the input signal is  $< \Phi_0/2$ —can allow higher bandwidths. For example, a typical locked loop bandwidth for the rf SQUID electronics described above may be 20 kHz, but open loop operation can allow bandwidths an order of magnitude higher.

It should be noted that the rf and input coils (Fig. 11) are not wound around the SQUID loop, but inductively coupled to the SQUID loop. A minor advantage of the rf SQUID is that connections from the SQUID sensor to the room temperature electronics are simple—only a single coax or a single twisted pair of leads are needed.

## B. The dc SQUID

The dc SQUID differs from the rf SQUID in the manner of biasing the Josephson junction and the number of junctions. Since there are two junctions, they need to be matched within a few percent, as do the shunt resistors. It may be possible to operate SQUIDs with mismatched junctions, but performance (if any) would be significantly degraded. The ideal shunt resistor should have a temperature independent resistivity. The use of normal metal resistors such as Pd is preferred over amorphous materials or materials with superconducting transitions which would prevent operation of LTS devices below  $T_c$  (e.g., 0.915 K in the case of a molybdenum shunt resistor).

Figure 13 shows a schematic of a typical dc SQUID. Like the rf SQUID (Fig. 11), the input, feedback, and modulation coils are not wound around the SQUID loop, but inductively coupled to it. It is biased with a dc current approximately equal to twice  $I_c$  and develops a dc voltage across the junctions (and shunt resistors). A change in the magnetic flux applied through the SQUID loop induces a wave function phase change that enhances the current through one Josephson junction ( $I_{\text{total}} = I_b + I_{\text{screen}} > I_c$ ) and reduces the current through the other ( $I_{\text{total}} = I_b - I_{\text{screen}} < I_c$ ). As the external flux ( $\Phi_{\text{ext}}$ ) increases (or decreases), the voltage will change in a periodic manner with the period being that of the flux quantum  $\Phi_0$  [Fig. 7(b)]. The voltage, which is periodic in  $\Phi_0$ , is used to provide a feedback current that nulls the flux penetrating the SQUID loop. Like the rf SQUID, this feedback

current (presented as a voltage at the output) is a direct measure of changes in flux applied to the SQUID. Unlike the rf SQUID (Fig. 12), the  $V$ - $\Phi$  curve is sinusoidal in nature. Similar to rf SQUIDs (Sec. III A 1), open loop operation allows significantly greater bandwidths for small amplitude signals. Additional details on the operation of dc SQUIDs may be found in Ref. 23. The dc SQUID typically requires at least four pairs of leads (bias, modulation, signal, and feedback) between the SQUID and its electronics. A heater circuit (to momentarily drive the temperature of the SQUID above  $T_c$ ) is useful to remove trapped flux.

### 1. Alternate modulation schemes

The flux-to-voltage gain of the SQUID can be increased by shunting the device with a resistor in series with an inductor coupled mutually to the SQUID loop.<sup>24</sup> This additional positive feedback (APF) enhances the output voltage gain of the SQUID and enables the use of a direct readout, circumventing the conventional modulation scheme and increasing the bandwidth more than one order of magnitude to above 3 MHz.<sup>25</sup> Reference 26 discusses APF and other concepts such as two stage SQUIDs, SQUID series arrays, relaxation oscillation SQUIDs, and digital SQUIDs that have been used for SQUID readouts.

### C. Noise and sensitivity

SQUID noise is often presented as the spectral density of the equivalent flux noise  $S_\Phi(f)$  as a function of frequency or noise energy per unit bandwidth  $E_N(f) = S_\Phi(f)/2L$ , where  $L$  is the inductance of the input coil. To allow devices with differing input inductances to be directly compared, the sensitivity of SQUID devices is best discussed in terms of the energy sensitivity:

$$E_N = L_{\text{input}} I_N^2 = \frac{\Phi_N^2}{L_{\text{input}}}, \quad (1)$$

where  $L_{\text{input}}$  is the input inductance of the device,  $I_N$  is the current noise, and  $\Phi_N$  is the flux sensitivity.  $E_N$  is often expressed in terms of Planck's constant  $h = 6.6 \times 10^{-34}$  J/Hz.

Noise characterization may also be presented as the spectral density of the equivalent flux noise  $S_\Phi(f)$  as a function of frequency or noise energy per unit bandwidth  $E_N(f) = S_\Phi(f)/2L_{\text{input}}$ . Figure 14 shows typical energy sensitivities for LTS and HTS SQUIDs. As can be seen, the noise can be described as the sum of frequency independent (white) and frequency dependent ( $1/f$ ) terms.

Magnetometers are often discussed in terms of field sensitivity. However, because the field sensitivity is as much dependent on the geometry of the detection coil geometry (area, number of turns, etc.) as the SQUID itself, energy sensitivity allows comparison of devices independent of coil geometry. Calculation of magnetic field sensitivity is discussed in Sec. IV D. The effective area of the device must also be considered, especially in the case of bare and fractional turn SQUID loops.

#### 1. White noise

*a. rf SQUIDs.* The rf SQUID can be modeled<sup>27</sup> as an ideal (lossless) parametric up-converter where  $E_N$

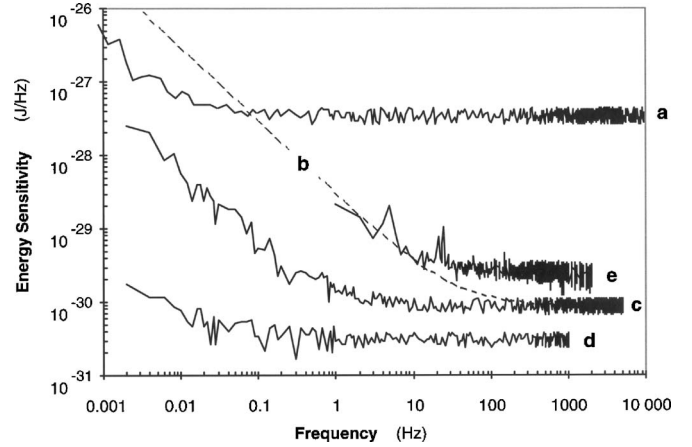


FIG. 14. Energy sensitivity vs frequency for a number of different SQUID devices: (a) is a LTS rf SQUID operated at a bias frequency of 19 MHz; (b) is a dc biased LTS dc SQUID with amorphous silicon barriers; (c) is (b) using ac biasing; (d) is a dc biased LTS dc SQUID with  $\text{AlO}_x$  barriers; and (e) is an ac biased HTS dc SQUID utilizing a ramp edge junction [Fig. 5(g)]. Devices (a)–(d) were operated at 4.2 K; device (e) was at 77 K.

$\propto k_B T_N / hf_B$ , where  $T_N$  is the noise temperature of the rf amplifier (Fig. 11) and  $f_B$  is the bias frequency used to excite the tank circuit. This results in the current (or field) noise in rf SQUIDs is proportional to  $1/\sqrt{f_B}$ . For a LTS rf SQUID operating at 19 MHz,<sup>28</sup> typical white noise is  $10^{-28}$  J/Hz [Fig. 14(a)]. Increasing the bias frequency to 180 MHz (Ref. 29) has been shown to reduce the white noise by a factor of 3. As  $f_B$  increases, the complexity of the electronics also tends to increase. With the discovery of high temperature superconductivity, the first HTS SQUIDs were single junction rf SQUIDs. As it is not known (at least theoretically) if there is a fundamental limit to the white noise of rf SQUIDs, at 1 GHz, a rf HTS SQUID could be quieter than a dc HTS SQUID.

*b. dc SQUIDs.* The minimum noise energy ( $E_N$ ) for a dc SQUID is given by:<sup>12</sup>

$$E_N \approx 4k_B T \sqrt{\pi L_{\text{loop}} C}, \quad (2)$$

where  $k_B$  is Boltzmann's constant,  $T$  is the temperature of the SQUID,  $L_{\text{loop}}$  is the inductance of the SQUID loop, and  $C$  is the self-capacitance of the junction. Substituting appropriate numbers indicates that  $E_N$  for a dc SQUID is on the order of  $h/2$ , and devices with these sensitivities have been constructed.<sup>30</sup> These extremely low noise levels are achieved by limiting the dynamic range and avoiding feedback. The need for practical (useful) devices requires that feedback be used and that the SQUID electronics has a reasonable dynamic range. Commercially available LTS dc SQUIDs have noise levels of  $10^{-31}$  J/Hz.

### 2. Temperature dependence

Due to the strong temperature dependence of superconducting properties, such as energy gap  $\Delta(T)$ , critical current  $I_c$ , surface resistivity  $R_s$ , etc., especially near  $T_c$ , we find that basic SQUID parameters such as bias and modulation drives will experience variations as a function of temperature. This increases with frequency up to the frequency whose energy

corresponds to the superconducting energy gap [ $\Delta(T)$ , the energy needed to decouple the paired electrons].

The best noise performance is obtained when the SQUID is operated at or below  $\frac{1}{2}T_c$ . A niobium LTS SQUID operating at 4.2 K has  $T/T_c=0.44$ , while a YBCO SQUID at 77 K has  $T/T_c=0.83$ . Operating at lower temperatures also means potentially lower noise [Eq. (2)]. A significant temperature variation may require retuning for optimum performance. A typical LTS SQUID [e.g., Figs. 14(c) and 14(d)] will have a temperature variation of  $\sim 0.1\Phi_0/K$ ; a HTS device [Fig. 5(f)] has  $d\Phi/dT \approx 0.015\Phi_0/K$ . Because liquid cryogenes are normally used to cool SQUID devices, ambient pressure and pressure variations can change the cryogen temperature with a commensurate change in SQUID operating parameters. For example, geophysical applications may require operation in deep mines, underwater, or at altitude (airborne). A 1 torr pressure variation at 760 torr is equivalent to a 1.5 mK change in the temperature of a liquid helium bath and a 11 mK change in the temperature of a liquid nitrogen bath. Use of a closed cycle refrigerator (Sec. VI B) can cause significant temperature variations ( $\pm \frac{1}{2}$  K at 1 Hz for a 4 K GM cycle cryocooler). A temperature controller or a large thermal mass (or both) may be needed to smooth out these variations.

### 3. Field dependence

In normal operation, LTS SQUIDS are operated in the Earth's magnetic field ( $\sim 50 \mu\text{T}$ ) or lower environments. LTS experiments requiring operation in high fields usually employ coils that transport the measured flux or currents to the LTS SQUID sensor located in a low field region of the cryostat (typically less than 10 mT).

Because HTS coils are located on the same substrate as SQUID itself (or next to in the case of a flip-chip design<sup>9</sup>), the HTS SQUIDS are subjected to the environment being measured. It should be noted that some bicrystal SQUIDS have  $I_c(H)$ 's that oscillate with  $\Phi_0/2$ .<sup>31</sup> Some HTS devices simply will not function in fields exceeding tens of microtesla. In addition, the decreased flux pinning in HTS devices at high fields results in reduced slew rates. The development of ramp edge junctions<sup>9</sup> has allowed HTS devices to operate in fields up to 0.1 T with white noise scaling as  $\sqrt{H}$ .

Both LTS and HTS devices should be operated in very stable fields. For LTS sensors, placing them inside a niobium provides a highly stable local field environment. Since HTS devices are usually configured for measuring external fields, it is not realistic to place a HTS SQUID in a HTS shield (unless it is large enough to encompass the entire object being measured.<sup>32</sup> Instead, attention must be paid to reducing external field influences on the SQUID sensor (Sec. IV B).

### 4. $1/f$ noise

Along with white noise, there exists a frequency dependent contribution that increases as the frequency decreases (Fig. 14; note that the variation is  $1/f$  in energy, not field). The onset of this " $1/f$ " noise can be dependent on the ambient magnetic field when the SQUID sensor is cooled. Cooling the SQUID sensor in low ambient magnetic fields (less than  $1 \mu\text{T}$ ) may significantly improve the  $1/f$  performance, particularly with HTS SQUIDS using grain boundary junc-

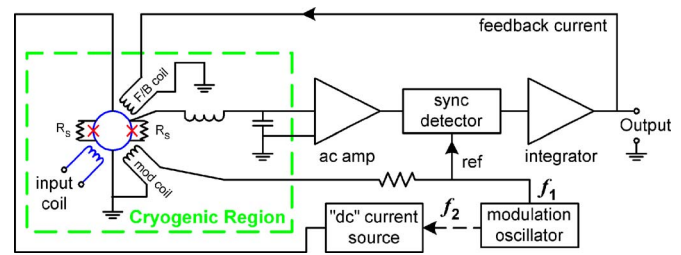


FIG. 15. (Color online) ac biasing. The modulation oscillator is used to chop the dc bias current at a frequency typically twice that of the modulation frequency (here  $f_2=2f_1$ ).

tions. It should be noted that measurements of  $1/f$  noise, usually taken at frequencies well below 1 Hz, are difficult. The SQUID sensor should be placed in a superconducting can, which is itself inside mu-metal shielding. Care should be taken to eliminate any potential mechanical motion. As vibration often appears as a  $1/f^2$  contribution, excessive low frequency noise may be identified by its spectral content.

### 5. Sources of $1/f$ noise

Thermally activated critical current fluctuations due to trapping and release of electrons in the barrier produce fluctuations in the (Josephson) energy gap  $\Delta(T)$  with variations in  $I_c$ . A large contribution to this noise in some dc SQUIDS can arise from the presence of the dc current bias. By chopping the dc bias (Fig. 15) in combination with the conventional flux modulation techniques, it is possible to reduce this added  $1/f$  noise.

This ac bias reversal approach,<sup>33</sup> sometimes referred to as dynabias, separates the original signal wave form from the noise associated with the dc bias and can reduce  $1/f$  noise at very low frequencies [Figs. 14(b) and 14(c)]. As mentioned in Sec. II A, the first commercial dc SQUIDS exhibited excessive  $1/f$  noise. The use of ac biasing<sup>33</sup> lowered the  $1/f$  knee (the frequency where the  $1/f$  noise equals the white noise) by nearly two orders of magnitude. Present day LTS SQUIDS use  $\text{AlO}_x$  barriers that do not exhibit this excessive  $1/f$  noise (ac biasing does not seem to further reduce  $1/f$ ). HTS SQUIDS exhibit temperature dependent critical currents and flux noise that arise from motions of flux lines trapped in the HTS material. Both of these effects cause  $1/f$  noise. The  $1/f$  noise due to critical current variations can be significantly reduced by the use of ac biasing. Flux noise fluctuations have not been able to be reduced by any known modulation scheme. Commercially available LTS SQUIDS have  $1/f$  knees of 0.1–0.5 Hz; HTS SQUIDS have  $1/f$  knees in the 5–20 Hz range.

The modulation signal can be distorted due to time delays, phase shifts, and attenuation from circuit elements between the modulation oscillator and the modulation coil on the SQUID chip. This can increase noise and reduce bandwidth. Many commercial SQUID electronics have a skew control that adds a small phase shifted signal at the same frequency as the modulation signal. This (skew) signal can be used to symmetrize the modulation signal presented at the SQUID loop improving the system performance. It should be noted that bias reversal limits the maximum bandwidth to less than half the bias reversal frequency.

Temperature variations of the SQUID can also cause  $1/f$  behavior (via  $d\Phi/dT$ , Sec. III C 2). If the SQUID is directly immersed in a liquid cryogen, stabilizing the bath temperature can be critical to minimizing temperature variations. Convection cells in the helium can be a major problem at low frequencies.<sup>34</sup> Movement of liquid cryogens can also induce temperature instabilities. One liquid nitrogen Dewar was found to have a temperature stability best described as  $\delta T = (1.9 + 1.9/T) \times 10^{-4} \text{ K}/\sqrt{\text{Hz}}$ .<sup>35</sup>

#### D. Control electronics

One important factor of SQUID design is that the feedback electronics must be able to follow changes in the shielding currents. If the shielding current changes so fast that the flux in the SQUID loop changes by more than  $\Phi_0/2$ , it is possible that the feedback electronics will lag behind the rapidly changing flux. When the electronics finally “catch up,” they can lock on an operating point (Fig. 12) different from the original. In this case, the SQUID has “lost lock” because the SQUID has exceeded the maximum slew rate of the electronics. This places an upper limit on the bandwidth of the system. Slew rate means not just the ability to track a signal at a single frequency (e.g., 60 Hz), but the ability to track signals at frequencies within the bandwidth of interest. The typical bandwidth of commercially available SQUID systems is dc to 50+ kHz. Custom electronics have been built extending bandwidths above 3 MHz.<sup>25</sup> Typical slew rates for commercial electronics are in the range of  $10^5$ – $10^6 \Phi_0/\text{s}$  for a single pure frequency. Complex wave forms may generate intermodulation distortion that will have the effect of reducing the effective slew rate. It should be noted that slew rates for HTS devices can be significantly less (1/10–1/100) than theoretically possible. This may be due to flux motion and other limitations inherent to HTS materials.

Even though one may not need or want to observe rapidly changing signals, situations may arise when ambient noise (e.g., 60 Hz) may determine the slew rate requirements of the system. To recover a signal from such interference, it is necessary that the system be able to track all signals present at the input, including the noise. When system response is sped up to handle very fast signals, sensitivity to rf interference and spurious transients is also increased. Since the ability to remain locked while subjected to strong electrical transients is greatest when the maximum slew rate is limited (slow), while the ability to track rapidly varying signals is greatest when the maximum slew rate is greatest (fast), it is desirable to be able to match the maximum slew rate capability to the measuring situation. As a matter of convenience, many commercial SQUID systems offer user selectable slew rates along with high-pass and low-pass filters for noise reduction.

#### E. Limitations on SQUID technology

When utilizing SQUID-based measurement systems and data reduction algorithms, it is important to bear in mind several fundamental limitations:

#### 1. Differential measurements

SQUIDs are sensitive to relative (field or current) changes only. This is a consequence of the fact that the output voltage of a SQUID is a periodic function [Fig. 7(b) or 12] of the flux penetrating the SQUID loop. The SQUID is “flux locked” on an arbitrary point on the  $V$ - $\Phi$  curve, and the SQUID output is sensitive to flux changes relative to this lock point.

#### 2. Slew rate limitations

If the signal changes faster than the feedback electronics can follow (i.e., the slew rate is exceeded) and the total signal change exceeds  $\frac{1}{2}\Phi_0$ , it is possible for the operating point to shift by one or more flux quanta (Fig. 7 or 12). If high bandwidths are needed, it is possible to operate the electronics in a limited range mode where the raw output is amplified without use of a feedback signal. Although the SQUID has an intrinsic bandwidth of several gigahertz, when operated with standard flux-locked loop electronics using ac flux modulation, the maximum usable bandwidth of most commercially available electronics is typically 50–100 kHz.

#### 3. $1/f$ noise

Another limitation is the presence of  $1/f$  noise. The use of ac biasing in HTS SQUIDs limits their maximum bandwidth to less than half the bias reversal frequency. If the bias reversal frequency is too high, noise can be induced due to voltage spikes in the transformer coupled preamplifier input circuit. Because of this, the maximum bandwidth of commercially available HTS SQUIDs is usually limited to  $\sim 50$  kHz. If MHz bandwidths are required, the ac bias is not used; however, there will be excess noise below 1 kHz.

#### 4. The vector nature of SQUID magnetometers

SQUID magnetometers are vector magnetometers. For a pure magnetometer operating in the Earth’s magnetic field ( $\sim 50 \mu\text{T}$ ), a  $180^\circ$  rotation can sweep out a total field change of up to  $100 \mu\text{T}$ . If the magnetometer has a sensitivity of  $10 \text{ fT}/\sqrt{\text{Hz}}$ , tracking the total field change requires a dynamic range of  $100 \mu\text{T}/10 \text{ fT} = 200 \text{ dB}$ , well beyond the capabilities of current electronics. In addition, the rotational speed must not cause the current flowing through the SQUID sensor to exceed its slew rate limitations. Pure gradiometers (Sec. IV F) would be insensitive to uniform fields and not suffer this dynamic range limitation. In reality, gradiometers are not perfect and have some magnetometer components [Eq. (7)] that can place motion restrictions even on well-balanced gradiometers.

### IV. INPUT CIRCUITS

#### A. Packaging

Although it is possible to couple magnetic flux directly into the SQUID loop, environmental noise considerations (Sec. VI) make this difficult, if not impossible, in an unshielded environment. In addition, the area ( $A = \pi r_{\text{coil}}^2$ ) of a typical SQUID loop is small ( $< 0.1 \text{ mm}^2$ ), and its resulting sensitivity to external flux changes ( $\Delta\Phi = A\Delta B$ ) little. Although a larger loop diameter would increase the SQUID’s

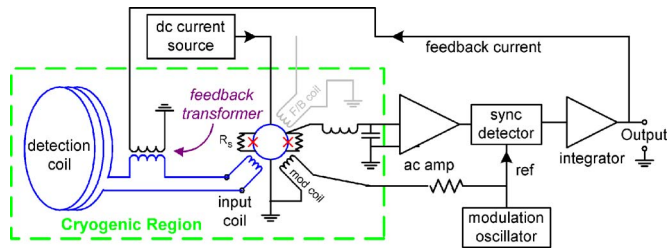


FIG. 16. (Color online) External feedback circuit. Note that the internal feedback circuitry (shown in Fig. 13) is not used.

sensitivity to external flux, it would also make it much more susceptible to environmental noise. For this reason, external flux is normally inductively coupled to LTS SQUID loops by a flux transformer. Because HTS devices have the detection coil grown on the same substrate, the Josephson loop is exposed to the environment being measured. This limits the ability of HTS devices to operate in high fields (Sec. III C 3).

The packaging of the sensor should be sufficiently rugged to allow use under adverse conditions. A niobium can shield LTS devices from external fields  $>20$  mT. If an experiment requires high fields, it is desirable to use a magnet with a compensation coil that generates a null ( $<20$  mT) field region. The SQUID sensor is placed there and connected to the experiment by twisted pair(s) of NbTi leads for field  $<10$  T. Nb<sub>3</sub>Sn leads may permit superconducting connections in fields above 20 T. When stored at room temperature, HTS devices require isolation from humid environments to prevent degradation of the YBCO film. Normally, a surface passivation layer over the YBCO is combined with encapsulating the HTS SQUID in a gas filled sealed G-10 or plastic enclosure.

To improve immunity to external sources in LTS systems, it is advisable to run the connecting leads [between the detection coil(s) and SQUID input] through superconducting tubes. While niobium tubing can be used, a much less expensive method is to remove the rosin core center of a 60/40 lead-tin solder. The resulting hollow tubing can be used as a superconducting shield below 6 K. Care must be taken so that the common mode from the tube does not exceed the common mode from the bare twisted wire. For HTS devices—if large coils are part of the device's structure—designing YBCO ground planes above and below the interconnects will help to reduce extraneous pickup (and improve balance (Sec. IV F) in the case of planar gradiometers).

Today, SQUIDs are fabricated as planar devices rather than point contacts [Fig. 5(a)] or Dayem bridges [Fig. 5(b)] used to fabricate early rf SQUIDs. In this configuration, the superconducting loop, Josephson junctions, and coils (input, feedback, and modulation) are patterned on the same device. Multilayer deposition techniques are used (primarily in LTS devices), and coils are normally in the form of a square washer.<sup>19</sup> The planar configuration leads to quite small devices, occupying only a few mm<sup>3</sup> compared to 5+ cm<sup>3</sup> (1.2 cm diam  $\times$  5 cm) for older toroidal rf SQUIDs.<sup>36</sup> Another advantage of the planar device is that it is possible to have the detection coils as part of the SQUID sensor, eliminating the need for separate (three-dimensional) detection

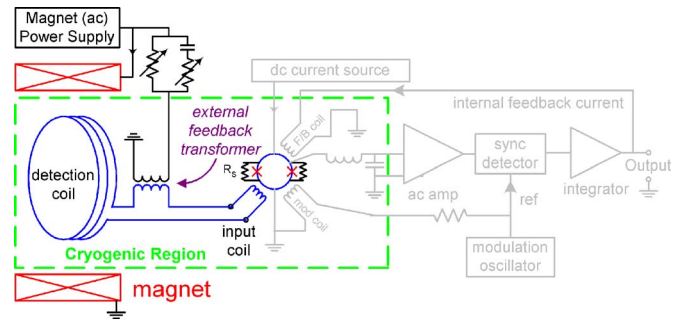


FIG. 17. (Color online) ac susceptibility system using external feedback. The external feedback signal is generated (in parallel to the internal feedback in this example) to the magnet power supply and then attenuated before being fed into the input circuit. The capacitive circuit element generates the quadrature signal.

coils. Such an integrated sensor can significantly reduce the complexity of multichannel systems.

## B. External feedback

Normally, SQUID electronics utilize an internal feedback technique to cancel changes in magnetic flux. An alternate approach to feedback may be made by coupling the feedback signal to the input coil [Fig. 16(a)] rather than to the Josephson loop. This can avoid large feedback currents (e.g., due to 50 or 60 Hz) that could exceed  $I_c$  for the Josephson junction(s).

A second method (Fig. 17) uses an externally generated signal in addition to the SQUID feedback electronics. One example is a circuit to compensate for an external ac field being applied near the detection coil(s) in a susceptibility experiment.

Another variation is where an external feedback signal (for real-time noise reduction) is generated by the output of reference channels (Sec. IV G). This method is normally used in parallel with internal feedback. When this technique is used, it may be necessary to null both the in-phase and quadrature feedback signals. This can be done manually or by computer control.

When calculating the sensitivity of the detection coil, the portion of the external feedback coil that is in series with the detection and input coils must be added to calculate the total inductance [Eq. (5)]. Care must be taken in constructing the external feedback coil and the leads that connect the coil. The major consideration is to avoid the introduction of potential rf interference into the external feedback coil. Shielding the leads, magnetically isolating the external feedback coil from the signal (or potential noise sources), and proper attention to grounding will reduce the chances of problems.

## C. The SQUID as a black box

Whether a rf or dc SQUID, a SQUID system can be considered as a black box that acts like a current (or flux)-to-voltage amplifier with extremely high gain. In addition, it offers extremely low noise, high dynamic range ( $>140$  dB), excellent linearity ( $>1:10^7$ ) and a wide bandwidth that can extend down to dc. A SQUID can also be used as a postam-

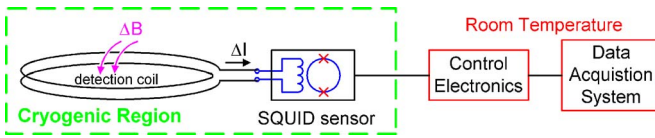


FIG. 18. (Color online) Schematic diagram of typical SQUID input circuit.

plifier stage<sup>37</sup> offering superior performance to conventional field effect transistors at frequencies as high as 500 MHz.

Conceptually, the easiest input circuit to consider for detecting changes in magnetic fields is that of a SQUID sensor connected to a simple superconducting coil (Fig. 18). Since the total flux in a superconducting loop is conserved, any change in external field through the signal coil will induce a current in the flux transformer that must satisfy

$$\Delta\Phi = NA\Delta B = (L_{\text{coil}} + L_{\text{input}})\Delta I, \quad (3)$$

where  $\Delta B$  is the change in applied field;  $N$ ,  $A$ , and  $L_{\text{coil}}$  are the number of turns, area, and inductance of the detection coil, respectively  $L_{\text{input}}$  is the inductance of the SQUID input coil; and  $\Delta I$  is the change in current in the superconducting circuit. If the lead inductance is not negligible, it must be added to  $L_{\text{coil}}$  and  $L_{\text{input}}$ . Typically, a twisted pair of 0.005 in. NbTi wire has  $L_{\text{lead}} \approx 0.3 \mu\text{H/m}$ .

#### D. Sensitivity

Maximum sensitivity is almost never the optimum sensitivity. Nevertheless, an understanding of the techniques used to maximize sensitivity is essential to any discussion of optimum sensitivity. Since the SQUID system has an output that is proportional to the input current, maximum sensitivity is obtained by using the input circuit that provides the maximum current into the SQUID and satisfies all other constraints of the experimental apparatus.

A common constraint is the physical size of the detection coil. As is seen in Eqs. (3) and (4), it is clear that maximum sensitivity to uniform fields is obtained with an infinitely large coil. Infinitely large coils fit quite nicely into Dewars with infinitely large necks, but they have the serious disadvantage of boiling off liquid cryogenes at an infinitely fast rate. If ultimate sensitivity is needed, common practice would be to build the largest diameter detection coil that will fit in a physically realistic Dewar neck.

Another constraint on coil design is spatial resolution that is dependent on the nature of the source, the geometry of the detection coil, and the distance between the coil and the source. If nearby objects are to be measured (e.g., biomagnetism or magnetic microscopy), then spatial resolution may be more important than absolute sensitivity. In fact, dipole field sensitivity can go up for smaller coils that are very close to the object being measured.

In the near field region, where the distance to the detection coil is less than a coil diameter from the detection coil(s)—assuming reasonable signal-to-noise ratio the spatial resolution can be better than 1/10th the coil diameter. Multiple or higher order (quadruple, etc.) sources may have spatial resolution on the order of the coil diameter. One rule of thumb is not to have the coil diameter significantly less than the distance between the coil and the source. This distance

includes the tail spacing (gap) of the Dewar (Fig. 25) used to provide the cryogenic environment. Application specific analyses are given in Secs. IX B and X B.

In the far field approximation, where the distance from the detection coil is many coil diameters, spatial resolution may be multiples of the coil diameter. In that situation, larger coils are recommended. However, it makes no sense to design coils for significantly higher sensitivity than environmental constraints (noise) permit.

To calculate the sensitivity and noise levels of a simple detection coil system, the inductance of the detection coil must be known. The inductance of a flat, tightly wound, circular multiturn loop of superconducting wire is given (in mks units) by<sup>38</sup>

$$L = \mu_0 N^2 r \left[ \log_e \left( \frac{8r_{\text{coil}}}{r_{\text{wire}}} \right) - 2 \right], \quad (4)$$

where  $\mu_0$  is the magnetic permeability of free space,  $r_{\text{coil}}$  is the radius of the detection coil, and  $r_{\text{wire}}$  is the radius of the (superconducting) wire. Knowing the coil inductance  $L_{\text{coil}}$ , we can rewrite Eq. (3) as

$$\Delta B = (L_{\text{coil}} + L_{\text{input}})\Delta I/NA. \quad (5)$$

Since the SQUID system has an output proportional to the input current, maximum sensitivity is obtained by using the input circuit that provides the maximum current into the SQUID and satisfies all other constraints of the experimental apparatus. For a pure magnetometer of a given diameter, the maximum sensitivity will occur when the impedance of the detection coil matches that of the SQUID sensor ( $L_{\text{coil}} = L_{\text{input}}$ ).

Much higher sensitivity ( $10^{-17} \text{ T}/\sqrt{\text{Hz}}$ ) in a limited bandwidth (100 Hz in this case) has been achieved by incorporating a rf SQUID [Fig. 14(a)] into a parametric amplifier circuit.<sup>39</sup> Substituting a present day dc SQUID sensor could yield a sensitivity of  $<3 \times 10^{-18} \text{ T}/\sqrt{\text{Hz}}$ . The highest sensitivity reported for a HTS SQUID magnetometer is  $3.5 \times 10^{-15} \text{ T}/\sqrt{\text{Hz}}$ .<sup>40</sup>

#### E. Detection coils

Several factors affect the design of the detection coils.<sup>41</sup> These include the desired sensitivity of the system, the size and location of the magnetic field source or current dipole<sup>42</sup> (Sec. X A 1), and the need to match the inductance of the detection coil to that of the SQUID. The ability to separate field patterns caused by sources at different locations and strengths requires a good signal-to-noise ratio. At the same time, one has to find the coil configuration that gives the best spatial resolution. Unfortunately, these two tasks are not independent. For example, increasing the signal coil diameter improves field sensitivity (to uniform fields or distant sources), but sacrifices spatial resolution. In practice, system design is restricted by several constraints: the impedance and noise of the SQUID sensors, the size of the Dewar, and the number of channels, along with the distribution and strength of noise sources.

It is extremely important for dc response that the detection coil(s) be superconducting. Resistance in the detection circuit has two effects: (1) attenuating the signal and (2)

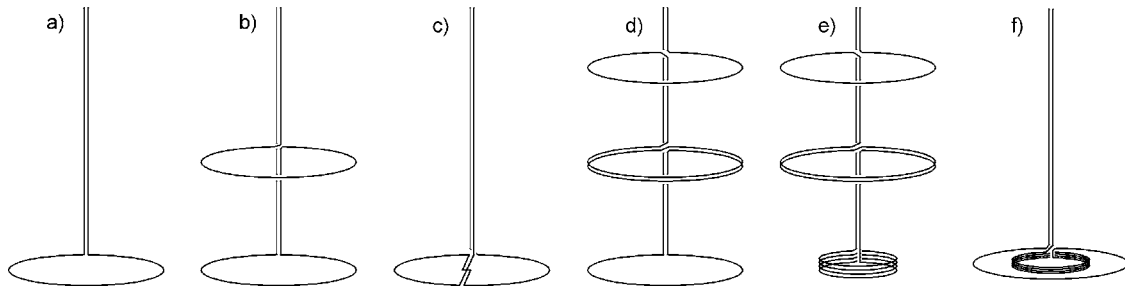


FIG. 19. (a) Magnetometer; (b) first derivative axial gradiometer; (c) first derivative planar gradiometer; (d) second derivative axial gradiometer; (e) second derivative asymmetric axial gradiometer; (f) first derivative radial gradiometer.

adding the Nyquist noise. Resistive attenuation is important only below a frequency  $f_0$ , such that the resistive impedance is equal to the sum of the inductive impedances in the loop (e.g.,  $f_0 \approx R/L_{\text{tot}}$ , where  $L_{\text{tot}}$  is the total inductive impedance of the loop). Resistive noise is only important if it becomes comparable to other noise sources or the signal ( $<10^{-30}$  J/Hz for biomagnetism;  $<10^{-26}$  J/Hz for geophysics). For a SQUID with  $E_N \sim 10^{-30}$  J/Hz, the total resistance of the circuit, including any joints, must be less than  $10^{-13}$   $\Omega$ .<sup>17</sup> Thus it is very important that all solder joints, press fits, or connections have as low a joint resistance as possible.

Figure 19 displays a variety of detection coils. The magnetometer [Fig. 19(a)] responds to the changes in the field penetrating the coil. More complicated coil configurations provide the advantage of discriminating against unwanted background fields from distant sources while retaining sensitivity to nearby sources.

Because of the present inability to make flexible (i.e., small bending radius) wire or make true superconducting joints in HTS materials, commercially available HTS devices are currently in the form of magnetic sensing rather than current sensing devices.

## F. Gradiometers

Magnetometers are extremely sensitive to the outside environment. This may be acceptable if one is measuring ambient fields. If what is to be measured is close to the detection coil and is weak, outside interference may prevent measurements at SQUID sensitivities. If the measurement is of a magnetic source close to the detection coil, a gradiometer coil may be preferred. Since  $B_{\text{dipole}} \propto 1/z^3$ , where  $z$  is the distance beneath the coil, it follows that the field from a distant source is relatively uniform in direction and magnitude at the sensor. If we connect in series two identical and exactly parallel loops wound in opposite senses, separated by a distance  $b$  (the base line), we obtain a coil [Fig. 19(b)] that will reject uniform fields.

Since the response of a single coil to a magnetic dipole goes as  $1/z^3$ , an object that is much closer to one coil than the other will couple better to the closer coil than to the more distant one. Sources that are relatively distant will couple equally into both coils. For objects that are closer than  $0.3b$ , the gradiometer acts as a pure magnetometer, while rejecting more than 99% of the influence of objects more than  $300b$  distant (Fig. 20). In essence, the gradiometer acts as a com-

pensated magnetometer. It is possible to use two gradiometers connected in series opposition [Fig. 19(d)] to further minimize the response of the system to distant sources. This can be extended to higher orders by connecting in series opposition two second order gradiometers, etc. Doing so, however, reduces the sensitivity of the instrument to the signal of interest (Fig. 21) and may not significantly improve the signal-to-noise ratio (this applies only to hardware gradiometers, not to electronic gradiometers).

Rejection of distant noise sources depends on having a precise match (or balance as it is sometimes referred to) between the number of area turns in the coils. A symmetric gradiometer [Fig. 19(b)] requires that  $N_{\text{signal}}A_{\text{signal}} = N_{\text{comp}}A_{\text{comp}}$ , where  $N$  is the number of turns and  $A$  the area of the signal and compensation coils, respectively. Thus  $L_{\text{coil}}$  in Eq. (5) becomes  $(L_{\text{signal}} + L_{\text{comp}})$ . An asymmetric design [Fig. 19(e)] has the advantage that the inductance ( $L_{\text{signal}}$ ) of the signal coil(s) can be much greater than the compensation coils ( $L_{\text{comp}}$ ); greater sensitivity is achieved than with a symmetric design. Another advantage is that the signal coil diameter is reduced, leading to potentially higher spatial resolution. Another way to reduce the inductance of the compensation coils is to physically separate the windings of the compensation turns so that they act as  $N$  single turns ( $L_{\text{comp}} \approx NL_{\text{single turn}}$ ) in series rather than a single tightly packed coil ( $L_{\text{comp}} \approx N^2L_{\text{single turn}}$ ). The optimum conditions for the number of turns in an asymmetric signal coil is given by<sup>43</sup>

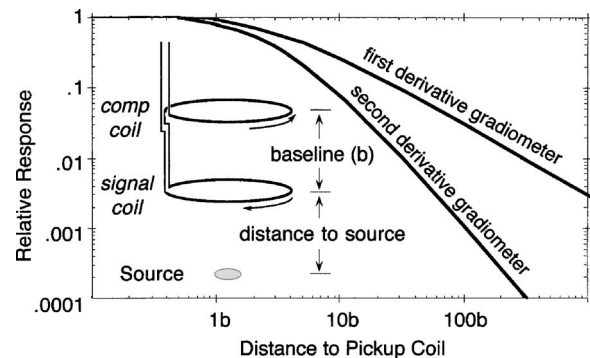


FIG. 20. Response of gradient coils relative to magnetometer response ( $1/z^3$  suppressed).

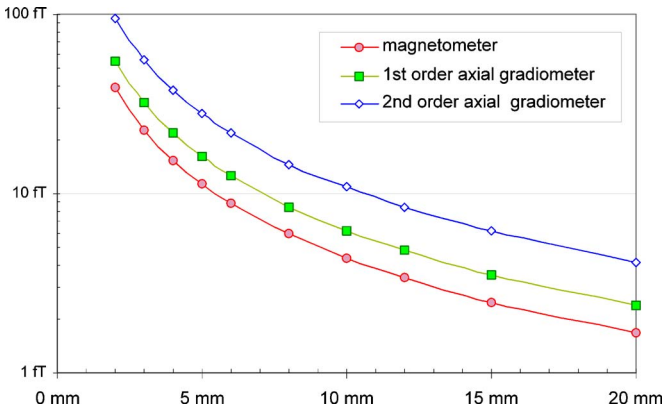


FIG. 21. (Color online) Sensitivity/ $\sqrt{\text{Hz}}$  vs coil diameter for different detection coil designs.  $L_{\text{SQUID}}=2 \mu\text{H}$ ,  $\Phi_{\text{noise}}=5 \Phi_0/\sqrt{\text{Hz}}$ ; base line= $5 \times$  coil diameter; lead length (from SQUID sensor to detection coil) =300 mm.

$$(L_{\text{signal}} + L_{\text{comp}} + L_{\text{input}} + L_{\text{leads}}) - N_{\text{signal}} \frac{\partial}{\partial N_{\text{signal}}} \times (L_{\text{signal}} + L_{\text{comp}} + L_{\text{input}} + L_{\text{leads}}) = 0. \quad (6)$$

If the gradiometer is perfectly made (balanced), it will reject uniform fields. However, if one coil has a larger effective diameter than the other, the response will not be that of a perfect gradiometer, but that of a gradiometer in a series with a “smaller” magnetometer. Mathematically, the balance  $\beta$  can be defined as

$$V_t \propto \mathbf{G} + \beta \cdot \mathbf{H}, \quad (7)$$

where  $V_t$  is the system response,  $\mathbf{G}$  is the coil’s response to a gradient field (e.g.,  $dB_z/dz$ ), and  $\mathbf{H}$  is the applied uniform field. If the coils are coplanar, there should not be any  $x$  or  $y$  field components detected. However, the reality of fabrication (e.g., tilt due to coil forms constructed from multiple pieces, imperfect machining, etc.) is such that there may be  $\beta$ ’s with  $x$  and  $y$  components.

Typically, coil forms used to wind gradiometers can be machined (grooved) to achieve balances that range from  $\beta = 0.01 \sim 0.001$ . Planar devices, fabricated using photolithography, can achieve significantly higher balances—a factor of 10 or better. Superconducting trim tabs<sup>44</sup> placed within the detection coils can improve  $\beta$  to the ppm level. High degrees of balance can allow a SQUID gradiometer to operate in relatively large (millitesla) ambient fields while maintaining sensitivities in the tens of femtotesla. The use of electronic balancing (Sec. IV F) can provide balance ratios at the ppm level.<sup>45</sup>

## 1. Sensitivity

To use a SQUID magnetometer or gradiometer as a quantitative instrument, it is necessary to properly calibrate the output voltage-measured magnetic field relationship. A small coil located under the detection coil (e.g., the “source” in Fig. 20) can easily be used for calibration purposes. Other possible calibration sources include a large coil or straight wire.<sup>46</sup> A meander path of two small diameter wires next to each other with current flows in opposite directions can be used to determine spatial resolution in magnetic microscopes (Sec. IX C).

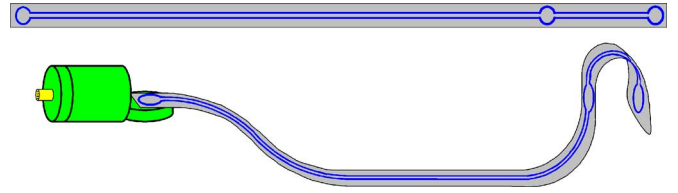


FIG. 22. (Color online) HTS patterned tape on flexible substrate (upper). HTS tape bent into axial gradiometer configuration. The flux is transported and inductively coupled to a  $90^\circ$  oriented HTS SQUID magnetometer (lower).

When comparing magnetometers and gradiometers, the typical basis for comparison is to assume that the source is relatively close to the signal coil(s) and the effect of the compensation coils can be neglected. Unless otherwise specified, this assumption will be used for all comparisons in this article.

## 2. Other design considerations

The design of the detection coil is dependent on the sensitivity and the spatial resolution required to measure the object(s) of interest. Coil optimization is not just that coil gives the maximum magnetic field sensitivity. Use of field sensitivity is a good metric if the object is in the far field approximation ( $z_{\text{source}} \gg r_{\text{coil}}$ ). Geophysical measurements (e.g., magnetotellurics, Sec. VIII A) are an example where field sensitivity is the determining measurement parameter.

The input impedance of the SQUID sensor will also affect coil design. As mentioned earlier, optimum sensitivity (for a magnetometer) occurs when  $L_{\text{coil}}=L_{\text{input}}$ . A small inductance (e.g.,  $0.2 \mu\text{H}$ ) SQUID may be the proper choice for millimeter diameter detection coils, whereas a  $2 \mu\text{H}$  SQUID is better suited for a larger (e.g., centimeter diameter) coil where femtotesla sensitivity is desired.

If spatial resolution is important (e.g., in paleomagnetism, Sec. VIII C; nondestructive testing, Sec. IX; or biomagnetism Sec. X), then the object must be in close proximity to the detection coil(s). Near field analysis should be performed to determine the optimum coil design. Optimization for magnetic dipoles is discussed in Sec. IX B; optimization for current dipoles is discussed in Sec. X B. It should be noted that if the source is much closer to the signal coil than a coil diameter ( $z_{\text{source}} \ll r_{\text{coil}}$ ), increasing the coil diameter may not increase the detected signal.

In addition to determining the optimum coil diameter and sensitivity, environmental noise considerations (Sec. VI) may require the use of gradiometers. Normally, gradiometers suffer from a loss in sensitivity due to the added inductance of the compensation coil (Fig. 20). It should be noted that, for small diameter coils where the inductance of the coil is significantly less than that of the SQUID sensor, a gradiometer may have nearly the same sensitivity as a magnetometer. This may be of interest in situations where ultimate sensitivity is less important than noise rejection. Figure 21 shows the relative sensitivities for a magnetometer along with first and second order symmetric gradiometers where the number of turns (at a given diameter) is optimized to match the total coil inductance to that of the SQUID sensor [Eq. (5)].

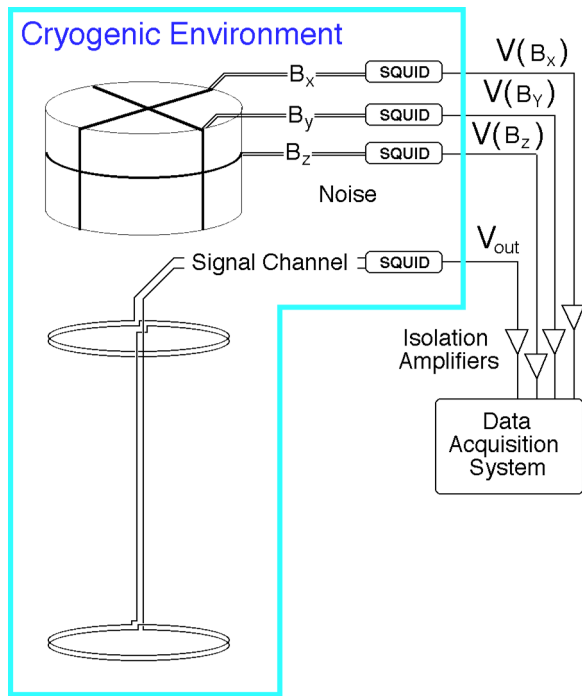


FIG. 23. (Color online) First order gradiometer with three noise cancellation channels.

As can be seen, a larger diameter yields greater sensitivity (unless  $z_{\text{source}} \ll r_{\text{coil}}$ ). However, larger diameter coils will have poorer spatial resolution. An asymmetric first order gradiometer [similar to Fig. 19(e)] would lie between the magnetometer and the (symmetric) first order gradiometer.

### 3. HTS gradiometers

Because of the inability to make flexible wire or make superconducting joints in HTS materials, present day HTS magnetometers are fabricated as planar devices and are available as pure magnetometers [Fig. 19(a)] and planar gradiometers [Fig. 19(c)]. It is possible to use a thick film patterned (as a planar gradiometer) HTS tape and bend it (Fig. 22) to form an axial gradiometer.<sup>47</sup> It should be noted that there will be substantial gradiometer imbalance [Eq. (8)].

### G. Electronic and software noise cancellation

Portions of (additional) magnetometer reference channel response(s) can be summed electronically with the gradiometers' input to balance out its effective magnetometer response. The simplest scheme is to use a second  $B_z$  magnetometer coil and subtract its output,  $V(B_z)$ , from the output of

the gradiometer,  $V_t$ . The actual output is attenuated (by a factor  $b$ ) as to exactly cancel the imbalance ( $\beta$ ) of the gradiometer. By adjusting  $b V(B_z)$  to equal  $\beta \cdot H$ , the net result goes to  $G$ . Since there can be imbalance in the  $x$  and  $y$  components, a three-axis set of coils (Fig. 23) allows compensation of the  $B_x$ ,  $B_y$ , and  $B_z$  components.

In addition to field noise, gradient fields generated by distant sources can be large enough to mask the signals being measured. Additional improvement can be achieved by the addition of a second gradiometer compensation channel. Thus the system output [using the notation of Eq. (7)] can be described as

$$V_{\text{out}} \propto \mathbf{G} + \beta \cdot \mathbf{H} + b_1 V(B_x) + b_2 V(B_y) + b_3 V(B_z) + g_4 V(G_z), \quad (8)$$

where  $b_1$  is the weighting for the  $B_x$  component,  $b_2$  is the weighting for the  $B_y$  component,  $b_3$  is the weighting for the  $B_z$  component, and  $g_4$  is the weighting for the gradient reference component  $G_z$  ( $dB_z/dz$ ).

As an example, the use of three reference magnetometers ( $B_x$ ,  $B_y$ , and  $B_z$ ) gave an attenuation of externally generated noise of 12 dB for an axial gradiometer (Fig. 23).<sup>48</sup> The addition of an external gradient reference channel improved noise rejection to better than 40 dB. The gradient channel should be located sufficiently far from the sources being measured so as not to detect significant signals, but close enough so that it essentially sees the same gradient noise. Moving the reference gradiometer 1 m away from the signal coil reduced noise rejection by a factor of 4 (12 dB).

Even simple subtraction algorithms can give improvements in removing common mode noise. Figure 24 shows the result of a simple subtraction algorithm ( $B_{\text{net}} = B_{\text{grad}} - B_{\text{ref}}$ ). Improvement in signal-to-noise ratio is inversely related to the degree of balance of gradiometer detection coils. A well-balanced gradiometer detection coil will show less improvement than a poorly balanced one. Efforts in improving intrinsic gradiometer balance can have significant benefits in reducing the need for electronic noise cancellation. Since the detection coil is not perfectly balanced, ideally, one should subtract all field and gradient components [expanding Eq. (8)]. To do this would require eight “noise” channels, e.g.,  $B_x$ ,  $B_y$ ,  $B_z$ ,  $dB_x/dx$ ,  $dB_y/dy$ ,  $dB_x/dy$ ,  $dB_x/dz$ , and  $dB_y/dz$ . From these components, all nine elements of the gradient tensor can be created and used to compensate for any imbalance of the detection coil(s). The use of eight-element vector/tensor arrays as reference channels can further improve external noise rejection, with rejection values

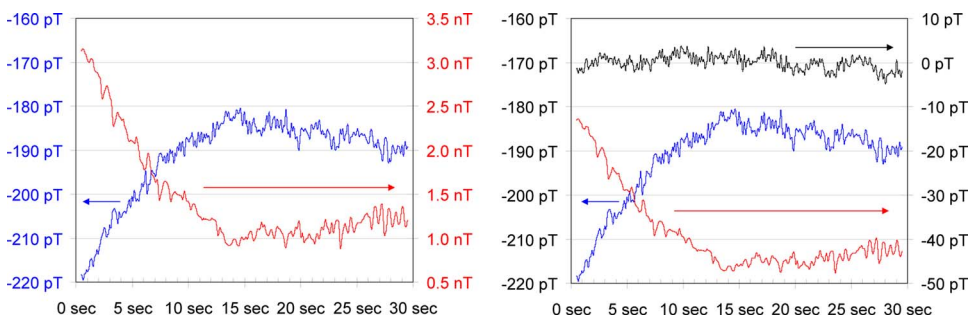


FIG. 24. (Color online) (a) Left ordinate: first order gradiometer ( $dB_z/dz$ ) low frequency drift; right ordinate: reference ( $B_z$ ) magnetometer. (b) Left ordinate: gradiometer (heavier line) and reference magnetometer (lighter line) attenuated by  $65\times$  (dc shifted by 135 pT); right ordinate: difference between gradiometer and attenuated reference magnetometer.

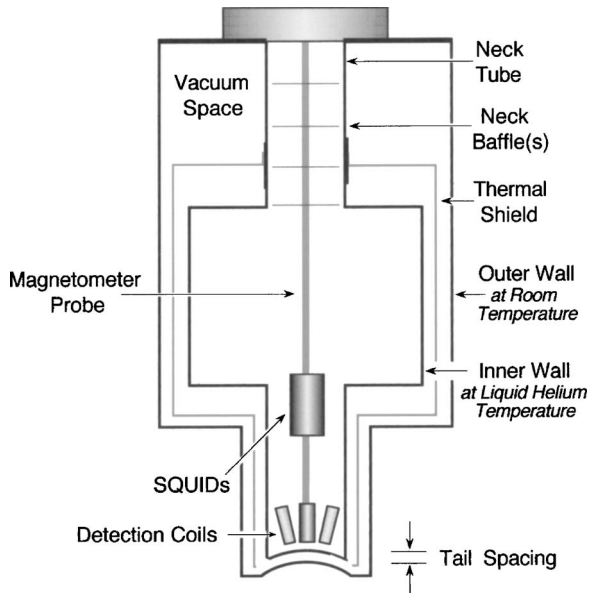


FIG. 25. Typical design of a fiber glass Dewar used for biomagnetic measurements (superinsulation not shown).

exceeding 60 dB.<sup>45</sup> A major advantage of electronic balancing is the significant improvement in immunity to low frequency environmental noise.

The simplest way to perform the noise cancellation is to simultaneously take data from the detection coil(s) and the noise channels. Then, in postprocessing, digitize the data and determine the weighting factors for each noise channel to minimize any common mode noise. One can also include time derivatives of the field and gradient components or frequency-domain components<sup>49</sup> into the cancellation algorithm to minimize effects of eddy current noise. If here is sufficient processing power, it may be possible to do real-time processing of the noise contribution by way of injection of the cancellation signals via external feedback (Sec. IV B).

While electronic noise reduction may be necessary, initial attention should be paid to gradiometer balance. Improvement in signal-to-noise ratio is inversely related to the degree of balance of a gradiometer detection coils. A well-balanced gradiometer detection coil will have less benefit from electronic noise reduction than a poorly balanced one.

Efforts in improving intrinsic gradiometer balance can have significant benefits in reducing the need for electronic noise reduction.

## V. REFRIGERATION

The major advantage of high temperature superconductivity is the simplified cryogenics and reduced spacing between cryogenic regions and room temperature. The thermal load (due to conduction and blackbody radiation) is less and the heat capacity of what needs to be cooled is larger (implying smaller temperature variations for a given heat load). Since the latent heat/unit volume of liquid nitrogen is  $\sim 60$  times larger than liquid helium, hold times become months rather than days for an equivalently sized Dewar.

### A. Dewars

The superconducting nature of SQUIDs requires them to operate well below their superconducting transition temperature (9.3 K for niobium and 93 K for  $\text{YBa}_2\text{Cu}_3\text{O}_{7-\delta}$ ). Ideally, the cryogenic environment should provide stable cooling (millikelvin or microkelvin depending on  $d\Phi/dT$  of the sensor, Sec. III C 2), have no time varying magnetic signature, be reasonably compact and reliable, and, if mechanical in nature, introduce neither a mechanical vibration nor a magnetic signature into the detection system. The thermal environment for the SQUID sensor and detection coil has typically been liquid helium or liquid nitrogen contained in a vacuum insulated vessel known as a Dewar (Fig. 25). The cryogen hold time depends on the boiloff rate (a heat load of 30 mW boils off  $\sim 1$  liter of liquid helium/day) and the inner vessel volume.

The space between the inner and outer walls is evacuated to prevent thermal conduction between the room temperature and the cryogen chambers. Within the vacuum space, a thermal shield (anchored to the neck tube) acts to reduce heat transfer by thermal (blackbody) radiation. The thermal shield can be either vapor cooled (Fig. 25)—using the enthalpy of the evaporating helium or nitrogen gas—or thermally connected to a liquid nitrogen reservoir. The evaporating gas can also be used to cool electrical connections to the SQUID sensors if the probe is immersed in the

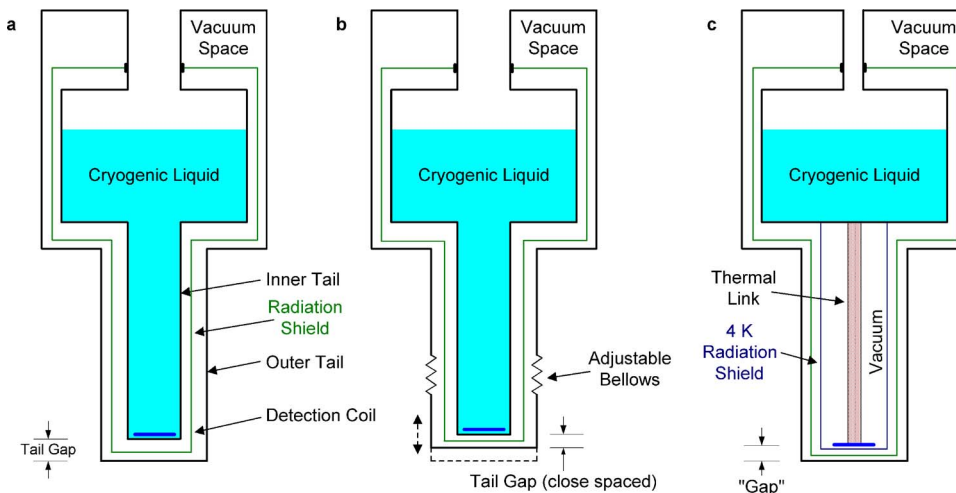


FIG. 26. (Color online) Different methods of achieving close Dewar tail spacing. Thermal shielding is omitted for clarity.

liquid cryogen [Fig. 26(a)]. Dewars with removable sections (e.g., tails) use liquid nitrogen cooled shields. Having a shield at 77 K effectively reduces the blackbody radiation by a factor of  $(300/77)^4 \approx 230$  [Eq. (9)]. Multiple layers of highly reflective aluminized Mylar® (often referred to as superinsulation) are placed between the inner and outer walls and the thermal shields to further reduce the blackbody radiation.

If the experiment involves measurements interior to the Dewar [Figs. 33(a) and 33(c)–33(e)], then a metallic Dewar is preferable. Metallic Dewars offer significant shielding from environmental noise at frequencies above 10–100 Hz. If the system is to measure magnetic fields exterior to the Dewar, the Dewar must be magnetically transparent, and metallic construction is not appropriate. Dewars for external field measurements (Fig. 25) are normally constructed of nonmetallic, low susceptibility materials to minimize their magnetic interactions with the SQUID sensors and detection coils. Materials used are typically glass-fiber epoxy composites such as G-10. To get the detection coil(s) as close as possible to the object being measured, a “tailed” design is often used. This decreases the forces on the bottom of the Dewar and allows the use of thinner end pieces (closer tail spacing). Dewars for biomagnetic measurements often have curved tails to get closer to the head, chest, or abdomen.

### 1. Fabrication

Most Dewars are built from glass/epoxy composite tubes and plates. Typically, a G-10 glass composite (similar to the material used in computer circuit boards) is used. It should be noted that properly made Dewars can last well over a decade while undergoing multiple thermal cycles. If using a mechanical or diffusion pump when pumping out the vacuum space in the Dewar walls (Fig. 25), be sure that the pumping line has a liquid nitrogen trap to avoid backstreaming the oil into the Dewar. Oil can significantly degrade the ability of superinsulation to reduce blackbody radiation (Sec. V A 1 a).

Because the vacuum space between the Dewar walls is evacuated, convection is not a significant heat load. There are three main sources of heat flux into a Dewar (besides the thermal conduction due to the SQUID lead cabling): blackbody radiation impinging on the inner portion of the Dewar vessel containing the liquid cryogen, thermal conduction down the neck tube, and 300 K blackbody radiation down the neck tube.

*a. Blackbody radiation.* Blackbody radiation ( $\dot{Q}_{\text{blackbody}}$ ) is normally the dominant heat load on a Dewar. Since the net load goes as the fourth power of the temperature [Eq. (9)], having a radiation shield at an intermediate temperature reduces the blackbody radiation by more than an order of magnitude,

$$\dot{Q}_{\text{blackbody}} = \varepsilon \sigma A (T_H^4 - T_L^4), \quad (9)$$

where  $\varepsilon$  is the emissivity of the radiating surface,  $\sigma$  is the Stefan-Boltzman constant ( $5.67 \times 10^{-8} \text{ W/m}^2 \text{ K}^4$ ),  $T_H$  is the hotter temperature, and  $T_L$  is the colder temperature. The use of multilayer superinsulation (MLI) can give significant reductions in blackbody radiation by providing tens to hun-

dreds of additional highly reflective, low emissivity surfaces between the hotter and colder surfaces. If superinsulation is used, Eq. (9) becomes<sup>50</sup>

$$\dot{Q}_{\text{MLI}} = \frac{\sigma A (T_H^4 - T_L^4)}{2(1/\varepsilon + 1/\varepsilon_{\text{MLI}} - 1) + (N - 1)(2 - \varepsilon_{\text{MLI}})/\varepsilon_{\text{MLI}}}, \quad (10)$$

where  $\varepsilon_{\text{MLI}}$  is the emissivity of the superinsulation and  $N$  is the number of superinsulation layers. In the limit where  $\varepsilon_{\text{MLI}} \ll \varepsilon$ , Eq. (10) becomes  $\dot{Q}_{\text{MLI}} = \varepsilon_{\text{MLI}} \sigma A (T_H^4 - T_L^4) / [N(2 - \varepsilon_{\text{MLI}})]$ . Care must be taken during fabrication to avoid contamination of the reflecting surfaces. Thumbprints or oil contamination can raise the emissivity of aluminized Mylar® superinsulation from  $\varepsilon_{\text{MLI}} = 0.03$  to near that of oxidized copper ( $\varepsilon \approx 0.6$ ).

*b. Thermal conduction down the neck tube and magnetometer probe.* Because most cryogenic inserts are loaded from the top of the cryostat, a sufficiently large neck tube is needed, not only to allow passage of the insert, but to support the weight of the inner vessel and liquid cryogen. The larger the neck diameter, the greater the thermal load [Eq. (11)]

$$\dot{Q}_{\text{conduction}} = \int_{T_L}^{T_H} \kappa \frac{A}{\ell} dT, \quad (11)$$

where  $\kappa(T)$  is the thermal conductivity,  $A$  is the cross-sectional area, and  $\ell$  is the length of the conductor

Since  $\dot{Q}_{\text{conduction}}$  is a function of the thermal conductivity of the neck tube, it is advisable to use low conductivity materials such as G-10 rather than stainless steels. Thermal conduction down the neck tube can be reduced by using the enthalpy of the cold evaporating gas to cool the neck wall. This contribution can be essentially reduced a factor of 5–6 by proper design. As a rule of thumb, a G-10 neck tube has a roughly linear thermal profile from cold to hot. Additionally, a vapor-cooled neck tube gives the designer a place to attach a blackbody radiation shield. Because there is no superinsulation down the neck tube, blackbody radiation from room temperature down the neck (Fig. 25) can be a significant thermal load. Most of this load can be absorbed by placing two to four vapor-cooled horizontal baffles 4–5 cm (vertically) apart.<sup>51</sup> For a liquid helium Dewar, the baffles should be positioned about where the 77 K region would be approximately one-third to one-quarter of the way up the neck tube. Any holes (e.g., for wiring, etc.) in the baffle(s) should be plugged or taped over.

The thermal head load of any cabling (e.g., SQUID leads, magnet current leads, level detector leads, etc.) leading into the cryostat must also be taken into account. Vapor cooling of the cabling can significantly decrease its thermal load.

One problem with plastic neck tubes is that—while warm—helium gas can diffuse through them and into the vacuum space. A very thin layer of aluminum or other metallic foil can be placed in the neck tube to act as a diffusion barrier; this permits thinner neck tubes. If the Dewar exhibits excessive boiloff after a period of time, it may be worthwhile to warm it up and check the vacuum. If the pressure is above 50–100 mTorr, pumping out the vacuum space is recom-

mended. Using a mass spectrometer leak detector can help determine if the pressure is due to a small helium (or nitrogen) leak or outgassing.

The use of polystyrene or polyurethane foam plugs instead of baffles is not recommended. While the initial boiloff is low, as soon as the foam is saturated by the evaporating cryogen, the thermal conductivity of the plug becomes greater than the vapor alone and the overall thermal load on the Dewar increases. A set of gold plated copper baffles *without foam baffles* may give the best results.

## 2. Tail spacing (gap)

In situations where external properties (such as magnetic fields of nearby objects, e.g., non-destructive evaluation (NDE) or biomagnetism) are to be measured, the smallest possible distance between detection coil(s) and room temperature is desirable. This distance (sometimes referred to as the tail gap) is primarily dependent on the diameter of the Dewar tail. The inner and outer tailpieces must be thick enough such that they do not deform (bow in or out) due to differential atmospheric pressure. For example, on a 25 cm diameter disk, a 1 atm differential is equivalent to a force of  $\sim\frac{1}{2}$  ton! The thickness of the tailpieces is determined by the amount of deflection (bend) that is acceptable. Typically, for a flat plate, bends of more than a tenth of a millimeter are to be avoided. The thicker the plate, the smaller the deflection. For large inside diameter (i.d.) Dewars, thicknesses become quite large.

Since most Dewar materials shrink as they get cold, the distance between the inner and outer tail sections (tail gap) will increase. For G-10, the thermal contraction from 300 to 4.2 K is  $\sim 0.3\%$ . Thus a 1 m high flat bottom Dewar [Fig. 26(a)] whose inner and outer tails are nearly touching (when warm) would have an additional 3 mm separation when the inner vessel is at liquid helium temperature. There are a number of different mechanisms to decrease the spacing.

*a. Adjustable gap mechanisms.* By placing a bellows (or similar vacuum tight mechanism) in the outer tail section [Fig. 26(b)], it is possible to reduce the coil-to-sample spacing (and eliminate the thermal contraction). The minimum achievable distance is dependent on the coil diameter and number of channels. Gaps (this includes the thicknesses of the inner and outer tail pieces) as small as 2 mm (Fig. 45) have been achieved for liquid helium Dewars with 3 mm detection coils. Gaps of  $\sim 100\ \mu\text{m}$  have been achieved for liquid nitrogen Dewars using coil-in-vacuum construction.<sup>53</sup> Care must be taken to increase the “gap” prior to warming up the Dewar, or the inner tail may push against the outer tail and damage or destroy the Dewar.

*b. Coils in vacuum.* Rather than placing the detection coil(s) in liquid, coil-in-vacuum technology connects the detection coil(s) to the cryogen bath by a thermal link [Fig. 26(c)]. This eliminates the need for an inner tail section and reduces the minimum distance between the detection coil(s) and room temperature. Typically, the thermal link is constructed from a high thermal conductivity material such as copper or sapphire. By thermally anchoring the SQUID sensor(s) to the Dewar belly, the detection coil(s) need only be

kept below their superconducting transition temperature (9.3 K in the case of NbTi). This reduces the amount of MLI (Sec. V A 1 a) and allows even closer spacing. Like liquid immersion Dewars, coil-in-vacuum cryostats can also benefit from adjustable tail mechanism. An alternate method, rather than adjusting the external tail section, is to have an adjustable mechanism at the thermal link<sup>53</sup> that allows the coils to be moved up and down. Both gear and lever mechanisms<sup>54</sup> can allow adjustments at the tens of micrometer level.

Since the probe does not need to be inserted down the neck tube, coil-in-vacuum Dewars can have significantly smaller neck tubes [Fig. 26(c)]. This reduces the heat load and allows longer hold times. The disadvantages include significantly more complex construction, ensuring that all SQUID leads are thermally anchored (rather than cooled by the cryogen vapor as in liquid immersion Dewars), and that the SQUID sensors and detection coils are part of the Dewar and cannot be removed without disassembly of the Dewar.

## B. Closed cycle refrigeration

As an alternative to the use of liquid cryogenes, closed cycle refrigeration<sup>55</sup> is desirable for several reasons. These include reduction of operating costs, use in remote locations, operation in nonvertical orientations, avoiding interruptions in cryogen deliveries, safety, and the convenience of not having to transfer every few days. Parameters governing suitability include physical size, absence of periodic replacement of cryogenic fluid, and most importantly vibration and magnetic signature. There are two main obstacles to using closed cycle refrigeration with SQUIDs. The first is the mechanical movement that (ultimately) causes the detection coils to move in the Earth’s magnetic field. The second is the magnetic signature due to the moving parts of the cryocooler’s cold head and compressor. Moving the compressor far away will reduce its relative signature. By moving the valving from the top of the cryocooler (i.e., a split head) even a meter away will reduce its signature. The remaining contributions to magnetic signature and vibration are the movement (for a GM cycle) of the heat exchanger and the stretching of the tubes generated by gas compression and expansion.<sup>56</sup> While cryocoolers<sup>56</sup> can have large cooling capacities, unless hundreds of channels are involved, only milliwatts of cooling capacity are needed to maintain SQUID sensors at their operating temperatures.

The first practical cryocooled SQUID system was the BTi CryoSQUID (Fig. 27). Based on a two stage Gifford-McMahon (GM) refrigerator, the use of a Joule-Thompson (JT) stage allowed 4 K operation with reduced vibration. An electronic comb filter was required to filter the  $\sim 1$  Hz compressor vibration from the output of the dc SQUID electronics to achieve system performance of 20 fT/ $\sqrt{\text{Hz}}$ . However, the acoustic (audible) noise from the compressor prevented its use in auditory evoked brain measurements.

Although multichannel cryocooled systems<sup>57</sup> have been built, the vibration and magnetic signature of closed cycle refrigerators kept them from widespread use. If GM refrigerators are to be used, it may be necessary to electronically subtract (Sec. IV G) out the synchronous noise (from the compressor and valve head) in order to get usable data. The

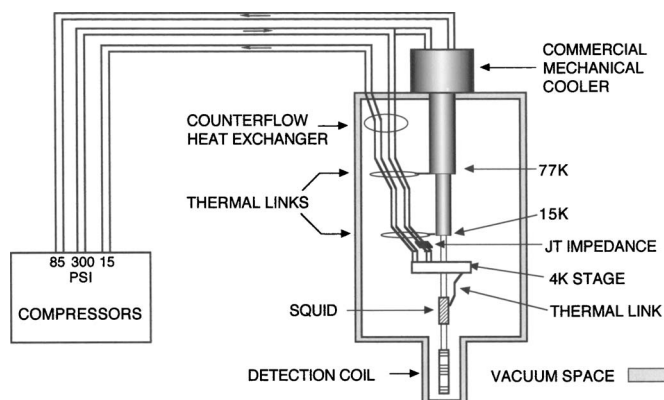


FIG. 27. CryoSQUID components (Ref. 53).

development of pulse tube refrigerators<sup>58</sup> offers promise for magnetometer operation with significantly reduced vibration (a factor of 10 better than a standard GM cycle cryocooler). Two stage pulse tube refrigerators have demonstrated 1 W cooling power at 4.2 K with a minimum achievable temperature of 2.5 K. Single stage pulse tube refrigerators have demonstrated 12 W cooling power at 77 K with a minimum achievable temperature of 40 K.

When considering the use of a closed cycle refrigeration system, both thermodynamic and operational parameters must be taken into consideration. The first consideration is usually the required operating temperature, followed by the available refrigeration capacity.

System performance is also determined by the total mass to be cooled, the total volume, and the cool down time. For systems that are used to cool sensors, mechanical vibration, electromagnetic emission, and magnetic signature must be taken into account. For split systems (where the compressor head is remote from the top of the Dewar), one must be concerned about flexible versus inflexible leads and the thermal influence of warm and cold leads to the cryogenic region.

Other considerations include reliability and operating life (mean time before failure and mean time before maintenance), cost, need for an external (water or air) cooling system for the compressor, tolerance to vibration and acceleration, and specific orientation of the cryocooler.

## VI. ENVIRONMENTAL NOISE

The greatest obstacle to SQUID measurements are external noise sources (Fig. 28). If the object being measured is within the cryostat (such as is typical in most laboratory experiments), metallic shielding can minimize external noise (e.g., act as a low pass eddy current shield). The use of gradiometer detection coils (Sec. IV F) can significantly attenuate the effect of distant noise sources. Superconducting shields essentially eliminate all external field variations, assuming that all electrical inputs to the experimental region have been appropriately filtered. Interference at power line or microprocessor clock frequencies can severely degrade performance. Unfortunately, if external objects are to be measured, superconducting shields are not appropriate.

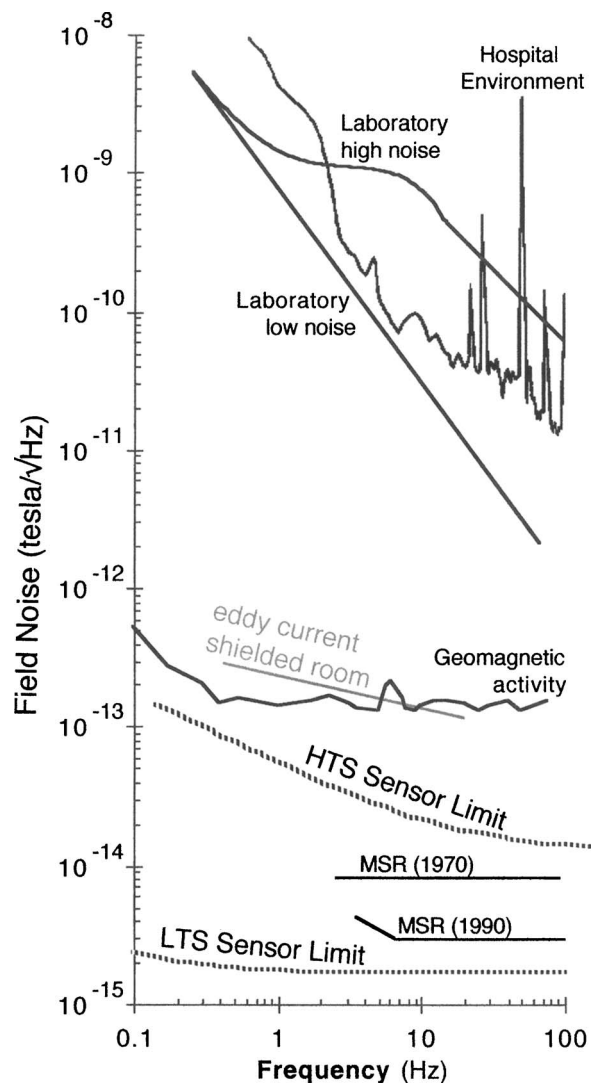


FIG. 28. rms field noise spectra in various environments as a function of frequency (after Ref. 59).

When measuring external fields, the SQUID magnetometer must operate in an environment—the magnetic field of the Earth—that can be ten orders of magnitude greater than its sensitivity (Fig. 28). The magnetic field at the surface of the Earth is generated by a number of sources. There exists a background field of  $\sim 50 \mu\text{T}$  with a daily variation of  $\pm 0.1 \mu\text{T}$ . In addition, there is a contribution (below 1 Hz) from the interaction of the solar wind with the magnetosphere. The remaining contributions to external magnetic fields are primarily manmade. These can be caused by structural steel and other localized magnetic materials such as furniture and instruments that distort the Earth's field and result in field gradients, moving vehicles that generate transient fields, electric motors, elevators, radio, television, and microwave transmitters, and the ever present power line electromagnetic field and its harmonics.

### A. Gradiometers for noise reduction

If the purpose of the measurement is to detect the magnetic field of a relatively close object, the detection coil(s) can be configured as a gradiometer (Sec. IV F) whose base

line is larger than the distance from the coil(s) to the object. This can allow rejection of external noise by more than 120 dB with less than a decibel loss of signal. It is standard practice to configure SQUID measurement systems for bio-medical and nondestructive evaluation measurements as gradiometers.

## B. Magnetic shielding

Attenuation of external magnetic fields can be accomplished by induced current shielding or flux shunting. Faraday's law ( $\nabla \times \mathbf{E} = -\partial \mathbf{B} / \partial t$ ) states that an electric field is induced in a material when it is exposed to a time dependent magnetic field. If the material is conducting ( $\rho \ll \infty$ ), the electric field induces a current that generates a magnetic flux to oppose the externally applied field. This effect, which is frequency dependent, can be used to create an eddy current shield to attenuate electromagnetic interference. The behaviors of the magnetic field and magnetic flux density are governed by Ampere's law that requires that  $H_{\text{tangential}}$  be continuous and by Gauss' law that requires that  $B_{\text{normal}}$  also be continuous at the interface between materials of differing magnetic permeability. The effect for materials with high magnetic permeabilities ( $\mu \gg 1$ ) is that magnetic flux is "pulled" towards a shielding material, "shunted" within the material, and then "released" back into the air (or vacuum), on the external surface of the shielding material.<sup>60</sup> Flux shunting is effective even at dc. The amount of flux shunting is dependent on  $\mu$ . The Meissner effect (Sec. I C) can also be used to make superconducting shields that shield external fields independent of frequency. These effects can be used individually or in combination to significantly reduce the effects of environmental noise.

### 1. Induced current shielding

One method to attenuate external noise sources is with an eddy current shield that generates fields that act to cancel the externally applied fields within the conducting material. The shielding effect is determined by the skin depth  $\lambda$ , the distance where the field is attenuated by a factor  $1/e$ . For a sinusoidal varying wave,

$$\lambda = \sqrt{\rho / \pi \mu_0 f}, \quad (12)$$

where  $f$  is the frequency of the applied field,  $\rho$  is the electrical resistivity, and  $\mu_0$  is the magnetic permeability of free space. In situations where the wall thickness  $t \ll \lambda$ , external fields are attenuated by

$$\left( \frac{H_{\text{internal}}}{H_{\text{external}}} \right)^2 = \frac{1}{1 + (2\pi f L / R)^2}, \quad (13)$$

where  $L$  is the inductance of the enclosure (assumed in this case to be an open-ended cylinder) and  $R$  is the resistance along the path of current flow. Unfortunately, induced currents in the shield generate noise. For an open-ended right circular cylindrical shape at a temperature  $T$ , the field noise internal to the can is given (within a factor of 2) by

$$B_{\text{rms}} = \sqrt{\frac{32\pi k_B T t}{\ell d \rho \times 10^{12}}}, \quad (14)$$

where  $\ell$  is the length and  $d$  the diameter of the can in mks units. The cutoff frequency is given by  $f_{-3 \text{ dB}} \approx \rho / 4\pi t d \times 10^5$  (again in mks units). Because of noise considerations, eddy current shields that are to be placed near the detection coils should be made from relatively poor conductors such as BeCu. Typical cutoff frequencies using these techniques range from tens of hertz to tens of kilohertz.

Another approach is to use eddy current shielding to shield the entire measurement system. An eddy current room ( $2.4 \times 2.5 \times 3.6 \text{ m}^3$ ) was constructed with 2 cm thick high purity aluminum walls. It achieved shielding  $>40$  dB at 60 Hz with improved performance at higher frequencies, and an equivalent field noise was less than 200 fT/ $\sqrt{\text{Hz}}$  at frequencies above 1 Hz.<sup>61</sup>

In the situation where  $t \gg \lambda$ , the attenuation becomes  $(r/\lambda)e^{t/\lambda}$ . If pure eddy current shielding is used, this would require extremely thick walls.

### 2. Flux shunting

The need for shielding at lower frequencies down to dc has led to the use of high permeability materials for shunting magnetic fields external to the experimental region. For a ferromagnetic material, the permeability of the material [ $\mu = \mu_0(1 + \chi)$ ] replaces  $\mu_0$  (the permeability of free space =  $4\pi \times 10^{-7} \text{ H/m}$ ) in Eq. (12). The shielding is due to the fact that flux prefers the path with the highest permeability. Since magnetically "soft" materials (e.g., mu-metal) can have permeabilities that exceed  $10^4$ , the external magnetic flux is shunted through the mu-metal walls, reducing the magnetic flux intensity ( $\mathbf{H}$ ) inside the shield.

For biomagnetic measurements (Sec. X), it may be necessary to enclose not only the sensing device, but also the subject in a magnetically shielded room (MSR) with large interior dimensions (e.g.,  $4 \times 3 \times 2 \text{ m}^3$ ). The first MSR used for SQUID measurements was built at the MIT Magnet Laboratory<sup>63</sup> and had an octagonal shape. This room was used for the first magnetocardiogram<sup>63</sup> (Sec. X D) and magnetoencephalogram<sup>64</sup> (Sec. X C) recordings. The use of multiple shields can act to further shield the interior of a MSR (Fig. 30). For the eight layer Berlin MSR,<sup>65</sup> shielding factors exceeded 100 dB at frequencies above 0.01 Hz. Active shielding (Sec. VI B 4) improved that to  $>130$  dB. All commercial MSRs combine multiple mu-metal for low frequency and aluminum walls for high frequency shielding (Fig. 29). Reference 66 gives a good overview of MSR design.

The ideal shield would be a superconducting shield because of its ability to provide complete shielding down to dc. However, a completely enclosed (e.g., six sided) superconducting MSR is unrealistic. The use of HTS superconductors such as  $\text{Bi}_2\text{Sr}_2\text{Ca}_2\text{Cu}_2\text{O}_{10}$  has allowed the construction of cylindrical shields<sup>32</sup> with low frequency attenuation that approaches that of the Berlin six layer MSR (Fig. 30).

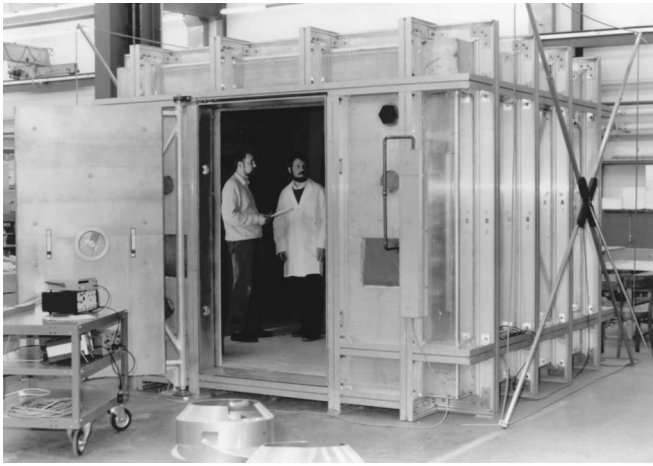


FIG. 29. Commercial magnetically shielded room showing first layer of mu-metal shielding and rigid aluminum frame.

### 3. Shielding factors

The attenuation of the transverse magnetic field at dc (ignoring end effects) for a single layer closed cylindrical shield where  $\mu \gg 1$  is given<sup>67</sup> by  $A \approx \mu t/d$ , where  $t$  is the wall thickness and  $d$  is the outer diameter of the shield. The use of multiple layer shields with gaps between the shields can further improve shielding (and provide low field environments). For a two layer shield,  $A \approx A_{\text{inner}} + A_{\text{outer}} + A_{\text{inner}}A_{\text{outer}} [1 - (d_{\text{inner}}/d_{\text{outer}})^2]$ . For particularly noisy backgrounds or experiments where subpicotesla environments are needed, three or four layer shields may be necessary.

In many situations, it is not possible to completely enclose the detection coils. An open-ended tube of high permeability or superconducting material can still provide significant attenuation of external fields. Table II gives the attenuation for both axial and transverse fields for semi-infinite tubes ( $\mu = \infty$  for normal metals;  $\mu = -1/4\pi$  for superconductors).

If the shield has a finite length ( $h$ ) and the measurement point is at the midpoint of the tube ( $h/2$ ), the shielding factor would be half that of a single semi-infinite tube. For example, taking the dimensions of the cylindrical shield described in Ref. 32 [ $d=65$  cm and  $z$  (half the length of the tube)  $=80$  cm] gives a theoretical attenuation of  $H_{\text{axial}}/H_{\text{external}} = \frac{1}{2}e^{-7.664 \cdot 80/65} = -88$  dB. This can be compared to the measured values of 77 dB (open circles in Fig. 30).

For positions above (or below the halfway point), the attenuation can be modeled as the “sum” of two semi-infinite tubes, one at depth  $z$  and the other at  $z+h/2$ . It can be seen that the axial shielding factor of a superconducting tube is superior to that of a mu-metal tube, whereas the transverse shielding factor of a mu-metal tube is greater than the transverse shielding factor of a superconducting tube. This implies that a combination of superconducting and mu-metal shields may serve to better screen both transverse and axial noise field components than either shield alone.

### 4. Active shielding

MSR shielding factors up to 120 dB ( $10^6$ ) or higher can be achieved by the use of active shielding.<sup>69</sup> In this situation, external coils surround the exterior of the MSR. A low noise

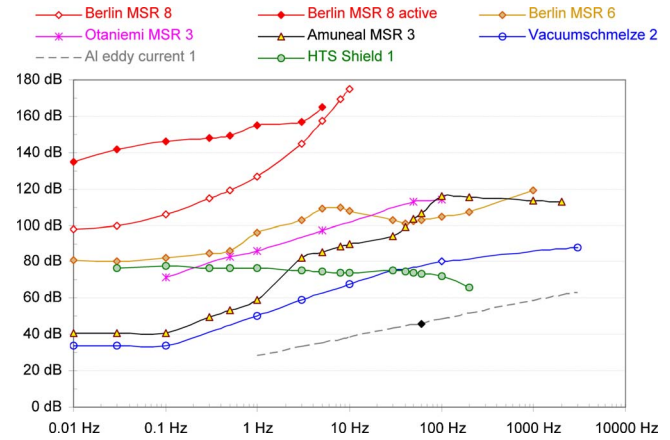


FIG. 30. (Color online) Shielding factors for various shielded rooms. The trailing number refers to the number of mu-metal layers. The dashed line is the shielding factor for an aluminum eddy current room (Ref. 62).

magnetometer (SQUID or flux gate) is mounted at the interior of the MSR. Its output is used (in a negative feedback mode) to generate a current that is fed into the external coils to cancel the low frequency noise (drift) detected by the magnetometer. By using coils (and detectors) in all three dimensions, 30–40+ dB of additional noise reduction can be achieved at low frequencies.

The use of external field coils can allow significant reduction in external noise even without a MSR. Nearly 70 dB attenuation at 60 Hz can be achieved by using a reference magnetometer and appropriate negative feedback electronics to drive a large (2.4 m) set of Helmholtz coils. It is important to use a reference sensor with the same characteristics as the detection coil(s). If the reference sensor has a significantly higher noise level, it will not be possible to achieve sensor noise limited sensitivities.

### C. Electrical noise

SQUID magnetometers and gradiometers are highly sensitive to external magnetic noise and radio frequency interference (rfi). Changes in power line and rfi intensities can cause the optimum tuning parameters to change. By monitoring the triangle height (Fig. 12) of the SQUID electronics in the tune mode, it may be possible to observe the effect of external noise sources. If working with a SQUID specifically designed to measure external fields, it is advisable to perform initial tests in a magnetically shielded environment. If you do not have access to a shielded room, measurements made after midnight or on the weekend can be compared to measurements during the day to see if there are environmental effects. In particularly bad environments, if rfi is of concern, wrapping the Dewar in aluminum foil may improve the situation. This acts as an eddy current shield. While it may reduce the system’s bandwidth (depending on the amount of aluminum foil used) and perhaps increase the system’s white noise, it can be very effective in attenuating rfi.

During the initial testing, be sure that the system is on a sturdy platform. A flimsy table may cause motion-induced noise. Also, be sure that the platform (or whatever mounting is being used) is free of any ferromagnetic contaminants. Avoid using conductive metal tables as they can couple in

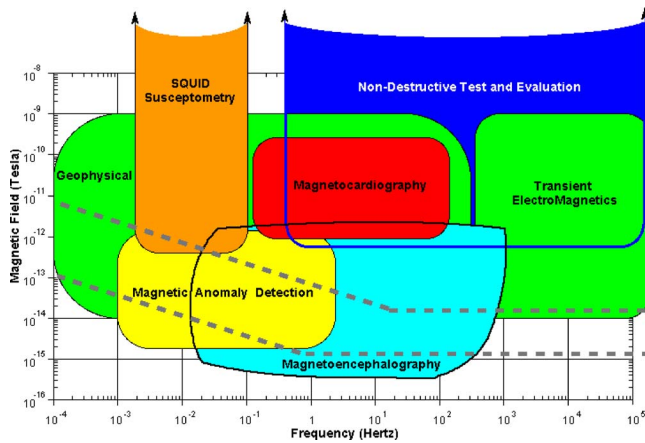


FIG. 31. (Color online) Field sensitivities and bandwidths typical of various applications. The dashed lines indicate the sensitivity of commercially available SQUIDs [lower line LTS, Fig. 14(d); upper line HTS, Fig. 14(e)].

gradient noise.  $XY$  stages can induce both magnetic noise (from the materials used to build the stage, especially if in motion) and electrical noise (from linear motors or piezoelectric drives used to move the stage). Superconducting motors<sup>70</sup> have been used to fabricate magnetically quiet  $XY$  stages.

The instrumentation being used can be a source of noise. Another source of rfi is microprocessor clock frequencies. The leads going from the SQUID sensor(s) to the electronics have to be electrically isolated from any other circuitry. Optoisolation (fiber-optic coupling) can isolate the microprocessor from the experiment. One test to see if there are potential noise problems is to run a hair dryer near the measurement circuit. The carbon brushes will generate large amounts of rfi noise and can help to diagnose potential problems during construction.

Common grounds are to be avoided like the plague—the introduction of power line frequencies can overwhelm almost any measurement. The leads should be twisted (noninductively wound) pairs. If rfi pickup is of concern, the leads should be shielded in metal tubing or metallic braid shielding. PbSn tubing between the detection coil and SQUID sensor is preferred because it acts as a superconducting shield below 6 K. If using PbSn tubing, be sure that the leads cannot move inside the tubing. Well-twisted leads that are properly anchored are better than leads that may move around inside of a superconducting shield tube. Measurements made after midnight or on the weekend can be compared to measurements during the day to see if there are environmental effects.

## VII. LABORATORY APPLICATIONS

SQUIDs offer the ability to measure at sensitivities unachievable by other magnetic sensing methodologies.<sup>1</sup> However, their sensitivity requires proper attention to cryogenics and environmental noise. SQUIDs should only be used when no other sensor is adequate for the task.<sup>71</sup> This applies not just to laboratory applications, but to every potential use of

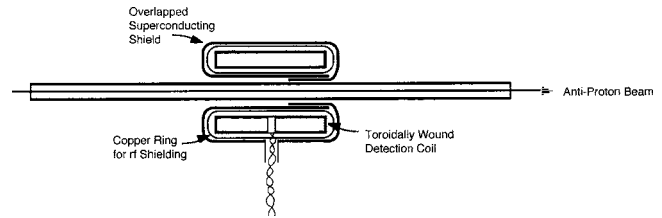


FIG. 32. Beam current meter.

SQUID sensors. A large number of applications configure the SQUID as a magnetometer. Sections VIII–X discuss a number of specific uses.

There are many exotic uses for SQUID sensors (Fig. 31). Figure 32 shows how a toroidally wound coil can be used to detect charged particles (in this case antiprotons) in a particle accelerator.<sup>72</sup> Planar gradiometers [Fig. 19(c)] have been successfully used as a detection coil to monitor cyclotron beam currents.<sup>73</sup>

SQUIDs can also be configured to measure a wide variety of electromagnetic properties (Fig. 33). As mentioned in Sec. II A, there is no method for making true superconducting connections to SQUIDs with HTS wire. As a result, commercially available HTS devices are currently in the form of magnetic sensing [Fig. 33(b)] rather than current sensing devices [Figs. 33(a)–33(c)]. Table II shows typical capabilities of SQUID-based instruments. The number in the parentheses refers to the corresponding figure. Additional information on laboratory applications of SQUID systems can be found in Refs. 36 and 74–76.

If there is no fundamental reason that requires dc measurements, ac measurements may provide higher signal-to-noise ratio. Increasing the effective measurement frequency and using a lock-in amplifier to reject out-of-band noise can significantly improve signal-to-noise ratio. This can be helpful in situations where  $1/f$  noise or external noise sources (Fig. 28) are significant.

### A. dc measurements

One common use of a SQUID is as an ammeter. Measurements down to dc can be made by directly coupling the current into the input circuit of the SQUID sensor in the case of LTS SQUIDs and inductively coupling (via superconducting transformers) into HTS SQUID sensors. When coupling into a circuit that is at room temperature,<sup>77</sup> significant low pass filtering of the input current must be done to prevent rfi interference. A toroidal geometry for the input coil has the advantage of extremely good coupling to the source while having excellent immunity to external sources. Such a configuration has been used to construct an antiproton beam current meter.<sup>72</sup>

There are also a number of applications where the input circuits can be resistive. One example is the detection of extremely small voltage or resistance. Figure 33(c) shows the schematic of a SQUID picovolt measuring system. When a voltage  $V_{\text{input}}$  is applied across the input terminals, a current is generated in the SQUID input coil. In this situation, the feedback current ( $I_{\text{FB}}$ ) that would normally be applied to the SQUID loop via the feedback coil (see Fig. 13) is fed back

via  $R_{FB}$  through  $r_{std}$  until the voltage drop across  $r_{std}$  is equal to  $V_{input}$  and there is no net current through the SQUID. The output voltage ( $V_{output}$ ) measures the voltage drop across  $R_{FB}$  and  $r_{std}$  with  $V_{input} = V_{output} \times r_{std} / (R_{FB} + r_{std})$ .

The voltage gain of the system is determined by the ratio of  $R_{FB}/r_{std}$ . Typical values for  $R_{FB}$  and  $r_{std}$  are  $3 \text{ k}\Omega$  and  $30 \text{ }\mu\Omega$ , respectively, giving a voltage gain of  $10^8$ . The standard resistor  $r_{std}$  is typically at 4.2 K. The voltage source, however, may be at a completely different temperature.

With the addition of an appropriate current source, it is possible to measure resistance [Fig. 33(d)]. Replacing  $V_{input}$  with a resistor ( $R_X$ ) and a highly stable constant current source ( $I_{CCS}$ ) (Ref. 78) creates a voltage drop across the resistor. The resistance is determined by  $R_X = V_{output} \times r_{std} / [(R_{FB} + r_{std}) I_{CCS}]$ .

The input noise ( $\sim 10^{-14} \text{ V}$ ) of a SQUID picovoltmeter is a function of the source resistance and temperature, the voltage noise due to the standard resistor, and the inherent current noise of the SQUID ( $I_N$ ). The system noise (in  $V/\sqrt{\text{Hz}}$ , referred to the input) is given by

$$V_{\text{rms}} = \sqrt{4k_B T_{\text{source}} R_{\text{source}} + 4k_B T_{r_{\text{std}}} r_{\text{std}} + I_N^2 R_{\text{source}}^2}. \quad (15)$$

Measurement of the Johnson noise in a resistor ( $\langle V^2 \rangle = 4k_B TR \Delta f$ , where  $\Delta f$  is the bandwidth of the measurement) can be used to determine absolute temperature.<sup>13</sup> Commercially available LTS SQUIDS have equivalent device temperatures  $< 1 \text{ }\mu\text{K}$  and are suitable for noise thermometry.<sup>13</sup> Resolutions of  $10^{-11} \text{ }\Omega$  can be achieved for  $R_X < 10^{-2} \text{ }\Omega$ . Other applications of picovoltmeters include measurements of thermopower, thermal emfs (thermocouples), and infrared bolometers.

## B. ac measurements

Directly connecting a current source to the input of a SQUID sensor [Fig. 33(a)] can give current sensitivities at

TABLE II. Relative attenuation along the axis of ideal semi-infinite cylinder (Ref. 68).  $z$  is the distance measured from the open end of the can and  $d$  is the diameter of the can.

	$H_{\text{axial}}$	$H_{\text{transverse}}$
Superconducting ( $\mu = -1/4\pi$ ) tube	$e^{-7.664z/d}$	$e^{-3.68z/d}$
Mu-metal ( $\mu = \infty$ ) tube	$e^{-4.81z/d}$	$e^{-7.664z/d}$

the  $10^{-12} \text{ A}/\sqrt{\text{Hz}}$  level. By using a step-up transformer,<sup>79</sup> ac sensitivities better than  $10^{-15} \text{ A}$  in a 1 Hz bandwidth can be achieved.

The SQUID can also be used as the null detector in an ac bridge circuit [Fig. 33(e)] to measure both resistive and reactive components of a complex impedance. The unknown impedance  $Z$  is excited by a current generated by an oscillator voltage that is attenuated by a precision ratio transformer ( $\lambda$ ). The difference between the voltage developed across the unknown impedance  $Z$  and that developed in the secondary of a nulling mutual inductor  $m$  is applied to the input of the SQUID circuit. The primary current in  $m$  is proportional to the oscillator voltage and defined by the setting of the ratio transformer ( $\alpha$ ). An additional reactive current is supplied by a second ratio transformer ( $\beta$ ) that causes the primary current to be passed through a capacitor rather than a resistor, thus generating a  $90^\circ$  phase shift in the voltage applied to  $m$ . The amplified off-balance signal that appears at the output of the SQUID control electronics can be displayed by means of a lock-in amplifier tuned to the oscillator frequency. As mentioned earlier, the sensitivity is limited inherently by the Johnson noise in the resistive components of the unknown (including the potential connections) and by the device noise of the SQUID sensor. Assuming  $I_N \approx 1 \text{ pA}/\sqrt{\text{Hz}}$ , such a system is capable of measuring self- and mutual inductances between  $10^{-12}$  and  $10^{-3} \text{ H}$  with  $1:10^6$  part resolution.<sup>13,75</sup>

Figure 34(a) shows a typical experimental setup for the

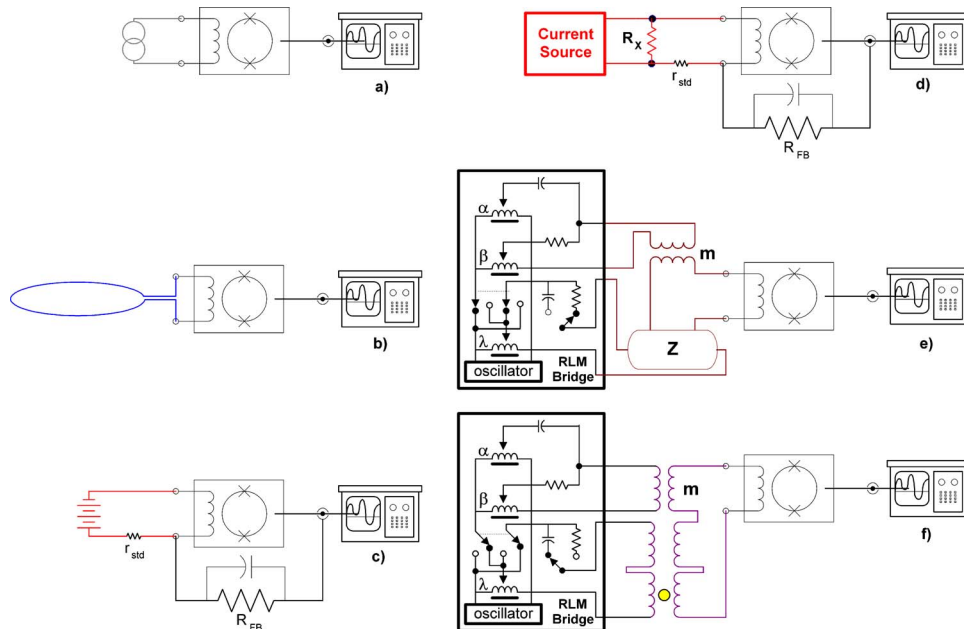


FIG. 33. (Color online) (a) ac and dc current, (b) magnetic field, (c) dc voltage, (d) dc resistance, (e) ac resistance/inductance bridge, and (f) ac mutual inductance (susceptibility bridge).

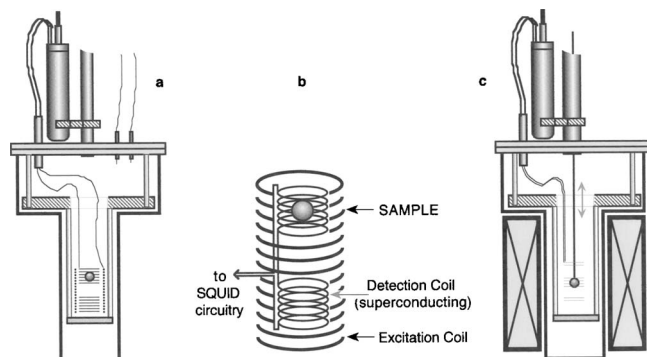


FIG. 34. Magnetic susceptibility measurement apparatus (liquid helium Dewar not shown): (a) ac susceptibility; (b) signal and excitation coil details; (c) second derivative oscillating magnetometer for dc measurements with external dc field coils.

measurement [Fig. 33(f)] of ac susceptibility. Such a configuration can be used for thermometry by measuring the low (millitesla) field magnetic susceptibility of paramagnetic salts such as  $\text{Ce}_2\text{Mg}_3(\text{NO}_3)_{12} \cdot 24\text{H}_2\text{O}$ —usually referred to as CMN.<sup>76</sup>

It is important not to couple the excitation signal into the detection circuit. The excitation and detection coil should not have the same gradient order. Otherwise, the excitation signal will be applied to the detection coil. For example, using a solenoidal excitation coil (gradient order=0) with a first derivative detection coil [Figure 34(b)] minimizes the current flowing through the detection coils. Likewise, a first order gradient excitation coil will couple no current through a second order detection coil (assuming they have a common center). Since gradiometer coils cannot be perfectly wound, the use of external feedback (Sec. IV B) may be needed to further reduce the contribution of the excitation coil into the SQUID detection circuit.

### C. Variable temperature SQUID magnetometer/susceptometers

Instead of using a secondary ac excitation coil [Figs. 33(f) and 34(b)], a dc field can be used to magnetize samples. Typically, the field is fixed and the sample is moved into the detection coil's region of sensitivity [Fig. 34(c)]. The change in detected magnetization is directly proportional to the magnetic moment of the sample.

Commonly referred to as SQUID magnetometers, these systems are properly called SQUID susceptometers. They have a homogeneous superconducting magnet to create a very uniform field over the entire sample measuring region and the superconducting pickup loops. The magnet induces a moment allowing a measurement of magnetic susceptibility. The superconducting detection loop array is rigidly mounted in the center of the magnet. This array is configured as a gradient coil to reject external noise sources. The detection coil geometry determines what mathematical algorithm is used to calculate the net magnetization. Oppositely paired Helmholtz coils<sup>80</sup> (Fig. 35), transverse detection coils, first and second derivative gradiometers [Figs. 19(b), 19(d), and 34(c)] have all been successfully used.

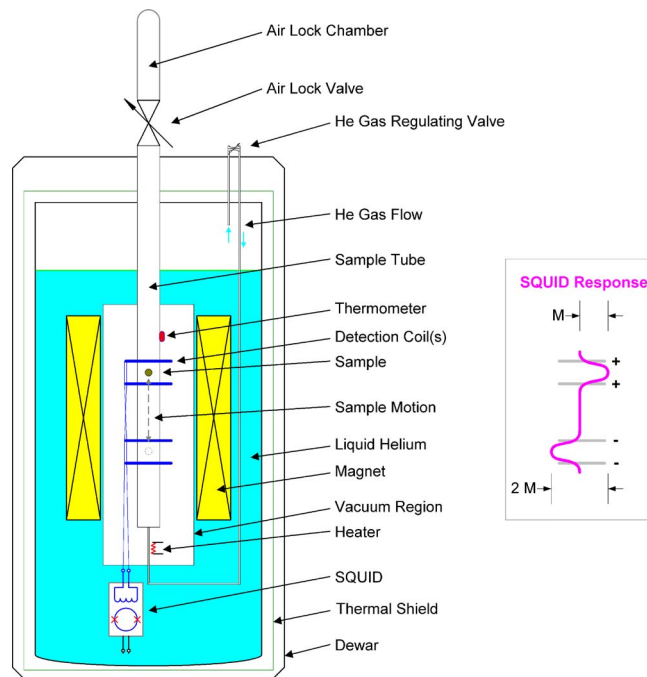


FIG. 35. (Color online) Variable temperature susceptometer (various electrical leads omitted for clarity). The trace on the right shows the response of the detection coil(s) as a function of sample position height.

Figure 35 shows input circuitry consisting of a superconducting circuit having two opposed Helmholtz detection coils and the SQUID input coil connected in series. The current that flows in response to a change in flux is given by  $\Delta I = \Delta\Phi/L$ , where  $\Delta I$  is the current induced in the circuit by the flux change  $\Delta\Phi$ , and  $L$  is the circuit's inductance. This is analogous to the response of conventional (resistive) detection coils (such as those used in a vibrating sample magnetometer),

$$\frac{dI}{dt} = \frac{d\Phi}{dt} \frac{1}{L} = -\frac{V}{L}, \quad (16)$$

where  $V$  is the voltage induced across the coils. The important difference is that for the superconducting case, the induced current is independent of the *rate* of flux change. This provides uniform response at all frequencies (i.e., true dc response) and allows the sample to be moved arbitrarily slowly without degrading performance. In this particular example, the sample is moved between the two counterwound detection coils. As the sample passes through a coil, it changes the flux in that coil by an amount proportional to the magnetic moment ( $M$ ) of the sample. The peak-to-peak signal from a complete cycle is thus proportional to twice  $M$ . The SQUID sensor (shielded inside a niobium can) is located where the fringe fields generated by the magnet are less than 10 mT. The detection coil circuitry is typically constructed using NbTi. This allows measurements in applied fields of 9 T while maintaining sensitivities of  $10^{-8}$  emu. Thermal insulation (not shown in Fig. 35) is placed between the detection coils and the sample tube to allow the sample temperature to be varied.

While persistent mode superconducting magnets are extremely stable, field drift at the 1 ppm/h level into a magne-

tometer input coil can be at the nT/s level. Again, the use of gradiometer detection coils can reduce this by two to three orders of magnitude. The susceptometer shown in Fig. 35 had a NbTi shield surrounding the detection coil. When the field was changed, the NbTi shield was heated above  $T_c$ , and then cooled when the desired field strength was reached. The NbTi shield trapped the field supplied by the superconducting magnet and gave the system much greater field stability than if no shield was present. The disadvantage of this method was the time needed to change fields (due to the heating and cooling of the NbTi shield) and its inability to do swept field measurements.

The most popular detection coil configuration is that of a second order coil configuration.<sup>81</sup> In this situation, the detected output is compared with that of an ideal response to determine the magnetization. This technique has the advantage of eliminating noise. Additionally, the intentional choice not to use a NbTi shield allowed swept field scans to be performed. Coupling two axial channels of differing gradient order (e.g., first and second) can significantly improve noise rejection. The detection coil does not necessarily need to be in an axial configuration. Planar gradiometers have been used to detect the onset of superconductivity in diamond pressure cells.<sup>82</sup> Placement of secondary excitation coils can allow ac susceptibility measurements approaching  $10^{-8}$  emu to be made in the presence of a significant dc bias field.

The use of a variable temperature insert can allow measurements to be made over a wide range (1.8–400 K). Typically, the sample temperature is controlled by helium gas flowing slowly past the sample (Fig. 35). The temperature of this gas is regulated using a heater located below the sample measuring region and a thermometer located above the sample region. This arrangement ensures that the entire region has reached thermal equilibrium prior to data acquisition. The helium gas is obtained from normal evaporation in the Dewar, and its flow rate is controlled by a precision regulating valve. The use of an oven probe can raise the sample temperature to 800+ K (at the expense of smaller sample measurement volume). If the system is to have top loading access, then the central (sample) tube should be constructed from a low conductivity material (e.g., 300 series SS) rather than high conductivity materials such as Al or Cu [Eq. (14)]. BeCu is an alternative choice if time constants faster than 10 ms are needed. Rock magnetometers (Sec. VIII C) use sample tubes made from fiber glass/epoxy rather than stainless steel primarily because metallic tubes conduct rfi into the pickup coil region and can cause SQUID noise. This also allows for time constants that approach microseconds. A disadvantage of insulating sample tubes is their very long thermal time constants.

When measuring changes in magnetic moment resulting from a variable other than temperature or magnetic field (e.g., an applied acoustic or rf pulse), the sample is centered in one of the paired detection coils (Fig. 35) and the SQUID output monitored as a function of the stimulus. This technique is useful for studying flow/stop-flow reactions, gas adsorption, catalytic processes, optical dissociation, or similar time dependent phenomena. Reference 83 gives a good over-

view of variable temperature SQUID susceptometer measurements.

A SQUID can also be used as an amplifier in a vibrating sample magnetometer (VSM). The VSM<sup>84</sup> moves the sample through a coil at a fixed frequency. Conventional VSMs use resistive coils and conventional amplifiers to get sensitivities at the  $10^{-5}$  emu level. The use of a SQUID can allow sensitivities at the  $5 \times 10^{-9}$  emu/ $\sqrt{\text{Hz}}$  level.<sup>85</sup>

#### D. NMR

NMR signals<sup>86</sup> can be measured by placing a sample (e.g., protons or  $^{19}\text{F}$ ) in the center of SQUID detection coils and either sweeping the external field or applying a rf excitation to the sample. The same experimental concept can be used to measure electron paramagnetic resonance (EPR) signals. Although limited to 100 ppm field uniformities, SQUID susceptometers (e.g., SHE VTS (Fig. 35), Quantum Design MPMS [Fig. 34(c)], or Conductus  $\chi\text{MAG}$ ) are excellent platforms for basic demonstrations of NMR measurements.

The relationship between the resonant frequency and applied magnetic field is given by the gyromagnetic ratio  $\gamma$  (for protons,  $\gamma=42.6$  MHz/T). For some materials,  $\gamma$  is so small (e.g.,  $^{39}\text{K}$  where  $\gamma=1.99$  MHz/T) that a detection frequency of 383 MHz (equivalent to 9 T for protons) would require an applied field of 193 T. The bandwidth of commercially available SQUID electronics (<100 kHz) places limits on NMR detection. However, custom made SQUID electronics<sup>24</sup> can allow measurements to be made at megahertz frequencies. The use of SQUID detection coils can offer significant improvements over conventional coils at a given field strength or allow equivalent signal-to-noise ratio at lower applied fields (reducing magnet cost). Similarly, SQUIDs offer improved signal-to-noise ratio for measurements of nuclear quadrupole moments.<sup>87</sup>

#### E. Other measurement techniques

Because SQUID magnetometers are vector devices, they can detect rotational movement of a magnetometer coil in the Earth's magnetic field ( $\sim 50 \mu\text{T}$ ) as small as  $10^{-3}$  arc sec. SQUIDs have been used for more esoteric applications including temperature measurements with resolution near  $10^{-12}\text{K}$  (Ref. 88) and to measure position for gravity wave detectors with sub angstrom resolution.<sup>89</sup> SQUIDs are also used as ultrahigh resolution angular position detectors in the Gravity Probe B program, which aims to test several predictions of Einstein's general theory of relativity.<sup>90</sup> Four SQUIDs in an Earth-orbiting satellite measure deviations in gyroscope spin axis direction with nanoradian resolution.

TABLE III. Typical sensitivities of SQUID instruments.

Measurement	Sensitivity
Current [Fig. 33(a)]	$10^{-12}$ A/ $\sqrt{\text{Hz}}$
Magnetic fields [Fig. 33(b)]	$10^{-15}$ T/ $\sqrt{\text{Hz}}$
dc voltage [Fig. 33(c)]	$10^{-14}$ V/ $\sqrt{\text{Hz}}$
dc resistance [Fig. 33(d)]	$10^{-12}$ $\Omega$
Mutual/self-inductance [Fig. 33(e)]	$10^{-12}$ H
Magnetic moment [Fig. 33(f)]	$10^{-10}$ emu

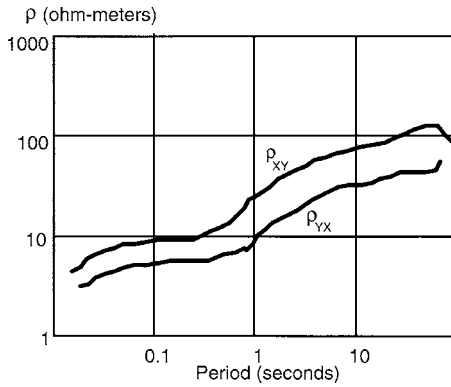


FIG. 36. Calculated resistivity as a function of frequency.

SQUIDS have been used in searches for dark matter such as weak interacting massive particles<sup>91</sup> (WIMPs) and axions<sup>92</sup> along with attempts at detecting magnetic monopoles<sup>93</sup> and free quarks.<sup>94</sup>

While this review is focused on low frequency applications, there is a need for higher frequency SQUID instruments. In particular, applications such as axion detectors, radio astronomy, and NMR (Sec. VII D) are examples where SQUIDS offer superior sensitivity at frequencies that can approach 1 GHz.<sup>95</sup>

**F. Absolute field measurements**

**1. Flip-coil magnetometers**

As mentioned in Sec. III E, conventional SQUIDS are sensitive to *relative* changes only. It is possible to make a SQUID magnetometer into an absolute magnetometer by rotating a coil 180° such that the field change (maximum to minimum) is twice the maximum field normal to the axis of rotation. To determine the total field, this needs to be done in all three axes. Such “flip-coil” magnetometers have been constructed. One example used a centimeter diameter coil that was rotated using plastic bevel gears actuated from room temperature to achieve field resolution at the picotesla level. In the case of “large” (i.e., microtesla total fields if picotesla resolution is desired) fields, caution must be taken not to exceed the dynamic range of the electronics. If the speed of rotation is slow enough to allow for flux counting (adding the number of resets of the electronics), the dynamic range of the measurement can be extended by orders of magnitude.

**2. Superconducting quantum interference filters**

An array of different superconducting loop sizes, either in series or in parallel configuration, acting as grating struc-

tures, can be used to form a superconducting quantum interference filter (SQIF). This type of interferometer is based on a phase dependent superposition of currents flowing through a multiloop network of Josephson junctions. The basic effect of such an arrangement is that the contributions of the loops to the output signal mutually cancel each other for any finite value of the ambient magnetic field. For zero magnetic field, a mutual enhancement occurs by means of the coherent superposition. Therefore, the  $V-\Phi$  characteristic of a SQIF shows a unique dip at zero field. The device can be tailored to show a dip with high swing and steep side slopes. In contrast to SQUIDS the characteristic field dependence of the voltage output of a SQIF is nonperiodic.<sup>96</sup>

The sensitivity of a SQIF scales proportionally to the square root of the number of loops in the array.<sup>97</sup> With even a moderate number of loops, this can allow absolute field measurements to be made at sensitivities approaching a few  $fT/\sqrt{Hz}$ . Another advantage of SQIFs is that the Josephson junction parameters need not be well matched, making fabrication of SQIF devices from HTS materials significantly easier than arrays of SQUIDS such as would be used in Josephson voltage standards.

**VIII. GEOPHYSICAL APPLICATIONS**

SQUID magnetometers are used to measure the Earth’s magnetic field (Fig. 28) at frequencies ranging between 1 kHz and  $10^{-4}$  Hz. Geophysical detection can be classified according to the type of energy source used by the method—seismic (acoustic energy), electromagnetic (natural and man-made), electrical (natural and manmade), magnetic (Earth’s magnetic field), gravity (Earth’s gravitational field), and radiometric (generally gamma ray) emissions from subsurface materials. Measurements made by electrical and electromagnetic methods are primarily sensitive to the resistivity of the subsurface materials at frequencies below 100 kHz. Above 100 kHz, the methods are sensitive to both resistivity and the dielectric constant of the subsurface materials.

In comparison to large induction coils, SQUID magnetometers are easier to deploy and use (allowing SQUID sensors to be placed down boreholes), operate to dc (with flat phase response), and avoid giving undue emphasis to high frequency phenomena such as the ubiquitous lightning induced sferics. Their wide bandwidth allows the use of a single instrument as compared to induction coils where multiple coils may be required. The high dynamic range of SQUIDS can allow diurnal range variations ( $\pm 100$  nT) to be tracked while still maintaining full sensitivity.

depth	Resistivity in ohm-meters					
	40			25		
200 m	6.0			4.0		
800 m	300	600	700	800	1000	500 100
10 km	500	800	700	800	1000	500 200
15 km	50	30	20	20	10	7 5
25 km	70	30	30		20	

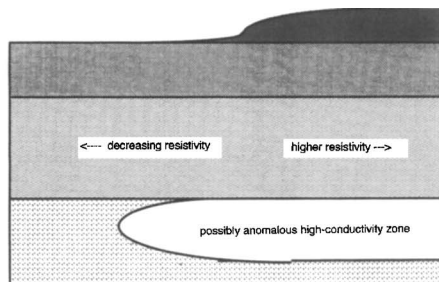


FIG. 37. Calculated 2D inversion map and resultant geologic interpretation. Horizontal span  $\approx 20$  km. After Ref. 100.

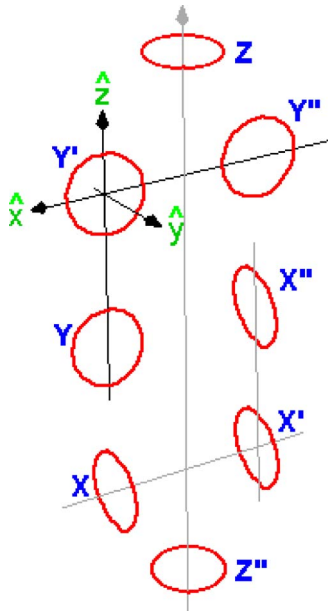


FIG. 38. (Color online) Tensor made from discrete magnetometers.

The use of SQUIDs in electromagnetic prospecting methods can be divided into passive and active methods.

**A. Passive methods**

Passive methods such as magnetotellurics (MT) and audio MT (AMT) use the interaction of the solar wind in the ionosphere as an electric and magnetic field generator. In general, they cover the frequency range of megahertz to 10 Hz and 10 Hz to 1 kHz, respectively.

**1. Magnetotellurics (MT)**

Magnetotellurics can be used to determine the electrical conductivity distribution of the Earth’s crust by measuring the Earth’s electric and magnetic fields.<sup>98</sup> Because the Earth is a good electrical conductor compared to the air, the electrical field generated in the ionosphere (due to the solar wind) is reflected at the Earth’s surface, with components of both the electric and magnetic field decaying as they penetrate into the Earth. The electric field (as a function of frequency) is related to the magnetic field via an impedance tensor ( $\mathbf{Z}$  in units of mV/km nT) where

$$E(\omega) = \mathbf{Z}H(\omega),$$

$$E_x(\omega) = Z_{xx}H_x(\omega) + Z_{xy}H_y(\omega),$$

$$E_y(\omega) = Z_{yx}H_x(\omega) + Z_{yy}H_y(\omega),$$

$$\rho_{ij} \approx 0.2|Z_{ij}|^2\tau; \delta \approx 0.5\sqrt{\rho\tau}. \tag{17}$$

By measuring  $E$  and  $H$ , the electrical resistivity of the Earth ( $\rho$  in  $\Omega$  m) can be calculated (Fig. 36). By measuring at different frequencies, the resistivity can be determined as a function of skin (penetration) depth [ $\delta$  (in kilometers)  $\approx \frac{1}{2}\sqrt{\rho\tau}$  kilometers, where  $\tau$  is the period of the electromagnetic wave].

By measuring at multiple positions and combining that information with geologic and geophysical data, it is possible to create a geologic model that can be used to indicate suitable drilling sites (Fig. 37).

Magnetotellurics has been used for oil exploration in the overthrust belts of the western United States and deep sediments of the Gulf coast region. The increased conductivity of hot saline regions associated with geothermal sites makes MT well suited for locating hydrothermal reservoirs. The use of multiple magnetometers (i.e., remote reference magnetotellurics<sup>100</sup>) can significantly reduce the influence of correlated noise.

SQUID magnetometers for MT are typically of 3 axes ( $B_x$ ,  $B_y$ , and  $B_z$ ). Since most MT surveys are done in remote areas, environmental noise is less of a consideration, although the sensitivity desired ( $<100$  fT/ $\sqrt{\text{Hz}}$ ) still makes even distant power line frequencies observable.

**2. Magnetic anomaly detection (MAD)**

Knowledge of the total magnetic field gradient ( $\nabla\mathbf{B}$ ) of an object can allow determination of its magnitude and direction.<sup>101</sup> From Maxwell’s equations, four of the gradients are redundant (e.g.,  $\partial B_y/\partial x = -\partial B_x/\partial y$ ). Thus only five gradient components are necessary to determine  $\nabla\mathbf{B}$  [Eq. (18)],

$$\begin{pmatrix} \partial B_x/\partial x & \partial B_x/\partial y & \partial B_x/\partial z \\ \partial B_y/\partial x & \partial B_y/\partial y & \partial B_y/\partial z \\ \partial B_z/\partial x & \partial B_z/\partial y & \partial B_z/\partial z \end{pmatrix} \Leftrightarrow \begin{pmatrix} \partial B_x/\partial x & \partial B_x/\partial z \\ \partial B_y/\partial x & \partial B_y/\partial z \\ & \partial B_z/\partial z \end{pmatrix}. \tag{18}$$

An eight-element vector/tensor array can also be made from pure magnetometer elements (Fig. 38). This is helpful when

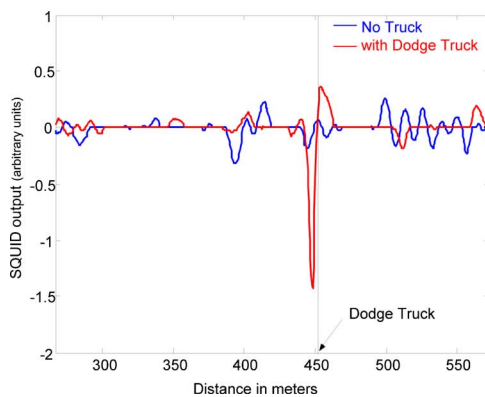


FIG. 39. (Color online) Output of HTS planar gradiometer flying over a commercial vehicle (arbitrary units). The gradiometer was inside a tail mounted stinger on a Cessna Caravan airplane.

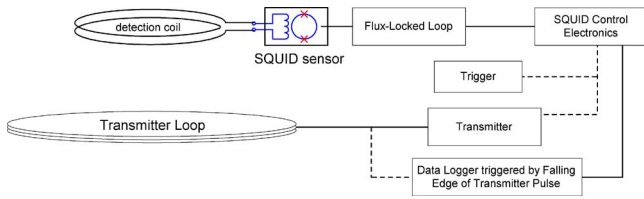


FIG. 40. (Color online) Block diagram of controlled source electromagnetic system.

axial gradiometers are not feasible (e.g., HTS SQUID sensors).

$$\frac{\partial B_x}{\partial x} = X - X',$$

$$\frac{\partial B_x}{\partial z} = X - X'', \quad B_X = \frac{1}{3}(X + X' + X''),$$

$$\frac{\partial B_y}{\partial z} = Y' - Y'', \quad B_Y = \frac{1}{3}(Y + Y' + Y''),$$

$$\frac{\partial B_y}{\partial x} = Y' - Y'', \quad B_Z = \frac{1}{2}(X + Z'').$$

$$\frac{\partial B_z}{\partial z} = Z - Z',$$

It should be noted that superconducting magnetometers are vector devices, and motion in the Earth’s magnetic field produces an output that can mask the desired signal. For airborne gradiometer systems, noise cancellation (compensation of motion-induced artifacts) via electronic balancing is the critical technology, not SQUID sensitivity. The detection (distance) limit for such a gradiometer system is proportional to the fourth root of magnetic moment of the object being detected. MAD has potential uses in mineralogical surveys and unexploded ordinance.<sup>102</sup> MAD has also been used for detection of vehicles and naval vessels (Fig. 39).

**B. Active methods**

Rather than using the electromagnetic field generated by the solar wind, active methods create a time dependent magnetic field generated by a loop driven by an electric current, with the magnetometer detecting the induced field. Measurements can either be in the time [e.g., transient electromagnetics (TEM)] or frequency (e.g., controlled source audio magnetotelluric) domains.

**1. Transient electromagnetic (TEM) pulses**

TEM uses large excitation coils (covering up to 10<sup>4</sup> m<sup>2</sup>) with currents in the order of 10 A. Pulse lengths range from microseconds up to 1 s. The magnetic fields generated by the loop can be measured with a three-axis magnetometer or an eight-element vector/tensor array. The advantage of the eight-element vector/tensor array is its ability to locate the object being excited by the electromagnetic pulse. Figure 40 shows the key elements of a TEM measurement using relatively small field excitation coils.<sup>103</sup> Targets were centered in the transmitter coil, which had three turns with a current of .01 A (65 nT effective field).

Figure 41(a) shows the five independent tensor gradients over the 10 cm diameter hollow (30 mm thick) copper sphere. As expected, all of the gradients have defined similar time constants (about 0.5 ms) for the sphere. The longest computed time constant for the copper sphere is 0.9 ms. This variation in the uniformity of the source pulse field over the target leads to an effective shorter time constant than would be expected. Figure 41(b) shows the tensor gradients over the 30 mm projectile. For this target, it appears that the geometric variation in the source pulse field has resulted in some distortion of the gradient response. However, it does illustrate that the tensor gradients from the 30 mm target are significantly different, which can be used for discrimination of the target type.

Reference 104 is a good introduction to TEM using a three-axis coil array. Because of the vector nature of SQUID magnetometers, the use of SQUIDS in mobile applications requires special attention to motion-induced noise. Reference 105 discusses a “hand held” system while Ref. 106 discusses an airborne system.

**2. Controlled source audio magnetotellurics (CSAMT)**

In some situations, natural (e.g., electrical fields generated in the ionosphere as the excitation current) signals are sometimes not available at the time, frequency, and amplitudes desired. Generating artificial excitation currents locally can overcome the lack of sufficient signal strength needed for the desired measurement. CSAMT is a frequency-domain method that replaces the excitation current generated by ionospheric electric fields with a current fed into the earth by a grounded dipole several hundred meters long. The actual depth to which a target can be imaged depends on the resistivity of the earth at the measurement site and the lowest

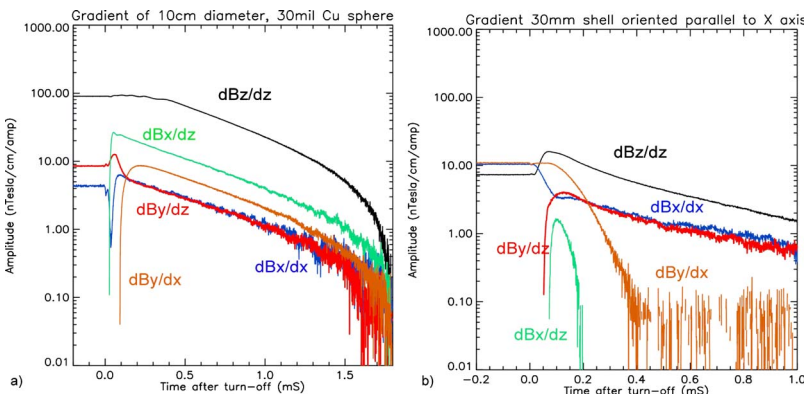


FIG. 41. (Color online) 1 μs interval data from Ref. 104 for (a) copper sphere and (b) artillery shell.

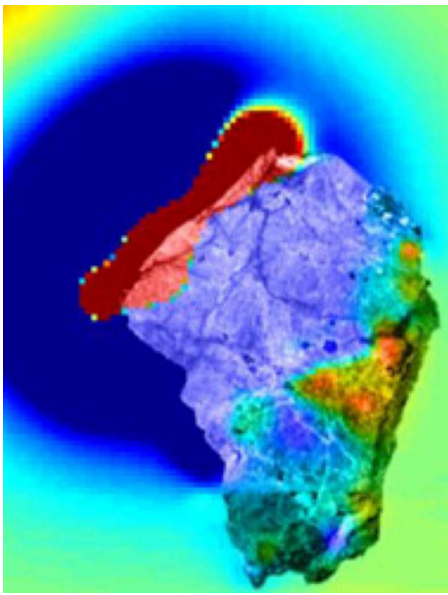


FIG. 42. (Color online) Magnetic microscope image of Martian meteorite ALH84001, after Ref. 110.

frequency for which there are reliable data. Audiofrequency (10 Hz–20 kHz) CSAMT can generate data to depths of 500 m. Extending the excitation down to 0.1 Hz can allow measurements down to 1 km depths.

### C. Rock magnetometry

Knowledge of the magnetic field orientation of a rock or core sample can give information as to how the rock was formed.<sup>107</sup> By changing the thermal history of the sample, it may be possible to determine the Curie and/or Néel temperature of the rock's constituents. By raising the applied field

above the saturation field of any ferromagnetic components, it may be possible to study paramagnetic components. Normally, a three-axis rock magnetometer is used for paleomagnetic measurements. By using orthogonal field coils ( $B_x$ ,  $B_y$ , and  $B_z$ ) or rotating the sample in a single coil, the anisotropy of the sample can be determined. Time dependent behavior can also be studied after rapid changes in either temperature or applied field.

There are multiple ways to measure the remnant magnetic moment of rock samples. The most convenient way is to place the sample inside orthogonal field coils. The use of LTS SQUID sensors allows sensitivities of  $10^{-10}$  emu ( $10^{-13}$  A m<sup>2</sup>) to be reached, equivalent to  $10^{-8}$  A/m for a 10 cc rock sample. Room temperature access to the measurement region is desirable. SQUID rock magnetometers are quite similar to SQUID susceptometers (Sec. VII C) in terms of their basic design. The main differences are larger sample tube bore size (7.6+ cm rather than 1 cm), a more limited temperature range (usually fixed at room temperature rather than variable temperature), and measurement at zero applied field (although, depending on instrument design, measurements in applied fields can be made). If the region of sensitivity of the detection coil(s) is small relative to the sample size, it may be possible to measure the magnetization as a function of position by slowly moving it through the coil's sensitive region. A major advantage of the LTS rock magnetometer is its ability to shield environmental noise. This is in part due to the use of long metallic (usually stainless steel) sample tubes and a sample region that is surrounded by mu-metal shield, a superconducting shield, a superconducting magnet, or some combination thereof.

A variation on the traditional rock magnetometer is the spinner magnetometer. In this case, the sample is rotated

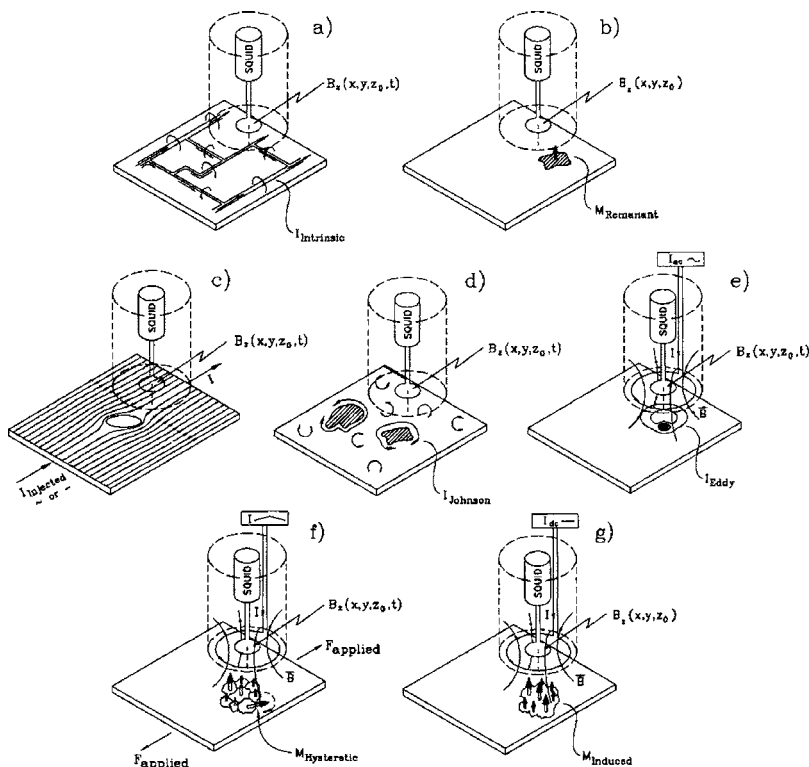


FIG. 43. Measurement configurations for SQUID NDE: (a) intrinsic currents, (b) remnant magnetization, (c) flaw-induced perturbations in applied currents, (d) Johnson noise or corrosion activity in conductors, (e) eddy currents induced by an applied ac magnetic field, (f) hysteretic magnetization by application of stress or an applied field, and (g) diamagnetic and/or paramagnetic materials in an applied field.

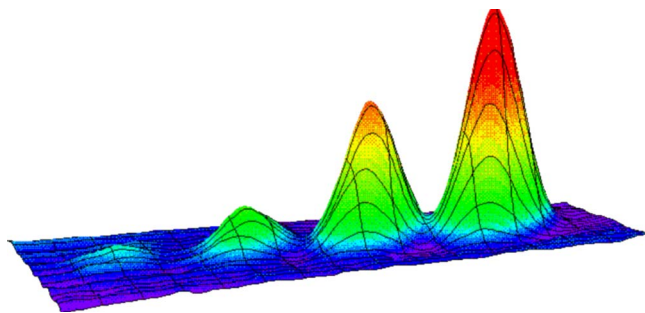


FIG. 44. (Color online) Scan of 1, 3, 5, and 10 mm holes in a steel plate.

beneath a SQUID magnetometer. In this situation, the sample is not tightly coupled to the sensing magnetometer; thus sensitivity will be significantly reduced. Rotating the sample on two axes permits the orientation and magnitude of the rock's magnetization to be determined. A lock-in amplifier (synchronized to the rotation) should be used to increase sensitivity and to ensure accurate measurement of the magnetization axes as the sample is rotated. Sensitivities of  $4 \times 10^{-5}$  A/m have been achieved<sup>108</sup> using 100 fT/ $\sqrt{\text{Hz}}$  HTS SQUID magnetometers.

SQUID microscopes (IX C) can also be used to image magnetization (Fig. 42) in slices taken from rock samples<sup>109</sup> with submillimeter spatial resolution. This can yield highly detailed maps with the ability to resolve a single grain in a rock.

## IX. NONDESTRUCTIVE TEST AND EVALUATION

Magnetic sensing techniques (Fig. 43) such as eddy current testing have been used for many years to detect flaws in structures. A major limitation on their sensitivity is the skin depth  $\lambda$  (the distance where the field is attenuated by a factor  $1/e$ ) of metallic materials. For a sinusoidal varying wave,  $\lambda = \sqrt{\rho / \pi \mu_0 f}$ , where  $f$  is the frequency of the applied field,  $\rho$  is the electrical resistivity, and  $\mu_0$  is the magnetic permeability of free space. Because SQUID sensors have true dc response and superior sensitivity, they can see “deeper” into metallic structures. dc response also means that they can detect remnant magnetization—without the need for externally applied magnetic fields. Their flat frequency response and zero phase distortion allow for a wide range of applications.

The presence or absence of magnetic materials makes it possible to detect perturbations or flaws. Figure 44 shows the magnetic field due to holes in a ferromagnetic plate. This leads to the potential application of SQUIDs in detection of stress or corrosion in reinforcing rods (rebar) used in bridges, aircraft runways, or buildings.

### A. Measurement techniques

Magnetic susceptibility is normally measured by applying an external magnetic field ( $\mathbf{H}$ ) in the same orientation as the detection coil(s). If the material being studied is isotropic, the response of the material to the applied field will be sufficient to determine the material's magnetic properties. For the purposes of this discussion, let us assume that both the field and detection coils are oriented vertically (in the  $z$  direction).

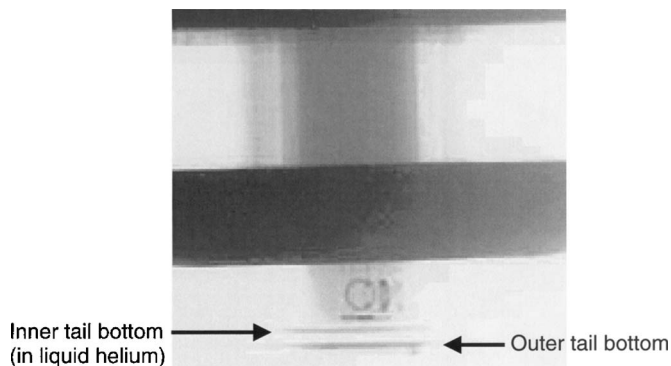


FIG. 45. X-ray of vector set ( $B_x$ ,  $B_y$ , and  $B_z$ ) of detection coils (2-mm-diam).

If the material is anisotropic, there will be field components generated in directions other than the ( $z$  axis) orientation of the field coil. In this situation, transverse detection coils (e.g., coils oriented in the  $x$  or  $y$  directions) would be needed to detect the anisotropic response. Figure 45 shows the tail section of a microSQUID™ system with “vector” ( $B_x$ ,  $B_y$ , and  $B_z$ ) detection coils. Alternatively, the field (e.g.,  $H_x$  or  $H_y$  or both) could be generated transverse to the ( $B_z$ ) detection coil(s). Any anisotropic response would be detected in the vertically oriented detection coil. Superconducting magnets can generate dc fields  $>0.1$  T a few centimeters beneath the end of the magnet. Placing the superconducting magnet in a persistent mode minimizes or eliminates field drift. This can allow detection at or near the theoretical sensitivity of the detection coil. Because of the inductance of multiturn coils of sufficient turns to generate large fields, the maximum field strength of ac magnets is significantly smaller (fractions of a millitesla rather than fractions of a Tesla) than persistent mode superconducting magnets. Thus the ultimate sensitivity of a dc susceptibility measurement system will be greater than an ac susceptibility measurement system.

In flaw detection, it may be desirable to have a uniform current flow that creates a uniform magnetic field. Any distortions (cracks, imperfections, inclusions, etc.) will cause the current path(s) to be distorted with a resultant nonuniform magnetic field. Imaging of the nonuniform magnetic field will allow identification of the causal distortion(s). A sheet inducer (Fig. 46) can be used to generate horizontal currents.<sup>110</sup>

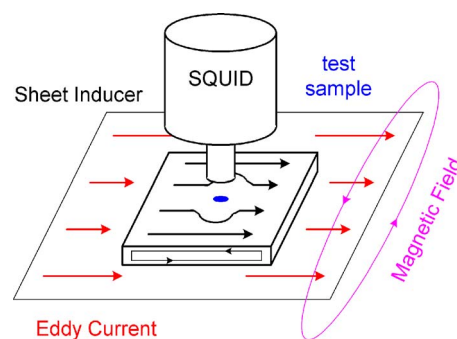


FIG. 46. (Color online) Sheet inducer.

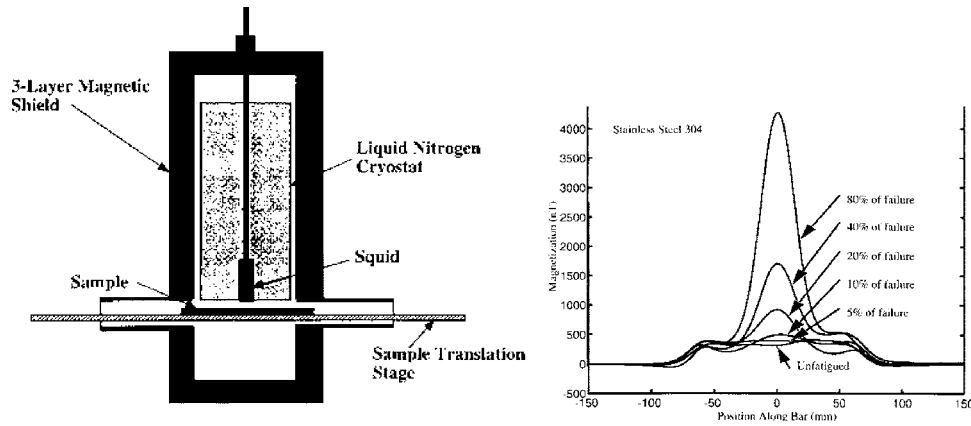


FIG. 47. Side view of Tristan NLD-510 Dewar in MS-830 showing customer constructed sample translation stage and measurements of 304 stainless steel as a function of percent of failure (Ref. 111).

### 1. Magnetization and strain

Stress and strain can have significant effects on the magnetic properties of materials. A particular advantage of magnetic sensing is in examining defects beneath insulating barriers. For example, a clad pipe with asbestos lagging can be quickly examined because the insulating barriers are virtually invisible to magnetic detection—the asbestos need not be removed or cut into. A similar use would be to detect corrosion underneath paint or other opaque coverings.

Another potential application of SQUIDs is in detection of stress or corrosion in reinforcing rods (Fig. 47) used in bridges, aircraft runways, or buildings. Certain types of steel (e.g., Tripp steel) take on an increasing magnetic dipole character as it is strained (Fig. 48). At zero strain, the strain signal has a multipole nature (looking like a sine wave with numerous maxima and minima and an amplitude of a few volts. When the sensor is strained, the magnetic field pattern becomes pure dipolar in nature with the amplitude proportional to the applied strain.

### 2. Effect of intervening materials

Unlike eddy current measurements, which have a skin depth that is frequency dependent, the true dc response of a SQUID magnetometer allows measurements with little, if any, effect from intervening materials. Figure 49 shows a linear scan of a Tripp steel strain sensor whose relative strain is estimated at  $\sim 10\%$ .

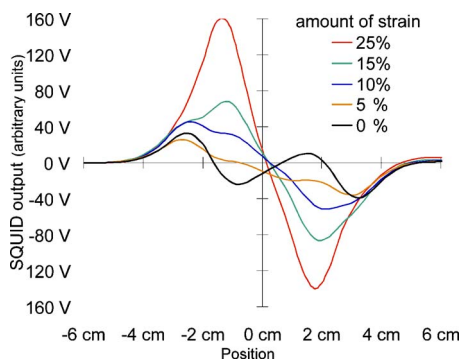


FIG. 48. (Color online) On-axis magnetization of strain sensor.

The strain sensor was measured by a LTS SQUID gradiometer in an unshielded environment, first with an air gap between the sensor and the SQUID magnetometer. A 3/8 in aluminum plate was then placed in the gap between the sensor and the SQUID magnetometer. Finally a 1/8 in-stainless steel plate was placed between the sensor and the SQUID magnetometer. As can be seen, the dc response of SQUID magnetometers allows penetration depths not possible with eddy current or other ac measurement techniques. Intervening materials can also be nonmetallic. Figure 50 shows two-dimensional (2D) magnetic field maps of the same embedded strain sensor measured beneath a variety of intervening materials.

It should be noted that the peak-to-peak heights of the maxima and minima in Figs. 50(a) and 50(d) are the same, indicating no attenuation of the detected signals.

### B. Sensitivity calculations

In reality, the purpose of NDE measurements of most samples is not to determine the magnetic field emanating from the sample, but to determine the magnetic moment(s) of the sample's constituents. Thus, the best figure of merit in assessing magnetic scanners and microscopes is the minimum detectable magnetic moment  $M_{\min}$ . For purposes of calculating  $M_{\min}$ , we can model small samples as a small loop where the magnetic moment is the equivalent current in the loop times the area of the loop ( $A \text{ m}^2$ ). For a bare SQUID

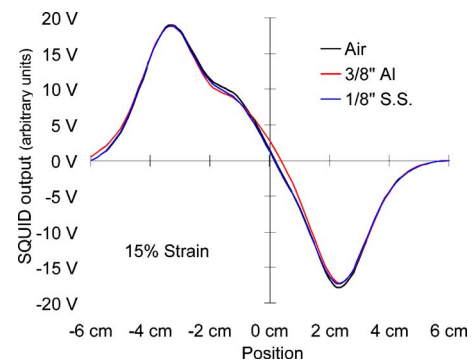


FIG. 49. (Color online) Effect of intervening materials.

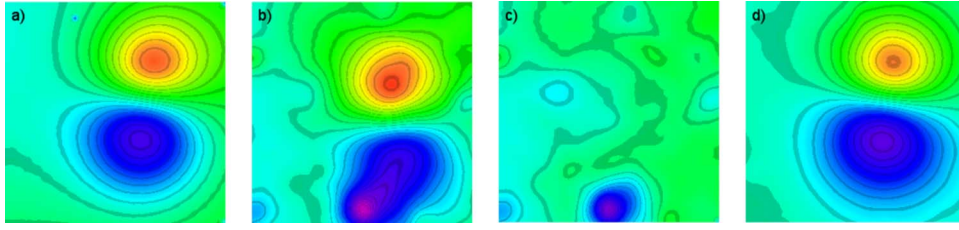


FIG. 50. (Color online) Magnetic field maps of a room temperature embedded strain sensor under a 4-cm-thick concrete overcoating. (a) Bare sensor showing dipole characteristics; (b) sensor under concrete; (c) bare concrete. Image (d) = b–c is a digital subtraction of B and C showing that it is possible to image objects deep underneath magnetically complex coverings. The scans cover a  $6 \times 6 \text{ cm}^2$  area.

with no input coupling coil (typical of HTS SQUIDs used in magnetic microscopes), the flux in the SQUID is given by

$$\Phi_{\text{SQUID}} = B_{\text{SQUID}} A_{\text{SQUID}} = m_{\text{SQ-sample}} I_{\text{sample}}, \quad (19)$$

where  $B_{\text{SQUID}}$  is the field in the SQUID loop,  $A_{\text{SQUID}}$  is the area of the SQUID loop,  $m_{\text{SQ-sample}}$  is the mutual inductance between the SQUID loop and the sample (which is modeled as a tiny loop), and  $I_{\text{sample}}$  is the equivalent current of the sample. Rearranging Eq. (19) by substituting the minimum detectable field change and replacing  $I_{\text{sample}}$  by  $M_{\text{min}}/A_{\text{sample}}$ , where  $A_{\text{sample}}$  is the area of the sample gives

$$B_N A_{\text{SQUID}} = m_{\text{SQ-sample}} M_{\text{min}} / A_{\text{sample}}. \quad (20)$$

Thus,

$$M_{\text{min}} = B_N A_{\text{SQUID}} A_{\text{sample}} / m_{\text{SQ-sample}}. \quad (21)$$

If a SQUID with an input coil and a separate detection coil (e.g., Fig. 18) is used, then,

$$M_{\text{min}} = B_N (L_{\text{SQUID}} + L_{\text{detection coil}}) A_{\text{sample}} / m_{\text{SQ-sample}} \quad (22)$$

with the SQUID's input current noise set to be equal to the current induced in the coil. Using the notation of Secs. IV D–IV F for an axial gradiometer detection coil, Eq. (22) becomes

$$M_{\text{min}} = I_N (L_{\text{signal}} + L_{\text{comp}} + L_{\text{input}} + L_{\text{lead}}) A_{\text{sample}} / m_{\text{SQ-sample}}. \quad (23)$$

For samples smaller than the detection coil ( $A_{\text{sample}} < \frac{1}{4} A_{\text{SQUID loop}}$ ), the size of the sample does not affect the sensitivity calculations. Further analysis will show that maximum sensitivity occurs when the coil (or SQUID loop) diameter  $\approx 1.7 \times$  the coil-to-sample (lift-off) distance. Thus—if field sensitivity is important (to achieve a reasonable signal-to-noise ratio)—reducing coil diameter to less than 60% of the Dewar gap will not be of great benefit and may actually result in a less desirable (or more expensive) instrument.

### C. Magnetic microscopes

Since electrical currents create magnetic fields [Fig. 43(a)], the ability to measure small magnetic fields offers the potential to locate the causes of semiconductor failures. In failed integrated circuits (IC), a short circuit would appear as a small area of intense magnetic flux. By overlaying a magnetic map (created by scanning a SQUID sensor over an IC) onto a computer-aided design (CAD) map of an IC's features

(Fig. 51), it is possible to locate where faults occur in a device. Knowledge of where faults are can allow determination why the fault occurred.

SQUID magnetometers have been used to make noncontact measurements of electronic circuits<sup>112</sup>—one instrument has better than  $10 \mu\text{m}$  resolution.<sup>113</sup> Such instruments with megahertz bandwidths could be used for circuit board and IC mapping. Reference 114 gives an excellent overview of SQUID NDE research. Using commercially available HTS SQUID microscopes, it is possible to detect 10 nA currents flowing in a conductor that is  $100 \mu\text{m}$  from the sensor.

Key to deciding on the type of instrument to be used is the required sensitivity and spatial resolution. Since these tend to be mutually exclusive for a given device, the user needs to decide what requirements are most critical. For example, micron resolution is meaningless if there is no sufficient sensitivity to detect the features being scanned.

The figures of merit used to assess these devices include the following.

*a. The spacing between magnetic features.* This is a key concern. A single dipole can be localized ten times better than resolving two closely spaced dipoles. The smaller and closer the detection coil, the better.

*b. How close you can get to the magnetic feature.* In essence, the detectable feature size is—to first order—a product of coil area and stand-off distance. Getting closer will improve signal-to-noise ratio, but getting much closer than a detection coil diameter gives no significant improvement in spatial resolution, especially for multiple sources.

Desired spatial resolution can also affect scan time. A  $100 \times 100$  point scan can take nearly 3 h to complete if the magnetometer acquires data for 1 s at each data point. Shorter acquisition times can speed up scan time, but at the

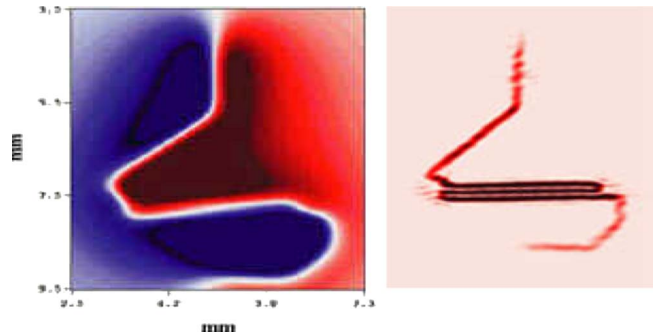


FIG. 51. (Color online) Magnetic field map generated by current flow and its deconvolved current map.

expense of field sensitivity (since SQUID noise is proportional to the square root of the measurement time).

Let us consider scanning magnetic microscopes based on differing technologies:

- (1) conventional LTS SQUID scanner,
- (2) scanning LTS SQUID microscope,
- (3) conventional HTS SQUID scanner, and
- (4) HTS SQUID microscope.

### 1. LTS SQUID scanning system

This system uses a niobium liquid helium (LTS) SQUID sensor and a separately wound detection coil (or coils). It requires the detection coil to be either immersed in liquid helium or in vacuum, but thermally anchored to a 4.2 K bath. Conventional coils can be wound with less than 2 mm diameter. Combined with a 2 mm stand-off, spatial resolutions (for a single dipole)  $<250 \mu\text{m}$  are possible. The ability to use a three-dimensional structure for the detection circuit allows significant external noise rejection. Another advantage of niobium-based superconductors is the ability of the detection coils to operate in tesla fields. This gives the LTS microscope the ability to make susceptibility measurements on the same spatial resolution scale. In addition, these systems can operate in multigauss ac fields with dc to 50 kHz bandwidths for eddy current measurements. The LTS SQUID scanner has the best field sensitivity ( $<10 \text{ fT}/\sqrt{\text{Hz}}$ ) of any magnetic field microscope. Versions of the LTS SQUID scanner have been available for more than 20 years.<sup>112</sup>

A variation on traditional LTS scanner is the use of submillimeter diameter coils or fractional turn SQUIDs combined with millimeter or smaller lift-off distances.<sup>54</sup> In this ultrahigh resolution scanning SQUID microscope, the detection coil was a  $500 \mu\text{m}$  diameter NbTi pickup coil wound on a sapphire bobbin. The coil is located in the vacuum space of the cryostat separated by a  $25 \mu\text{m}$  thick sapphire window from the room temperature samples, with a distance of  $\sim 250 \mu\text{m}$  between the coil and sample. Thermal anchoring of the sapphire bobbin to the helium bath kept the detection coil well below the transition temperature of NbTi. External noise required full sensitivity ( $<100 \text{ fT}/\sqrt{\text{Hz}}$ ) measurements to be done in a magnetic shield. Alternate versions of this scanner could use smaller diameter bobbins or monolithic SQUIDs for higher spatial resolution. Fractional turn SQUIDs have the disadvantage of poorer spatial resolution when resolving magnetic dipoles.<sup>54</sup>

### 2. LTS scanning magnetic microscope (SMM)

This system<sup>70</sup> uses a monolithic array of SQUID sensors and LTS coils. Up to nine (linear array)  $14 \times 14 \mu\text{m}^2$  coils are at the end of a cantilever that is suspended over the sample. The sample is cooled to allow the detection coils to be within a few micrometers of the sample, yielding  $2 \mu\text{m}$  spatial resolution (Fig. 52). While that accuracy is not sufficient to locate a specific submicron transistor, it can place defects in a particular region so other tests can be performed. The use of superconducting stepper motors allows  $0.16 \mu\text{m}$  X-Y resolution on the scanning stage. Since the sample and coils are cooled, superconducting shielding can be used to

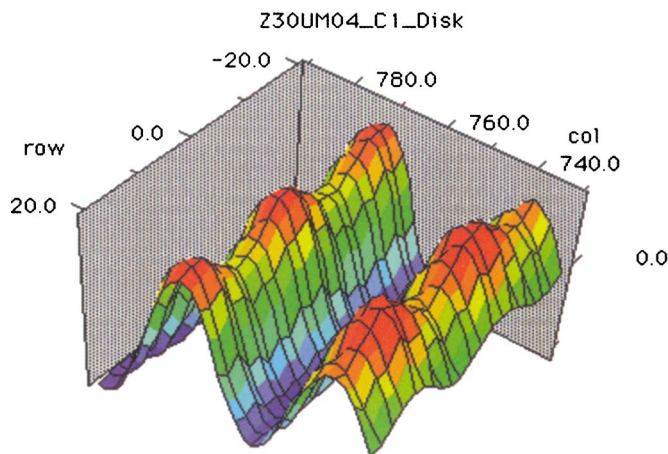


FIG. 52. (Color online) Magnetic image of data on a hard disk. Measurements were made at a vertical stand-off of  $30 \mu\text{m}$ . The bit spacing is  $10 \mu\text{m}$  and the intertrack spacing is  $15 \mu\text{m}$ .

eliminate all external noise sources. Sample loading requires the cryostat to be warmed up, but the use of load-locks may allow scanning electron microscope (SEM) style sample handling. It is also possible to add field generation coils to apply small dc and ac fields for susceptibility and eddy current measurements.

The LTS scanning magnetic microscope has a field sensitivity  $<100 \text{ pT}/\sqrt{\text{Hz}}$ . A relatively mature technology, it has a low risk factor in terms of technology development. One such system<sup>70</sup> has been operating for over ten years.

### 3. HTS SQUID scanning system

The high temperature (HTS) version of the LTS scanner Sec. IX C 1 uses a YBCO HTS SQUID sensor. The inherent anisotropic nature of the HTS superconductors require that the planar detection coil be integral or inductively coupled to the sensor, unlike the LTS scanner that can use three-dimensional gradiometer coils for improved noise rejection. Commercially available HTS sensors have typically consisted of a single turn coil with a 8 mm hole with sensitivities as low as  $20 \text{ fT}/\sqrt{\text{Hz}}$ .

If operated outside a shielded room, environmental noise may exceed the available dynamic range of the higher sensitivity magnetometers. Decreasing the HTS coil size (which can improve spatial resolution, see Fig. 54) to decrease sensitivity may allow unshielded operation. The fixed dynamic range and decreased input sensitivity translate to a higher maximum input signal. Unshielded operation can also be achieved by using a planar (e.g.,  $dB_z/dx$ ) gradiometer. The typical 500:1 balance attenuates the rfi and power line interference sufficiently for the flux-locked loop to hold lock. A typical sensitivity for a 10 mm base line planar gradiometer is  $50 \text{ fT}/\text{cm}/\sqrt{\text{Hz}}$ . Obviously, the system output will reflect that of a planar gradiometer rather than that of a magnetometer.

Unlike LTS SQUIDs, HTS SQUIDs do not have the ability to operate in tesla fields. It is possible to operate a HTS scanning system in millitesla fields. HTS systems have been operated in milligauss ac fields with dc to 20 kHz bandwidths. This makes them the preferred (HTS) device for sus-



FIG. 53. (Color online) SSM scan of the ink in the region around George Washington's right eye on a one dollar bill.

ceptibility and eddy current measurements on macroscopic samples. Typically, sensor-to-sample distances are  $< 1$  cm, although Dewars can be made with 2 mm stand-off distances.

#### 4. HTS scanning SQUID microscope (SSM)

Conceptually identical to the LTS scanning magnetic microscope (Sec. IX C 2), the SSM typically uses the bare SQUID loop ( $\sim 50 \mu\text{m}$ ) as the detection coil. Operating in the Dewar vacuum space (but thermally anchored to the liquid nitrogen bath or closed cycle refrigerator) stand-off distances  $< 100 \mu\text{m}$  are possible.<sup>52</sup> The SSM (because of its smaller detection "coil") has a sensitivity  $\sim 10 \text{ pT}/\sqrt{\text{Hz}}$ . SSM's normally achieve close spacing by either fixing the SQUID sensor to the bottom of the Dewar or having a mechanism that allows for external adjustment of the coil position to compensate for thermal contraction.<sup>115</sup>

Unfortunately, its magnetometer detection coil configuration may make it susceptible to external noise sources (depending on the local environment). Operation in a shielded environment can improve noise immunity. By using phase sensitive detection (injecting an ac current into the device under test), background noise can be filtered out. The addition of external field coils can make susceptibility measurements (dc or ac) possible.

The use of a ferromagnetic flux transporter<sup>116</sup> can offer significant improvement in spatial resolution in HTS microscopes, but at a loss in ac response. One use for a SSM is measurement of current traces. By overlaying SSM images on a CAD map of an IC or circuit board features, it is possible to locate where actual faults occur (Fig. 51). Under ideal conditions, a SQUID can detect as little as 10 nA flowing in a conductor that is  $100 \mu\text{m}$  from the sensor. Other uses are in magnetoimmunoassay (Sec. IX F), paleoarcheology (Sec. VIII C) and detection of counterfeit currency (Fig. 53).

#### D. Sample movement and scan time

To avoid motion-induced noise (caused by moving the SQUID sensor in the Earth's magnetic field), the sample is moved underneath the SQUID sensor. The typical measurement sequence in SQUID microscopy is serpentine step and measure. After each movement, there is a short (usually user specified) settling time after which the measurement is made (again for a user specified interval) after which the sample is moved to the next measurement position. Total scan time is a product of the number of measurements and the distance

between each step, the speed of the sample translation stage, the wait) time and the measurement time at each step.

Assuming 1 s between measurements, a scan of a  $1 \text{ cm}^2$  area with a  $100 \mu\text{m}$  step size will take nearly 3 h. Obviously, shortening the measurement time (e.g., by continuously measuring with moving the sample) will reduce the scan time, but with the penalty of increased noise ( $B_{\text{noise}} \propto \sqrt{\text{measurement time}}$ ). In many situations, sample variations will be significantly higher than system noise. It may be worthwhile to prescan the sample with a short measurement time and a step size significantly greater than the desired spatial resolution to identify which parts of the sample will require higher resolution scans. Subsequent scans can be done in selected regions with the much smaller step sizes; this avoids excessively long measurement times.

#### E. Microscope selection

Environmental noise can have a significant effect on microscope operation. Many HTS microscopes operate unshielded because of their significantly reduced sensitivity compared to LTS microscopes. Even so, care must be taken to ensure that the microscope is not placed in an environment where external noise sources dominate to the point of preventing the SQUIDs from being able to operate. One way to avoid this is to enclose the microscope in a magnetic shield. Alternatively, use of gradiometers can allow unshielded operation. This is especially true for LTS devices. For HTS devices where high (submillimeter) spatial resolution is not as important as field sensitivity, planar gradiometers offer a way to operate unshielded and avoid the complexity of a shielded enclosure.

The choice of microscope system depends on the needed spatial resolution and magnetic field sensitivity. Resolution (the minimum separation between two magnetic features) is dependent on both the distance from the sensor to the sample (lift-off) and detection coil size. If a SQUID microscope can place its sensor very close to the sample ( $< 2$  coil diameters), then the coil size is the limiting factor to resolution.

Because the flux sensitivity of SQUID sensors is roughly constant (for a given type of SQUID sensor), there is an inverse relationship between sensitivity and spatial resolution. Figure 54 shows the trade-off between sensitivity and spatial resolution for a number of different SQUID sensors.

#### F. Magnetic assays (immunoassays)

Similar to tagging molecules with radioactive isotopes (radioimmunoassay), fluorescent molecules, light scattering particles, and enzymes for the production of chemiluminescent signals, magnetic particles tens of nanometers in size can be used to tag molecules to investigate biological and chemical reactions. These tagged particles can be localized after paper chromatography or other such separation process by measuring their remnant magnetic field(s). SQUID based magnetic microscopes are well suited to this task. Subjecting the magnetic nanoparticles to an external magnetic field and (after switching off the field) measuring the relaxation of the magnetization can give information about the nanoparticles by differentiating between the differing relaxation times due

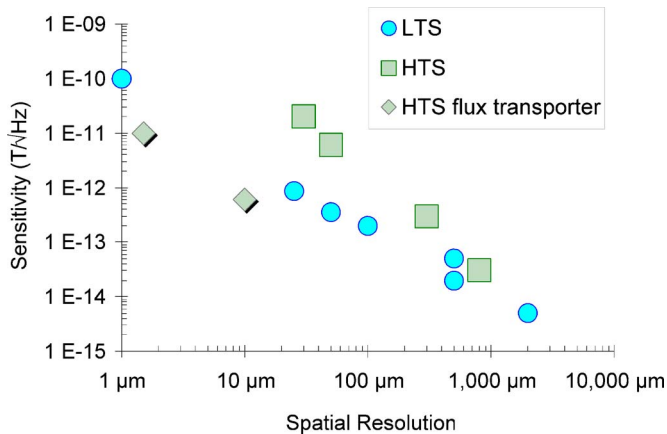


FIG. 54. (Color online) Sensitivity and spatial resolution of a number of SQUID microscopes.

to the movement of entire particles (Brownian motion  $\sim 10^{-5}$  s for a 20 nm particle) and rotation of the magnetization vector inside the particle (Néel relaxation: 0.01–10 s). This use of magnetorelaxometry can allow identification of bound and unbound molecules by discriminating between the different relaxation mechanisms. Reference 117 describes a LTS system utilizing a planar gradiometer for magnetorelaxometry measurements.

Figure 55 shows one method of magnetoimmunoassay. An antibody is attached to a marker that is tagged with magnetic particles (e.g.,  $\gamma\text{-Fe}_2\text{O}_3$ ) embedded in a polymer core. For the detection of an antigen, an antibody that selectively couples to the antigen is used. Figure 55 illustrates a capture surface with an immobilized capture molecule for one domain (epitope) of the target and a free label conjugated to another detection molecule, specific for another epitope of the target. In the presence of the target, the label is attached to the capture surface and in the absence of the target, the unbound label can be washed away. Detection occurs after measuring the presence (or absence) of the label on the capture surface.

Issues that affect signal-to-noise ratio are things like nonspecific binding (NSB) and interfering signals from other sample materials. The magnetic detection approach suffers from very little outside interference, unlike many of the other nonradioactive (optical) methods. The approach of magnetorelaxation is a unique means to address the issue of nonspecific binding and washing. The idea is that specifically bound labels will not be free to undergo Brownian rotations

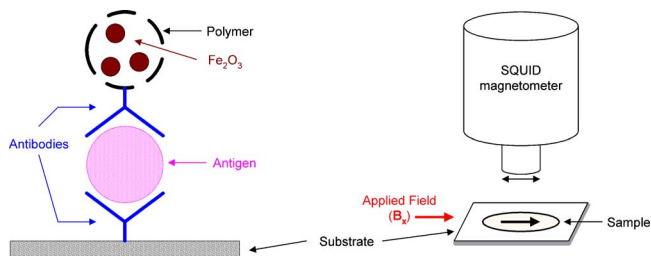


FIG. 55. (Color online) (a) Binding reaction between antibody and antigen in magnetoimmunoassay; (b) schematic diagram of magnetoimmunoassay measurement.

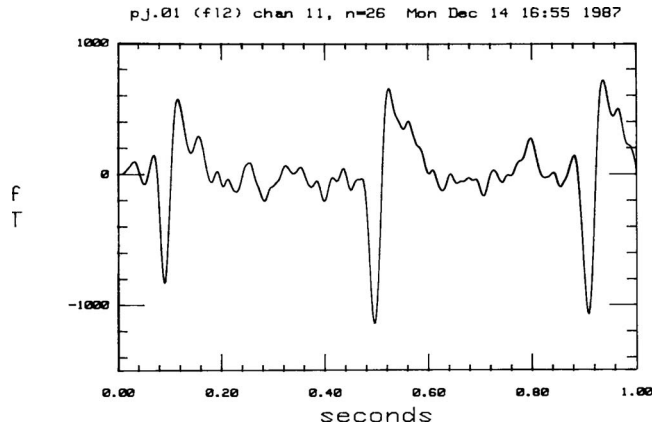


FIG. 56. Magnetocardiogram of fetus (29 week gestation).

as will the free and nonspecifically bound labels. So if the label is designed so that its Néel relaxation time is long compared with its Brownian relaxation time, then the relaxation measurements can potentially distinguish specifically bound labels, even with no washing. Approaches that do not rely on a wash step to separate specifically from nonspecifically bound labels are called “homogenous.”

### X. MEDICAL APPLICATIONS OF SQUIDS

Electrical measurements of physiological potentials are well established in clinical diagnostics. Essentially every phenomenon in electrophysiology has a magnetic analog since a magnetic field is associated with every electric current. Analogous measurements of physiological magnetic fields, however, are relatively unknown to researchers and clinicians. Biomagnetic research encompasses many of the major organs of the body, including the heart (Fig. 56), brain, liver, lungs, and muscles. Several new diagnostic procedures and instruments have resulted from this work. These measurements are proving to be of considerable significance (see proceedings of the various international biomagnetism conferences such as Ref. 48).

As shown in Fig. 57, biomagnetic signals range from essentially dc to several hundred hertz, and the field intensities range from about 50 to  $10^6$  fT. The sources of these

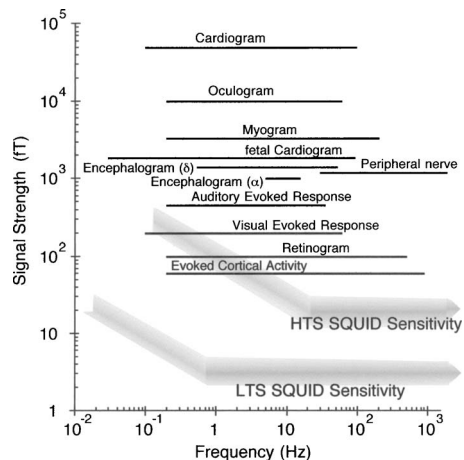


FIG. 57. Typical amplitudes and frequency ranges for various biomagnetic signals (based on a  $\sim 1$  cm tail gap).

TABLE IV. Areas in which SQUID magnetometers are being used in medical research.

Studies of the brain, neuromagnetism	Other medical applications
Epilepsy	Noninvasive <i>in vivo</i> magnetic liver biopsies
Presurgical cortical function mapping	(Ferritometry)
Trauma (closed head injury)	Studies of the stomach, gastroenterology
Drug development and testing	Intestinal and mesenteric is
Stroke	Lung function and clearance studies
Alzheimer's	Peripheral and single nerve studies
Neuromuscular disorders	Organ transplant rejection risk
Prenatal and neonatal MEG	Blood flow disorders
Performance evaluation	Animal systems
Studies of the heart, magnetocardiography	Drug development
Arrhythmia	
Heart muscle damage	
Fetal cardiograph	

fields vary from localized groups of neurons in the brain, to more dispersed muscle tissues in the heart, to magnetic particles distributed throughout the lungs.

There are two key technical advantages in employing magnetic—as opposed to electric—sensors for measuring biological ion currents:

- (1) The generators of electrical activity in the body can be precisely localized to within a few millimeters from their magnetic signals because magnetic signals are not strongly dependent on variations in the body's tissue conductivity as are electrical signals. Furthermore, the body's tissue is effectively transparent to magnetic fields in the biological frequency range.
- (2) Measurement of dc and low frequency phenomena is feasible because of the inherent dc response and low noise of SQUID magnetometers, and because there is no artifact due to changing electrical contact with the body, as is the case when measuring biological potentials with electrodes.

The use of bioelectric signals as a diagnostic tool is well known in medicine, e.g., the electrocardiogram (EKG) for the heart and the electroencephalogram (EEG) for the brain.<sup>79</sup>

The electrical activity that produces the surface electrical activity that is measured by EEG and EKG also produces magnetic fields. The analogous magnetic measurements are known as the magnetocardiogram (MCG) and the magne-

toencephalogram (MEG) (Fig. 57). Other physiological processes also generate electrical activity with analogous magnetic fields.

The development of the SQUID has allowed the development of noninvasive clinical measurements of biomagnetic fields (Table IV). The use of gradiometers can allow measurements to be made in unshielded environments at sensitivities below  $20 \text{ fT}/\sqrt{\text{Hz}}$ . However, neuromagnetic measurements are typically made in room-sized MSR's (Ref. 118) that will allow measurements of the magnetic field of the brain over the entire surface of the head ( $>250$  positions simultaneously).

### A. Measurement techniques

Magnetic fields associated with different physiological functions and conditions vary widely in their intensities, frequencies, and spatial distributions (Fig. 57). Consequently, different techniques and instruments must be used in their measurement.

Magnetic fields from active electrical sources in the body are measured completely passively and external to the body by placing the detector in close proximity to the body's surface. This technique is applicable to the heart, brain, and skeletal muscles. It has been shown in the case of the brain, for example, that a small patch of activated neurons can be modeled as a current dipole<sup>119</sup> that generates a well-defined magnetic field profile (Fig. 58). Measurement of this profile can be used to infer the location of the neuron with consid-

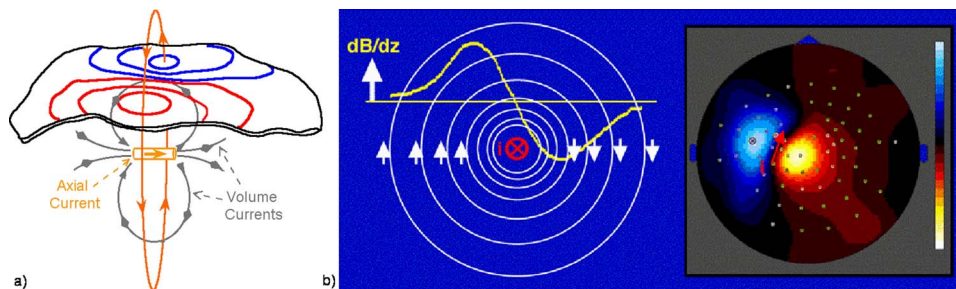


FIG. 58. (Color online) Magnetic field generated by a current dipole. For a sphere, the dipole is located at midpoint of the maxima and minima at a depth = distance  $\Delta \div \sqrt{2}$ .

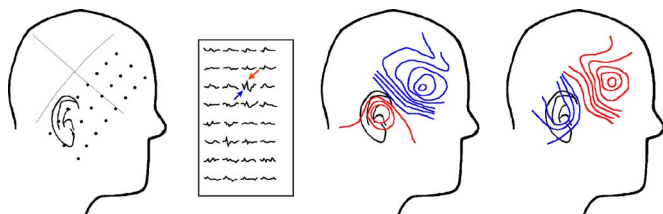


FIG. 59. (Color online) Field contour map generation.

erable accuracy. Using evoked response techniques, the location of signal pathways and information processing centers in the brain can be mapped at different delay times (latencies) following the stimulus. For this purpose, the field is mapped around the surface of the head (Fig. 60).

Systems for measurement of the brain require that the head be surrounded by detection coils. Unlike whole head measurement systems, most other biomagnetometers utilize flat tail Dewars. The channel count and coil arrangement are dependent on the application. If measurements are being made in a MSR, typically the detection coils are first derivative gradiometers. Measurements in unshielded environments require second order gradiometers with a high balance ( $\sim 1:10^6$ ) or in conjunction with reference channels. Unshielded operation requires very high dynamic range and careful attention to be paid to rfi immunity. In both shielded and unshielded environments, synthetic third order gradiometers with first order hardware primary sensors have been successfully used.<sup>45</sup>

Systems for susceptibility measurements use magnets, either integral to the detection coils (Sec. X G) or immediately prior to the measurement (Sec. X H). Care must be taken not to couple field generated noise into the detection coil(s).

### 1. Magnetic mapping

Magnetic fields from active electrical sources in the body can be measured passively and external to the body by placing the magnetometer in close proximity to the body's surface. It has been shown that a spatially compact population of neurons in the brain can be modeled as a current dipole that generates a well-defined magnetic field profile (Fig. 58). Reference 120 gives an excellent review of magnetic source imaging.

To generate a contour map, measurements are taken at a number of points [Fig. 59(a)] and the magnetic field values are determined at a given point in time at each grid point [Fig. 59(b)]. Isofield contours are then generated to yield a field map [Fig. 59(c)]. Time sequenced contour maps can be generated by looking at subsequent time slices [Fig. 59(d)]. The distance between measurements (equivalent to the inter-coil spacing on multichannel systems) is dependent on the depth of the source and the spatial resolution desired.

Mapping of these field profiles can be used to infer the location of the equivalent active dipole site region to within millimeters. Using evoked response techniques, the location of signal pathways and information processing centers in the brain can be mapped at different delay times (latencies) following the stimulus (Fig. 60).

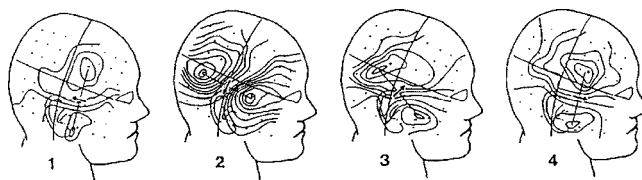


FIG. 60. Neuromagnetic patterns generated by the interictal spike complex in a patient with a partial epileptic seizure disorder. The individual patterns are measured at intervals of approximately 20 ms.

There are also magnetic measurements for which there are no electrical analogs.<sup>121</sup> These are measurements of static magnetic fields produced by ferromagnetic materials ingested into the body and measurements of the magnetic susceptibility of materials in the body. In particular, information on the quantity and depth of diamagnetic or paramagnetic materials (such as iron stored in the liver) can be obtained by using magnetizing and detection coils of differing sizes in the same instrument and measuring the induced field as a function of distance. This technique is being used to clinically monitor patients suffering from iron overload diseases such as hemochromatosis, thalassemia, and sickle cell anemia.

### 2. Magnetic source measurements

*a. Para/diamagnetic sources.* Fields from paramagnetic or diamagnetic materials are measured while a low intensity external magnetic field is applied to a local region of the body and compared with the background field when the subject is removed from the sensitive range of the instrument. Information on the depth of these materials can be obtained by using magnetization and detection coils of differing sizes in the same instrument or by measuring the field as a function of distance from the body.

*b. Ferromagnetic sources.* The location and quantity of ferromagnetic materials in the body, typically due to contaminants in the lungs (Sec. X H), are determined by measuring the magnetic field external to the body before and after a low intensity magnetic field (typically 0.1 T) is applied to magnetize the ferromagnetic material. The distribution of these materials can be determined by applying the field to only a small region of the body at a time.

### B. Sensitivity

As mentioned, the choice of detection coil design is very much dependent on what is to be measured. Although many systems for biomagnetic measurements are described in terms of their ability to detect magnetic fields—a valid assumption when considering noise sources—or magnetic dipole sources, the magnetic dipole does not provide a good model of neurological sources. The most common source model in electrophysiology is that of the current dipole (Fig. 58). The strength  $Q$  of a current dipole has the dimension of current times length and the unit of A m. It is represented by a vector whose direction coincides with the direction of the current. The current dipole is a simplified representation for much more complex patterns of current which exist at the cellular level.<sup>119</sup> The current dipole is useful in that more elaborate extended sources can be represented by an array of

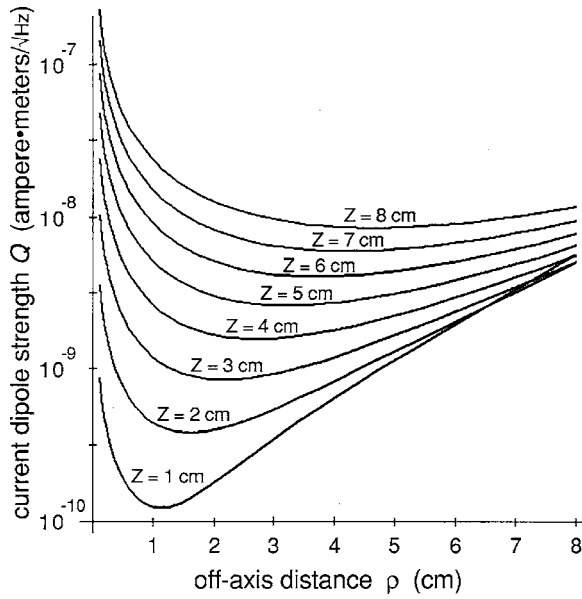


FIG. 61. Minimum detectable current dipole for a first derivative, six turn, 5 ft/√Hz gradiometer with a coil diameter of 2 cm (Ref. 123) as a function of off-axis position ( $\rho$ ) and depth ( $z$ ).

individual current dipoles. The response of a simple magnetometer to a current dipole in free space can be expressed by<sup>41</sup>

$$Q_{\min} = \frac{\pi\Phi_{\min}\sqrt{m}}{\mu_0\sqrt{r}\rho[(1-m/2)K(m) - E(m)]}, \quad (24)$$

where  $m = 4r\rho/\sqrt{[(r+\rho)^2+z^2]}$ ,  $Q_{\min}$  is the smallest current dipole that can be detected,  $\Phi_{\min}$  is the minimum detectable magnetic flux in the pickup coil [see Eq. (3)],  $\mu_0$  is the permeability of free space,  $r$  is the radius of the pick-up coil,  $\rho$  is the off-axis distance (in cylindrical coordinates),  $z$  is the axial distance of the current dipole below the bottom of the pick-up coil, and  $K$  and  $E$  are elliptical integrals of the first and second kind, respectively (the elliptic integrals are a result of integrating the Biot-Savart law over a circular coil area). If only the radial component of the field is measured, these equations are simplified to the radial component of the Biot-Savart law. A more realistic model (taking into account the conducting nature of the brain) is described in Ref. 122. In any case, for a gradiometer, one must sum the response of all the coil windings (accounting for coil polarity) and take into account the base line of the gradiometer. The tail spacing of the Dewar must not be neglected when determining  $z$ . Figure 61 shows minimum detectable current dipole as a function of coil-to-dipole distance.

Unlike the response of a magnetic dipole which goes as  $1/z^3$ , the response of a current dipole goes as  $1/z^2$ . Also, the maximum sensitivity is not located directly beneath the detection coils, but offset (consistent with Fig. 58). For a current dipole in a spherical conducting medium, the  $1/z^2$  law applies only for more superficial sources. For sources approaching the sphere center, the decay exponent monotonically increases.

### C. Magnetoencephalography: Measurements of the brain

The MEG is the magnetic counterpart of the more familiar EEG. The amplitude of the MEG signals is quite small, often less than a picotesla peak-to-peak over the back of the head (Fig. 57). Spontaneous brain activity is readily observed using SQUID magnetometers, without resorting to signal averaging. By making MEG measurements from an array of magnetic sensors, it has been demonstrated that sources of brain activity can be localized to within a few millimeters. By contrast, it is sometimes difficult to localize brain activity to the correct hemisphere when using EEG.<sup>124</sup>

Since magnetoencephalography can be used to associate brain function with the underlying anatomic structure, it may eventually be beneficial in the diagnosis of neurological disorders such as epilepsy, Parkinson's disease, Alzheimer's disease, stroke, and head trauma. The overall anatomic distribution (pattern) of brain activity may also be useful in providing objective measurements relating to psychiatric disorders and their treatment with psychoactive drugs.

The ability of MEG to localize brain activity has prompted clinical research studies of epilepsy.<sup>125</sup> When neurosurgery is indicated in the treatment of epilepsy, the surgeon requires information as to the location and extent of the brain tissue generating the seizures, as well as detailed information of where various brain functions are mapped (the latter to guide where *not* to cut!). Presently, the clinically acceptable method for obtaining this information is by implanting EEG electrodes on or within the patient's brain. Preliminary findings have shown that noninvasive localization of epileptic centers by MEG is in close agreement with findings using invasive electrodes. Presurgical functional mapping is another example where MEG has been used to delineate where various brain functions are mapped. Intensive testing will be required to determine if MEG is reliable enough to stand alone as a guide to the neurosurgeon. Because of its noninvasive nature, MEG promises to reduce both risk and cost to the patient in the presurgical diagnosis of epilepsy.

The first MEG measurements were made with single channel magnetometers. This required multiple placements over the subject's head (Fig. 59) and often took days to complete. Present day MEG systems provide whole head coverage that require hundreds of sensor channels. This allows real-time acquisition of data.

Noise reduction is achieved through the use of MSRs and eight or more element vector/tensor reference arrays. The first multichannel ( $N=5-7$ ) neuromagnetometers used fixed superconducting tabs to improve gradiometer balance from  $1:10^2$  to  $1:10^4$ . Because of the labor associated with placing superconducting tabs on hundreds of channels, their use on high channel count systems has been abandoned. Instead, MSRs (sometimes using synthetic methods<sup>45</sup>—similar to the generalized Eq. (8) with field balance of about  $10^5$ ) are used to provide shielding of external noise. Typically, the detection coils of MEG systems are first order gradiometers, either hand-wound axial ( $dB_z/dz$ ) or planar (paired  $dB_x/dz$  and  $dB_y/dz$ ). The advantage of planar coils is that their intrinsic balance is superior to that of hand-wound axial coils.

The disadvantage of planar coils is that their base line is much shorter than that of axial coils; this gives axial coils an advantage when measuring deep sources. While pure magnetometers have been used (to maximize sensitivity), their inability to reject common mode noise makes them much more susceptible to low frequency noise in drift (e.g., <10 Hz) signals generated by high speed rail lines). Magnetometers can be used only in well shielded environments, such as the Berlin MSR or whole body superconducting shields.<sup>32</sup> The MSR (Fig. 30) gives 30–80 dB of attenuation and the reference arrays another 60+ dB.

Another advantage of the high channel count of whole head systems is the ability to use the array of sensors to image the MEG signals using methods analogous to those applied to radio astronomy. A linearly constrained minimum variance beam former<sup>126</sup> minimizes all signals seen by the sensor array, subject to a constraint for an equivalent current dipole at a specified coordinate. As a result, this beam former has a gain of unity for signals arising from the specified location, while attenuating all other signals. Thus, beam forming can be thought of as “spatially selective noise reduction.” This property permits functional imaging of brain activity without requiring signal averaging and without the need to delete artifacts from eye movement, heart signal (MCG), or environmental magnetic noise. Synthetic aperture magnetometry<sup>127</sup> (SAM) appears to have better spatial resolution [by  $\sqrt{2}$  than the beam former described in Ref. 126 for the 2D MEG case, and better by a factor of  $\sqrt{3}$  than the three-dimensional (3D) beam former].

The large surface area (more than 1000 cm<sup>2</sup>) and complex shape of a whole head Dewar (Fig. 62) usually means thick tail pieces and Dewar gaps of 15–20 mm. Putting the Dewar cavity at an angle to allow the Dewar to be positioned for either seated or supine (lying down) patients increases the design and fabrication complexity. Dewar motion for whole head systems is usually only in the tilt ( $\theta$ ) direction. The patient is located by movement of a three-axis ( $x$ ,  $y$ , and  $z$ ) bed and/or chair.

If infants are to be measured, significantly closer spacing can give significant improvement in signal-to-noise ratio. It should be noted that the scalp and skull of newborns are thin. This makes it possible to measure MEG signals at a distance less than  $\frac{1}{2}$  cm from the brain surface.<sup>128</sup> This shorter distance will result in a large increase in the amplitude of MEG signals from the infant, since the magnetic field is inversely proportional to the square of the distance (Sec. X B). The shorter distance and a high density of detectors can also result in higher spatial resolution.

Ancillary equipments (e.g., patient bed, Dewar gantry, etc.) need to have no time varying magnetic signature. Ferromagnetic components are to be avoided because of their relatively large (microtesla or millitesla) remnant fields. Nonferrous metallic components (which can cause scattering of gradient interference) may be acceptable if sufficiently far from the detection coils.<sup>129</sup>

MEG is presently the largest and most successful commercial application of SQUIDs; more than 20 000 SQUID sensors have been installed in whole-cortex MEG systems.

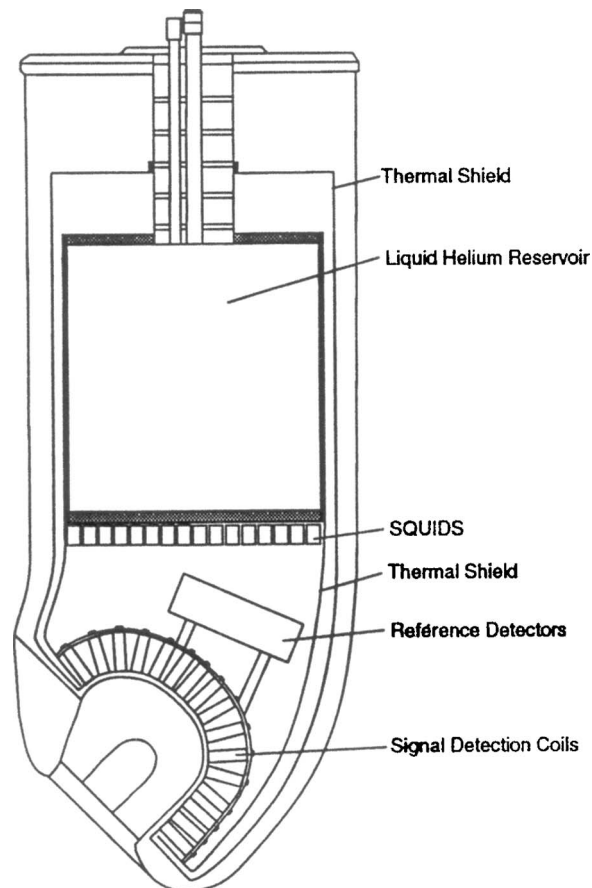


FIG. 62. Whole head neuromagnetometer (coil-in-vacuum construction).

#### D. Magnetocardiography: Measurements of the heart

The MCG is the magnetic signal generated by the heart's electrical activity. The MCG is homologous to the ECG. A peak MCG signal of 50 pT can be measured over the heart. This signal is easily measured by SQUID magnetometer, with excellent signal-to-noise ratio.

Measurement of the heart's conduction system is important in the diagnosis of diseases in which the heart has an abnormal rhythm, reduced mechanical performance, and higher susceptibility to sudden failure. Direct current (dc) MCG measurements have shown that a “current of injury” flows in the heart as a result of myocardial infarction. Although a current of injury signal can also be seen in the ac-coupled electrocardiogram, the magnitude of the injury and the location of the injured region cannot be determined with precision. Using MCG, it may be possible to determine both the location and extent of the injured heart tissue. Clinical studies are under way to test this hypothesis.<sup>130</sup>

The SQUID magnetometer is sensitive enough to noninvasively detect the fetal magnetocardiogram (Fig. 56). The fetal electrocardiogram is often used by physicians as a measure of fetal distress but detection of this fetal heartbeat is often unreliable. This is because, later in gestation, the fetus is coated with an oily substance called the vernix caseosa. The vernix tends to electrically insulate the fetus, greatly attenuating the fetal ECG. By contrast, the fetal MCG is not attenuated by the vernix, making it possible to monitor the

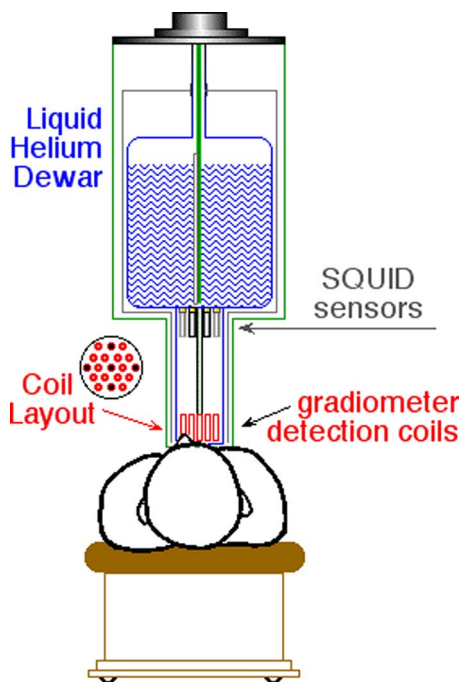


FIG. 63. (Color online) MCG biomagnetometer components (gantry and electronics not shown).

fetal heart through all phases of gestation, including labor. Another advantage of magnetic (as compared to electrical) methods is that the spatial resolution of MCG allows it to better isolate the fetal heart in the presence of the maternal heartbeat.<sup>131</sup>

MCG has also been used to measure the specialized conduction system of the heart. To obtain electrical measurements, it is necessary for the patient to swallow an electrode, which is passed down the esophagus to the level of the heart. Measurement of the heart's conduction system is important in the diagnosis of diseases in which the heart has an abnormal rhythm, reduced mechanical performance, and higher susceptibility to sudden failure.

Cardiac measurements need only a single channel if just the time series MCG (Fig. 56) is of interest. If real-time dipole mapping is desired, additional channels (either in a hexagonal, square, or other arrangement) to more than cover the extrema of the field patterns [Fig. 58(b)] will be required. Figure 63 shows a 19 channel axial gradiometer system with sufficient coverage for single placement measurements.

Typically, MCG systems measure only the vertical ( $B_z$ ) field component. Dewar tails are normally flat with  $\sim 10$  mm gaps. The use of a second order gradiometer is preferred over a first order gradiometer in fetal MCG because of its superior rejection of the maternal MCG.

### E. Magnetomyography and magnetoneurography: Muscle and peripheral nerve measurements

The electrical activity of muscles and peripheral nerves can readily be detected using magnetic sensors.<sup>132</sup> Here the chief advantage of biomagnetometry is its contactless noninvasive nature. In order to make equivalent electrical measurements, it is necessary to pass needle electrodes through the skin into the vicinity of the nerve or muscle.

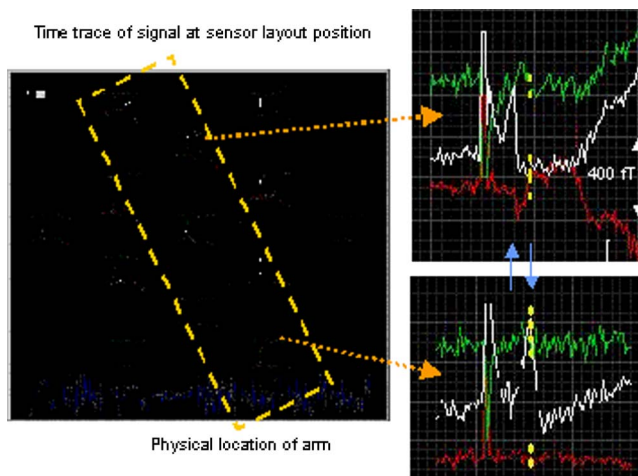


FIG. 64. (Color online) Peripheral nerve signals generated by an electrical shock at the median nerve (the brighter trace is  $B_z$ ; the others are  $B_x$  and  $B_y$ ). The forearm location is shown by the outlined box. The first (vertical) peak is the stimulus artifact. The next peak is the detected peripheral nerve as it travels up along the forearm. The distance between the two (expanded) sensor locations is 5 cm. The peak ( $B_z$ ) of the detected signal between the upper and lower expanded time display has shifted by 2 ms.

Measurement systems for spinal cord or peripheral nerve activities are defined by the temporal characteristics and quasi-one-dimensional geometry of the signal. Neurological events are typically on a 10 ms time scale, while spinal cord and peripheral nerve events are typically on a 1 ms (or faster) time scale. Placement of axial coils directly over the nerve will result in a net zero signal (Fig. 58). Thus, vector coils ( $B_x$  and/or  $B_y$ ) may be desirable. The ideal sensor placement for spinal cord measurements may be that of a long rectangular array rather than the hexagonal arrays that are used in MEG or MCG studies. Figure 64 shows the result of an electrical stimulation of the median nerve. The measurement system consisted of 37 axial ( $B_z$ ) and 13 pairs of vector ( $B_x$  and  $B_y$ ) detection coils laid out in a hexagonal array.

### F. Magnetoenterography: Measurements of the stomach and intestines

Blockage of arterial blood flow (ischemia) in the gastrointestinal tract can lead to intestinal necrosis. Treatment requires surgical intervention to remove or bypass any necrotic intestinal tissue. If diagnosis is delayed, the mortality rate can exceed 50%. Conventional diagnosis of mesenteric artery narrowing or blockage is by an arteriogram that requires a catheter and x-ray dye. Because of the limits of x-ray resolution, arteriograms can only see blockages of blood vessels 1 mm or larger.

The gastrointestinal (GI) tract exhibits two types of electrical activity: a high frequency (in the hertz regime) spiking associated with muscle contraction and low frequency oscillations [cycles/min (cpm)] known as the basic electric rhythm (BER). While the BER can be detected using electrodes, this is a highly invasive procedure. Typically, the signal strength of a BER signal is at the picotesla level. As shown in Fig. 65, ischemic episodes show a marked reduction in the BER.<sup>133</sup> SQUID technology offers the possibility of detection of ischemia by monitoring the BER frequency.

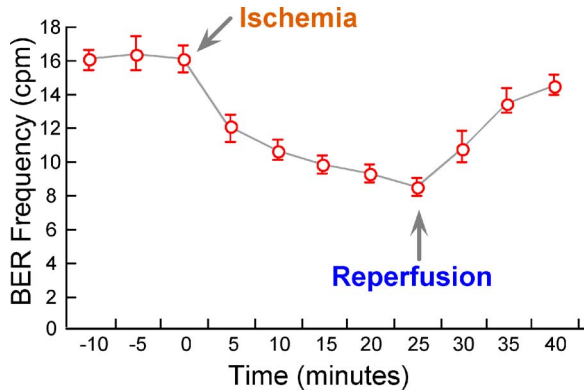


FIG. 65. (Color online) Shift in BER [in cycles/min (CPM)] before and after chemically induced occlusion of a mesenteric (intestinal) artery. The BER frequency varies as a function of position within the GI tract. The gastric BER is typically  $3.2 \pm 0.1$  cpm, the small intestine BER is  $11.3 \pm 0.1$  cpm, and the duodenum BER is  $\sim 12$  cpm.

Instrumentation for magnetoenterography is similar to some magnetocardiography systems in channel count. Typically, a low to medium (19–37) channel count with sensitivity better than  $50 \text{ fT}/\sqrt{\text{Hz}}$  is sufficient to detect and localize the BER. However, since the GI tract has a complex shape that causes the current paths to be in different directions, vector ( $B_x$  and  $B_y$ ) detection coils are recommended in addition to the normal axial ( $B_z$ ) detection coils found in MCG systems. Because of the very low frequency nature of the BER, significant attention must be paid to noise reduction. Highly balanced gradiometers and the use of an eight-element reference array are recommended, especially if unshielded operation is desired. Nonmagnetic ancillary equipments (Dewar gantry, patient bed, etc.) are also required to avoid coupling in environmental noise that could mask the very low frequency picotesla level BER signals.

### G. Ferritometry: Magnetic susceptibility measurements

Although most body tissue is diamagnetic, organs rich in iron—notably the liver—can be strongly paramagnetic due to the iron storage compounds ferritin and hemosiderin. The magnetic susceptibility of an organ can be determined by measuring the small changes in an applied magnetic field when the body is brought into the vicinity of the magnetometer. Diamagnetic tissue will cause a small decrease in the

sensed magnetic field, while paramagnetic tissue results in a larger increase in the sensed field. The magnitude and extent to which the body perturbs the applied field is used to estimate tissue iron concentration.

Figure 66 shows a SQUID susceptibility system (referred to as Ferritometer®) for measuring liver iron stores. The system detects the dc change in flux as a function of position beneath the magnet and detection coils.<sup>134</sup> The applied field is  $\sim 30$  mT directly beneath the Dewar tail, decreasing to a few millitesla a few centimeters beneath the Dewar tail. The water bag simulates the diamagnetic contribution of body tissue ( $\chi_{\text{water}} \approx \chi_{\text{tissue}}$ ), essentially allowing the detection coils only to “see” the movement of the paramagnetic liver. The net change in the dc level of detected flux is related to the organ’s iron concentration and has been proven useful in evaluating the treatment of patients with iron overload disorders. Ferritometer® measurements of liver iron agree well ( $r \sim 0.98$ ) with those obtained by liver biopsy—the only other quantitative measure of iron concentration.<sup>135</sup>

ac fields have been used to magnetize the liver.<sup>136</sup> In this situation, a Helmholtz coil set surrounds the patient. The advantage of the ac technique is that it can reject environmental noise better than dc methods. However, only the dc methodology (which allows significantly higher fields to be applied to the patient than ac methods, Sec. IX A) has been shown to have sufficient sensitivity and repeatability to be clinically useful.

### H. Magnetopneumography: Magnetic remnance measurements of the lung

The human body is normally diamagnetic or paramagnetic; there are no naturally occurring ferro- or ferrimagnetic constituents. Magnetic dust is the principal component of ferrous welding fume. It is also a significant part of asbestos dust, coal mine dust, and coal fly ash. Ferrimagnetic materials associated with particulate contaminants such as dust in the lungs of coal miners, welders, and asbestos workers can be detected by magnetizing these ferrimagnetic components.

Magnetopneumography (MPG), the measurement of magnetizable material within the lungs has been an important tool for measuring welding dust exposure in the ship building industry in Sweden and Finland. A magnetizing field is applied to the lungs (Fig. 67) and the remnant field

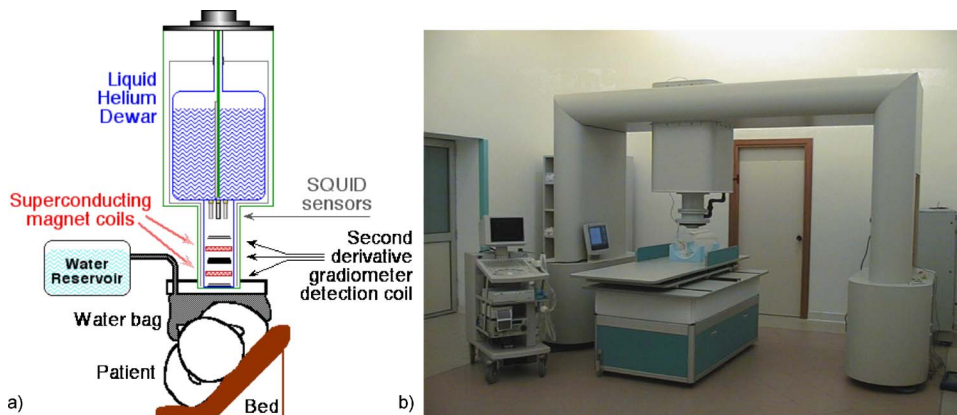


FIG. 66. (Color online) (a) Ferritometer® components. Typical patient movement is 10 cm vertically. The combination of a second order detection coil and a first order magnetizing coil gives excellent near field sensitivity while rejecting distant sources. (b) Installed system showing ultrasound scanner (to left of gantry) and plastic calibration phantom (on bed).

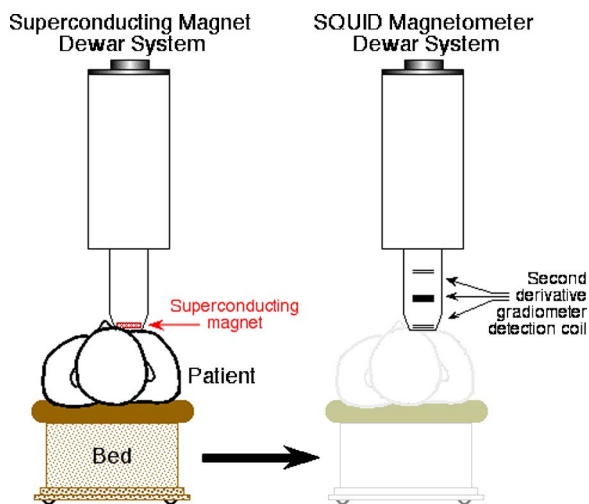


FIG. 67. (Color online) Magnetopneumography measurement system.

measured after removal of the field. The remnant field outside the chest after exposure to a magnetizing field can be as great as 1 nT.<sup>119</sup> Magnetic dust is also used as a tracer for measuring lung dust clearance.<sup>137</sup> An inhaled dosage of 1 mg is sufficient to follow clearance over one year and later. Alveolar clearance half-time is about four months in healthy nonsmokers and increases in smokers and in patients with interstitial lung diseases.<sup>138</sup> Recently, it has been shown that particle clearance in the airways has a long-term phase.<sup>139</sup>

The SQUID magnetometer<sup>140</sup> is sensitive enough to detect particles of magnetite in the lung at levels totaling as little as 20  $\mu\text{g}$  equivalent to 0.5  $\text{ng}/\text{cm}^3$  of lung tissue.<sup>141</sup> By exposing the chest to an external magnetic field of about 0.1 T, the magnetic particles become aligned and the lungs weakly magnetized. After the magnetization field is removed, the pattern of magnetization, as sensed by magnetometers, can be used to deduce the quantity and location of the magnetic particles. Exposure to a 70 mT dc field for 5 ms is sufficient to achieve 90% saturation of ferrimagnetic particles.

In the lung the magnetic particles are phagocytized within hours by alveolar macrophages. Intracellular transport will cause the magnetic polarization to decay with a characteristic time constant,  $M_H = m_s(1 - e^{-t/\tau_H})$ , where  $M_H$  is the magnetization measured by the SQUID gradiometer (Fig. 67),  $m_s$  is the moment of the ferromagnetic particle, and  $\tau_H$  is the time constant of decay, typically a few minutes. In addition, the remnant magnetic particles can be twisted in weak (millitesla) magnetizing fields, which reveal viscoelastic properties of alveolar macrophages. Both relaxation and twisting are indicators for the function of alveolar macrophages in the human lung.<sup>142</sup>

## I. Animal systems

Research instruments for animal measurements have been typically low channel count systems with smaller detection coils. The higher spatial resolution desired for animal measurements (sometimes as small as 100  $\mu\text{m}$ ) also requires closer spacing. The use of adjustable tail Dewars (Fig. 26) and coil-in-vacuum technology can allow moderate count

(7–37) small diameter (1–4 mm) detection coil arrays to be built without having to use excessively thick Dewar tail pieces. The actual design of an animal system is very much dependent on the size and shape of the animal being measured. For mice and other small animals, physical constraints (and budgets) often limit the measurement system to a few channels of millimeter scale detection coils inside a flat tail Dewar. A system for MEG measurements on a macaque monkey could be a scaled down version of an adult whole head system (Sec. X C). SQUID magnetometers can also be used for measurements of action potentials<sup>143</sup> and tissue slices. The technology developed for magnetic microscopy (Sec. IX C 1) has also influenced the development of animal systems designed for *in vitro* measurements.<sup>144</sup>

## J. Biomagnetic instrumentation concerns

In summary, when building or purchasing a SQUID system for biomagnetic measurements, the following design areas must be considered.

- Number of channels: How many are needed (be sure not to overestimate, cost is a function of channel number)? Are multiple (multiposition) measurements acceptable (slower, but require less channels) or must the measurement(s) be done in a single measurement?
- Signal-to-noise ratio: What is the sensitivity required? Should sensitivity be specified as minimum detectable changes in field ( $\text{fT}/\sqrt{\text{Hz}}$ ) or current dipole ( $\text{A m}/\sqrt{\text{Hz}}$ )?
- Detection coil design: What are the characteristics of source [current dipole, linear (e.g., peripheral nerve), magnetic dipole, etc.]? This will indicate if single orientation (e.g.,  $B_z$ ) or vector (e.g.,  $B_z$ ,  $B_x$ , and  $B_y$ ) orientation detection coils are needed. What coil diameter will give the needed sensitivity? What coil layout (hexagonal, square, etc.) is best? What coil-to-coil spacing is needed?
- Magnetometer versus gradiometer: Does environmental noise require the use of gradiometers? If so, what style (axial versus planar), order, and base line are needed?
- Noise reduction: What is the environmental noise? Have ground loops, EMI, and vibration (e.g., nearby traffic—human or vehicle) been accounted for? Will magnetic shielding be needed? If so, what type (MSR versus eddy current room)? Will reference channels be used for electronic noise cancellation?

If so, will pre- or postprocessing algorithms be used?

- Cryogenics:

What is the needed coil-to-subject distance(s)?

Is liquid helium suitable or is closed cycle refrigeration required?

- Data acquisition rates:

What is the total amount of data to be gathered in a single session?

Must the data be processed real time?

How is the data to be interpreted?

How is the data to be displayed?

Will the data be correlated with other methodologies (e.g., EEG, MRI, CT, ECG, and PET)?

## ACKNOWLEDGMENTS

The author gratefully acknowledges helpful discussions with F. Bedard, John Clarke, Duane Crum, Michael Faley, the late Robin Giffard, Mark Kennedy, Larry Maltin, Winfried Möller, Jochen Mannhart, Marty Nisenoff, Doug Paulson, Stephen Robinson, Ray Sarwinski, Mike Simmonds, Bill Sutherling, Jiri Vrba, Harold Weinstock, Ben Weiss, the late Sam Williamson, and P.J. Zarecky. The author would also like to acknowledge Hypres, Inc., for Fig. 10(b), Vacuumschmelze GmbH for Fig. 29, Sky Research for Fig. 39, J. P. Wikswo for Fig. 43, Neocera for Fig. 51, CTF for Fig. 58(b), W. Sutherling for Figs. 59 and 60, W. Black for Fig. 62, and W. Richards for Fig. 65.

<sup>1</sup>P. Ripka, *Magnetic Sensors and Magnetometers* (Artech, Boston, 2001).  
<sup>2</sup>H. Kamerlingh-Onnes, *Akad. van Wetenschappen, Amsterdam* **14**, 818 (1911).  
<sup>3</sup>D. J. Quin and W. B. Ittner, *J. Appl. Phys.* **33**, 748 (1962).  
<sup>4</sup>*The Physics of Superconductors*, edited by K. H. Bennemann and J. B. Ketterson (Springer, Berlin, 2003), Vols. 1 and 2.  
<sup>5</sup>J. Bardeen, L. N. Cooper, and J. R. Schrieffer, *Phys. Rev.* **108**, 1175 (1957).  
<sup>6</sup>J. G. Bednorz and K. A. Müller, *Z. Phys. B: Condens. Matter* **64**, 189 (1986).  
<sup>7</sup>D. Larbalestier, A. Gurevich, D. M. Feldmann, and A. Polyanskii, *Nature (London)* **414**, 368 (2001).  
<sup>8</sup>W. Meissner and R. Oschensfeld, *Naturwiss.* **21**, 787 (1933).  
<sup>9</sup>R. P. Feynman, R. B. Leighton, and M. Sands, *The Feynman Lectures on Physics* (Addison-Wesley, Reading, MA, 1965), Vol. 3.  
<sup>10</sup>B. D. Josephson, *Phys. Lett.* **1**, 251 (1962).  
<sup>11</sup>M. I. Faley *et al.*, *IEEE Trans. Appl. Supercond.* **9**, 3386 (1999).  
<sup>12</sup>C. D. Tesche and J. Clarke, *J. Low Temp. Phys.* **29**, 301 (1982).  
<sup>13</sup>R. P. Giffard, R. A. Webb, and J. C. Wheatley, *J. Low Temp. Phys.* **6**, 533 (1972).  
<sup>14</sup>T. Van Duzer and C. W. Turner, *Principles of Superconductive Devices and Circuits* (Elsevier, New York, 1981).  
<sup>15</sup>T. P. Orlando and K. A. Delin, *Foundations of Applied Superconductivity* (Addison-Wesley, Reading, MA, 1991).  
<sup>16</sup>J. Clarke and A. I. Braginski, *Fundamentals and Technology of SQUIDS and SQUID Systems*, The SQUID Handbook Vol. 1 (Wiley, New York, 2004).  
<sup>17</sup>R. B. Stephens and R. L. Fagaly, *Cryogenics* **31**, 988 (1991).  
<sup>18</sup>D. Koelle, R. Kleiner, F. Ludwig, E. Dantsker, and J. Clarke, *Rev. Mod. Phys.* **71**, 631 (1999).  
<sup>19</sup>M. B. Ketchen and J. M. Jaycox, *Appl. Phys. Lett.* **40**, 736 (1982).  
<sup>20</sup>J. E. Zimmerman, *J. Appl. Phys.* **42**, 4483 (1971).  
<sup>21</sup>D. Drung, S. Knappe, and H. Koch, *J. Appl. Phys.* **77**, 4088 (1995).  
<sup>22</sup>J. E. Zimmerman, P. Thiene, and J. T. Harding, *J. Appl. Phys.* **41**, 1572

(1970).  
<sup>23</sup>J. Clarke, in *SQUID Sensors: Fundamentals, Fabrications and Applications*, edited by H. Weinstock (Kluwer Academic, Dordrecht, 1997), pp. 1–62.  
<sup>24</sup>D. Drung, R. Cantor, M. Peters, H. J. Scheer, and H. Koch, *Appl. Phys. Lett.* **57**, 406 (1990); see also: D. Drung, C. Assmann, J. Beyer, M. Peters, F. Ruede, and Th. Schurig, *IEEE Trans. Appl. Supercond.* **15**, 777 (2005).  
<sup>25</sup>J. Li, C. P. Lusher, M. E. Digby, B. Cowan, J. Saunders, D. Drung, and T. Schurig, *J. Low Temp. Phys.* **110**, 261 (1998).  
<sup>26</sup>D. Drung, *Supercond. Sci. Technol.* **16**, 1320 (2003).  
<sup>27</sup>J. N. Hollenhorst and R. P. Giffard, *IEEE Trans. Magn.* **15**, 474 (1999).  
<sup>28</sup>SHE model 330X rf SQUID electronics.  
<sup>29</sup>Quantum Design model 2000 rf SQUID electronics.  
<sup>30</sup>R. T. Wakai and D. J. Van Harlingen, *Appl. Phys. Lett.* **52**, 1182 (1988).  
<sup>31</sup>C. W. Schneider, G. Hammerl, G. Logvenov, T. Kopp, J. R. Kirtley, P. J. Hirschfeld, and J. Mannhart, *Europhys. Lett.* **68**, 86 (2004).  
<sup>32</sup>H. Ohta, T. Matsui, and T. Uchikawa, *Neurology and Clinical Neurophysiology*, 2004:58 (November 30, 2004).  
<sup>33</sup>M. B. Simmonds and R. P. Giffard, U.S. Patent No. 4,389,612 (June 21, 1983).  
<sup>34</sup>J. Clarke (private communication).  
<sup>35</sup>R. Sarwinski (private communication).  
<sup>36</sup>R. L. Fagaly, *Sci. Prog.* **71**, 181 (1987).  
<sup>37</sup>M. Mück, J. B. Kycia, and J. Clarke, *Appl. Phys. Lett.* **78**, 967 (2001).  
<sup>38</sup>F. W. Grover, *Inductance Calculations, Working Formulas and Tables* (Dover, New York, 1962).  
<sup>39</sup>M. B. Simmonds, W. A. Fertig, and R. P. Giffard, *IEEE Trans. Magn.* **MAG-15**, 478 (1979).  
<sup>40</sup>M. I. Faley, U. Poppe, K. Urban, D. N. Paulson, and R. L. Fagaly, *J. Phys.: Conf. Ser.* **43**, 1199 (2006).  
<sup>41</sup>J. P. Wikswo, Jr., *AIP Conf. Proc.* **44**, 145 (1978).  
<sup>42</sup>J. P. Wikswo, Jr. and B. J. Roth, *Electroencephalogr. Clin. Neurophysiol.* **69**, 266 (1988).  
<sup>43</sup>R. Ilmoniemi, J. Knuutila, T. Ryhänen, and H. Seppä, in *Progress in Low Temperature Physics*, edited by D. F. Brewer (Elsevier, Amsterdam, 1989), Vol. XII, pp. 1–63.  
<sup>44</sup>F. B. Jaworski and D. B. Crum, in *SQUID Applications to Geophysics*, edited by H. Weinstock and W. C. Overton (Society of Exploration Geophysicists, Tulsa, OK, 1981), pp. 19–25.  
<sup>45</sup>J. Vrba, in *SQUID Sensors: Fundamentals, Fabrications and Applications*, edited by H. Weinstock (Kluwer Academic, Dordrecht, 1997), pp. 117–178.  
<sup>46</sup>P. H. Ornelas, A. C. Bruno, C. Hall Barbosa, E. Andreade Lima, and P. Costa Ribeiro, *Supercond. Sci. Technol.* **16**, S427 (2003).  
<sup>47</sup>D. E. Farrell, C. J. Allen, P. N. Arendt, S. R. Foltyn, D. N. Paulson, R. L. Fagaly, and G. M. Brittenham, *Bull. Am. Phys. Soc.* **44**, 1553 (1999).  
<sup>48</sup>S. E. Robinson, in *Advances in Biomagnetism*, edited by S. J. Williamson, M. Hoke, G. Stroink, and M. Kotani (Plenum, New York, 1989), pp. 721–724.  
<sup>49</sup>P. J. M. Wöltgens and R. H. Koch, *Rev. Sci. Instrum.* **71**, 1529 (2000).  
<sup>50</sup>K. D. Timmerhaus and T. M. Flynn, *Cryogenic Process Engineering* (Plenum, New York, 1989), Chap. 7.  
<sup>51</sup>P. Lynam, W. Proctor, and R. G. Scurlock, *Cryogenics* **9**, 242 (1969).  
<sup>52</sup>A. Mathai, D. Song, Y. Gim, and F. C. Wellstood, *Appl. Phys. Lett.* **61**, 598 (1992).  
<sup>53</sup>D. S. Buchanan, D. N. Paulson, and S. J. Williamson, in *Advances in Cryogenic Engineering*, edited by R. W. Fast (Plenum, New York, 1988), Vol. 33, pp. 97–106.  
<sup>54</sup>L. E. Fong, J. R. Holzer, K. K. McBride, E. A. Lima, F. Baudenbacher, and M. Radparvar, *Rev. Sci. Instrum.* **76**, 053703 (2005).  
<sup>55</sup>G. Walker, *Miniature Refrigerators for Cryogenic Sensors and Cold Electronics* (Clarendon, Oxford, 1989).  
<sup>56</sup>C. Wang and P. E. Giffard, *Adv. Cryog. Eng.* **47B**, 641 (2002).  
<sup>57</sup>K. Sata, in *Recent Advances in Biomagnetism*, edited by T. Yoshimoto, M. Kotani, S. Juriki, H. Karibe, and N. Nakasato (Tohoku University Press, Sendai, 1999), pp. 63–66.  
<sup>58</sup>C. Heiden, in *SQUID Sensors: Fundamentals, Fabrications and Applications*, edited by H. Weinstock (Kluwer Academic, Dordrecht, 1997), pp. 289–306.  
<sup>59</sup>G.-L. Romani, S. J. Williamson, and L. Kaufman, *Rev. Sci. Instrum.* **53**, 1815 (1982).  
<sup>60</sup>J. F. Hoburg, *IEEE Trans. Electromagn. Compat.* **37**, 575 (1995).  
<sup>61</sup>G. Stroink, B. Blackford, B. Brown, and M. Horacek, *Rev. Sci. Instrum.* **52**, 463 (1981).

- <sup>62</sup>D. Cohen, *Rev. Phys. Appl.* **5**, 53–58 (1970).
- <sup>63</sup>D. Cohen, E. A. Edelsack, and J. E. Zimmerman, *Appl. Phys. Lett.* **16**, 278 (1970).
- <sup>64</sup>D. Cohen, *Science* **175**, 64 (1972).
- <sup>65</sup>J. Bork, H.-D. Hahlbohm, R. Klein, and A. Schnabel, in *Biomag2000*, Proceedings of the 12th International Conference on Biomagnetism, edited by J. Nenonen, R. J. Ilmoniemi, and T. Katila (Helsinki University of Technology, Espoo, Finland, 2001), pp. 970–973 (<http://biomag2000.hut.fi/proceedings.html>).
- <sup>66</sup>E. Baum and J. Bork, *J. Magn. Magn. Mater.* **101**, 69 (1991).
- <sup>67</sup>“The Definitive Guide to Magnetic Shielding,” Amuneal Corporation, Philadelphia, PA (unpublished).
- <sup>68</sup>J. R. Claycomb and J. H. Miller, *Rev. Sci. Instrum.* **12**, 4562 (1999).
- <sup>69</sup>D. Cohen, U. Schläpfer, S. Ahlfors, M. Hämäläinen, and E. Hålgren, in *Proceedings of the 13th International Conference on Biomagnetism*, edited by H. Nowak, J. Haueisen, F. Giessler, and R. Huonker (VDE Verlag GmbH, Berlin, 2002).
- <sup>70</sup>J. Anderberg, M. Cloclough, D. B. Crum, D. N. Paulson, and R. L. Fagaly, *IEEE Trans. Appl. Supercond.* **13**, 231 (2003).
- <sup>71</sup>H. Weinstock (private communication). This is often referred to as Weinstock’s law.
- <sup>72</sup>M. Kuchnir, J. D. McCarthy, and P. A. Rapidis, *IEEE Trans. Magn.* **MAG-21**, 997 (1985).
- <sup>73</sup>T. Watanabe, S. Watanabe, T. Ikeda, M. Kase, Y. Sasaki, T. Kawaguchi, and T. Katayama, *Supercond. Sci. Technol.* **17**, S450 (2004).
- <sup>74</sup>R. L. Fagaly, *Sensors* **13**, 18 (1996).
- <sup>75</sup>R. E. Sarwinski, *Cryogenics* **17**, 671 (1977).
- <sup>76</sup>O. Lounasmaa, *Experimental Principles and Methods below 1 K* (Academic, London, 1974).
- <sup>77</sup>J. P. Wikswo, *Rev. Sci. Instrum.* **53**, 1846 (1982).
- <sup>78</sup>B. Levy and A. J. Greenfield, *Rev. Sci. Instrum.* **50**, 655 (1979).
- <sup>79</sup>F. Bordoni, P. Carelli, I. Modena, and G.-L. Romani, *J. de Physique* **39**, 1213 (1978).
- <sup>80</sup>J. S. Philo and W. M. Fairbank, *Rev. Sci. Instrum.* **48**, 1529 (1977); see also: E. P. Day, T. A. Kent, P. A. Lindahl, E. Munck, W. H. Orme-Johnson, H. Roder, and A. Roy, *Biophys. J.* **52**, 837 (1987).
- <sup>81</sup>Model MPMS, Quantum Design, 6325 Lusk Boulevard, San Diego, CA.
- <sup>82</sup>K. Amaya, K. Shimizu, M. I. Eremets, T. C. Kobayashi, and S. Endo, *J. Phys.: Condens. Matter* **10**, 11179 (1998).
- <sup>83</sup>M. McElfresh, “Fundamentals of Magnetism and Magnetic Measurements,” Quantum Design Technical Document, 1994 (unpublished), <http://www.qdusa.com/resources/techdocs.html>.
- <sup>84</sup>S. Foner, *Rev. Sci. Instrum.* **30**, 548 (1959).
- <sup>85</sup>M. Pelizzione and A. Teyvaud, *Appl. Phys.* **24**, 375 (1981).
- <sup>86</sup>R. A. Webb, *Rev. Sci. Instrum.* **48**, 1585 (1977).
- <sup>87</sup>C. Hilbert, J. Clarke, T. Sleator, and E. L. Hahn, *Appl. Phys. Lett.* **47**, 637 (1985).
- <sup>88</sup>B. J. Klemme, M. J. Adriaans, P. K. Day, D. A. Sergatskov, T. L. Aselage, and R. V. Duncan, *J. Low Temp. Phys.* **116**, 133 (1999).
- <sup>89</sup>N. Solomonson, W. O. Hamilton, W. Johnson, and B. Xu, *Rev. Sci. Instrum.* **65**, 174 (1977).
- <sup>90</sup>J. M. Lockhart, B. Muhlfelder, G. M. Gutt, M. Luo, R. C. Clappier, T. R. McGinnis, and G. R. Smith, *IEEE Trans. Appl. Supercond.* **7**, 2354 (1997). A discussion of the SQUID readout and superconducting shielding can be found in J. M. Lockhart, *Proc. SPIE* **619**, 148 (1986).
- <sup>91</sup>CDMS Collaboration, D. S. Akerib *et al.*, *Phys. Rev. Lett.* **93**, 211301 (2004).
- <sup>92</sup>R. Bradley, J. Clarke, D. Kinion, L. J. Rosenberg, K. van Bibber, S. Matsuki, M. Mück, and P. Sikivie, *Rev. Mod. Phys.* **75**, 777 (2003).
- <sup>93</sup>B. Cabrera, *Phys. Rev. Lett.* **48**, 1378 (1982).
- <sup>94</sup>A. F. Hebard and W. M. Fairbank, in *Proceedings of the 12th International Conference of Low Temperature Physics* (Keigaku, Tokyo, 1971), p. 855; see also L. W. Jones, *Rev. Mod. Phys.* **49**, 717 (1977).
- <sup>95</sup>M. Mück and J. Clarke, *Rev. Sci. Instrum.* **72**, 3691 (2001).
- <sup>96</sup>J. Oppenländer, Ch. Häussler, T. Träuble, and N. Schopohl, *Physica C* **368**, 119 (2002).
- <sup>97</sup>N. Schopohl, *IEEE Trans. Appl. Supercond.* **15**, 936 (2005).
- <sup>98</sup>A. A. Kaufman and G. V. Keller, *The Magnetotelluric Sounding Method* (Elsevier, New York, 1981).
- <sup>99</sup>M. E. Ander, R. Goss, D. Strangway, C. Hillebrand, A. W. Laughlin, and H. Cassandra, *Geothermal: Energy for the Eighties*, Geothermal Resources Council Transactions Vol. 4 (Geothermal Resources Council, Davis, CA, 1980), pp. 5–8.
- <sup>100</sup>T. D. Gamble, W. M. Goubau, and J. Clarke, *Geophysics* **37**, 98 (1979).
- <sup>101</sup>W. Wynn, C. Frahm, P. Carroll, R. Clark, J. Welhoner, and M. Wynn, *IEEE Trans. Magn.* **11**, 701 (1975).
- <sup>102</sup>T. R. Clem, G. J. KeKelis, J. D. Lathrop, D. J. Overway, and W. Wynn, in *SQUID Sensors: Fundamentals, Fabrications and Applications*, edited by H. Weinstock (Kluwer Academic, Dordrecht, 1997), pp. 517–586.
- <sup>103</sup>R. Wold, P. Weichman, M. Tondra, E. Lange, C. Nordman, D. Paulson, T. Starr, J. Johnson, and D. Wilkinson, Development of a standoff UXO detection system using SDT and high temperature SQUID sensor arrays, UXO Forum 2000, Anaheim, May 2000.
- <sup>104</sup>G. Panatov, M. Bick, Y. Zhang, and H.-J. Krause, *IEEE Trans. Appl. Supercond.* **11**, 888 (2001).
- <sup>105</sup>V. Zakosarenko, A. Chwala, J. Ramos, R. Stolz, V. Schultze, H. Lütjen, J. Blume, and T. Schüller, *IEEE Trans. Appl. Supercond.* **11**, 896 (2001).
- <sup>106</sup>C. P. Foley *et al.*, *IEEE Trans. Appl. Supercond.* **9**, 3786 (1999); see also K. E. Leslie *et al.*, *IEEE Trans. Appl. Supercond.* **13**, 759 (2003).
- <sup>107</sup>D. J. Dunlop and O. Ozdemir, *Rock Magnetism: Fundamentals and Frontier* (Cambridge University Press, New York, 1997).
- <sup>108</sup>K. E. Leslie, R. A. Binks, C. J. Lewis, M. D. Scott, D. L. Tilbrook, and J. Du, *IEEE Trans. Appl. Supercond.* **11**, 252 (2001).
- <sup>109</sup>B. P. Weiss, J. L. Kirschvink, F. J. Baudenbacher, H. Vali, N. T. Peters, F. A. Macdonald, and J. P. Wikswo, *Science* **290**, 791 (2000).
- <sup>110</sup>Y. P. Ma and J. P. Wikswo, *Rev. Prog. Quant. Nondestr. Eval.* **17**, 1067 (1998).
- <sup>111</sup>K. Telschow (unpublished).
- <sup>112</sup>R. L. Fagaly, *IEEE Trans. Magn.* **MAG-25**, 1216 (1989).
- <sup>113</sup>J. Kirtley, *IEEE Spectrum* **33**, 40 (1996).
- <sup>114</sup>W. G. Jenks, S. S. H. Sadeghi, and J. P. Wikswo, *J. Phys. D* **30**, 293 (1997).
- <sup>115</sup>J. P. Wikswo, in *Advances in Cryogenic Engineering*, edited by R. W. Fast (Plenum, New York, 1988), Vol. 33, pp. 107–116.
- <sup>116</sup>Ch. Gerber, H. Hilgenkamp, and J. Mannhart, U.S. Patent No. 6,211,673 (3 April 2001).
- <sup>117</sup>J. Schambach, L. Warzemann, P. Weber, R. Kötz, and W. Weitschies, *IEEE Trans. Appl. Supercond.* **9**, 3527 (1999).
- <sup>118</sup>R. L. Fagaly, in *Magnetoencephalography*, Advances in Neurology Vol. 54 edited by S. Sato (Raven, New York, 1990), pp. 11–32.
- <sup>119</sup>S. J. Williamson and L. Kaufman, *J. Magn. Magn. Mater.* **22**, 129 (1981).
- <sup>120</sup>H. Kado *et al.*, in *Biological Imaging and Sensing*, edited by T. Furukawa (Springer, Berlin, 2004), pp. 117–204; see also J. C. Mosher, S. Baillet, and R. M. Leahy, Proceedings of the 2003 IEEE Workshop on Statistical Signal Processing (IEEE Cat. No. 03TH8705), pp. 294–297 (2003); R. E. Greenblatt, A. Ossadtchi, and M. E. Pflieger, *IEEE Trans. Signal Process.* **53**, 3403 (2005).
- <sup>121</sup>S. E. Robinson and R. L. Fagaly, Proceedings of the American Society of Mechanical Engineers AES-9, 7 (1989).
- <sup>122</sup>J. Sarvas, *Med. Biol.* **32**, 11 (1987).
- <sup>123</sup>J. Knuutila, S. Ahlfors, A. Ahonen, J. Hällström, M. Kajola, O. V. Lounasmaa, V. Vilkmann, and C. Tesche, *Rev. Sci. Instrum.* **58**, 2145 (1987).
- <sup>124</sup>W. Sutherland (private communication).
- <sup>125</sup>S. Sato, *Magnetoencephalography: Comparison with Electroencephalography and Clinical Applications*, Advances in Neurology Vol. 54 (Raven, New York, 1990).
- <sup>126</sup>B. D. Van Veen, W. Van Drongelen, M. Yuchtman, and A. Suzuki, *IEEE Trans. Biomed. Eng.* **44**, 867 (1997).
- <sup>127</sup>S. E. Robinson and J. Vrba, in *Recent Advances in Biomagnetism*, edited by T. Yoshimoto, M. Kotani, S. Juriki, H. Karibe, and N. Nakasato (Tohoku University Press, Sendai, 1999), pp. 302–305.
- <sup>128</sup>Y. Okada, K. Pratt, C. Atwood, A. Mascarenas, R. Reineman, J. Nurminen, and D. Paulson, *Rev. Sci. Instrum.* **77**, 024031 (2006).
- <sup>129</sup>R. Engelhardt, E. B. Fung, P. Kelly, T. R. Biehl, Z. Pakbaz, P. Nielsen, P. Hartz, and R. Fischer, *Neurology and Clinical Neurophysiology* **32**, 1 (2004).
- <sup>130</sup>R. Fencic, D. Brisinda, and A. M. Meloni, *Neurology and Clinical Neurophysiology 2004:13* (November 30, 2004).
- <sup>131</sup>R. T. Wakai, M. Wang, and C. B. Martin, *Am. J. Obstet. Gynecol.* **170**, 770 (1994).
- <sup>132</sup>I. Hashimoto, T. Mashiko, T. Mizuta, T. Imada, K. Iwase, and H. Okazaki, *Electroencephalogr. Clin. Neurophysiol.* **93**, 459 (1997).
- <sup>133</sup>L. A. Bradshaw, J. K. Ladipo, D. J. Stapon, J. P. Wikswo, Jr., and W. O. Richards, *IEEE Trans. Biomed. Eng.* **46**, 959 (1999).
- <sup>134</sup>D. N. Paulson, R. L. Fagaly, R. M. Toussaint, and R. Fischer, *IEEE Trans. Magn.* **MAG-27**, 3249 (1991).
- <sup>135</sup>G. M. Brittenham, D. E. Farrell, J. W. Harris, E. S. Feldman, E. H. Danish, W. A. Muir, J. H. Tripp, and E. M. Bellon, *Neurophysiology*

- 307**, 1671 (1982).
- <sup>136</sup>C. M. Bastuscheck and S. J. Williamson, *J. Appl. Phys.* **58**, 3896 (1985).
- <sup>137</sup>D. Cohen, S. F. Arai, and J. D. Brain, *Science* **204**, 514 (1979).
- <sup>138</sup>W. Möller, W. Barth, M. Kohlhäufel, K. Häussinger, W. Stahlhofen, and J. Heyder, *Exp. Lung Res.* **27**, 547 (2001).
- <sup>139</sup>J. Heyder, *J. Appl. Physiol.* **97**, 2200 (2004).
- <sup>140</sup>D. N. Paulson, R. M. Toussaint, and R. L. Fagaly, *IEEE Trans. Magn. MAG-23*, 1315 (1987).
- <sup>141</sup>W. Stahlhofen and W. Möller, *Radiat. Environ. Biophys.* **32**, 221 (1993).
- <sup>142</sup>W. Möller, W. G. Kreyling, M. Kohlhäufel, K. Häussinger, and J. Heyder, *J. Magn. Magn. Mater.* **225**, 218 (2001).
- <sup>143</sup>J. P. Wikswo, Jr., in *SQUID Sensors: Fundamentals, Fabrication and Applications*, edited by H. Weinstock (Kluwer Academic, Dordrecht, 1996), pp. 307–360.
- <sup>144</sup>F. Baudenbacher, N. T. Peters, P. Baudenbacher, and J. P. Wikswo, *Physica C* **368**, 24 (2002).